



Dissertation

Manufacturing of High-Loading Aqueous Cathodes for Li-Ion Batteries

carried out for the purpose of obtaining the degree of Doctor technicae (Dr. techn.), submitted at TU Wien, Faculty of Technical Chemistry
by

Dipl.-Ing. Lukas NEIDHART

Mat.No.: 01203528

under the supervision of

Univ. Prof. Dipl.-Ing. Dr. techn. Franz Winter

Institute of Chemical, Environmental and Bioscience Engineering, E166

Reviewed by

Prof. Dr. Wilhelm Pfleging

Institute for Applied Materials - Applied
Material Physics (IAM-AWP)

Karlsruhe Institute of Technology (KIT)

Hermann-von-Helmholtz-Platz 1, 76344

Eggenstein-Leopoldshafen, Germany

Univ.-Prof. Dipl.-Phys. Dr. Jürgen Fleig

Institute of Chemical Technologies and
Analytics

TU Wien

Getreidemarkt 9, 1060 Vienna, Austria

This work has been supported by the Austrian Federal Ministry for Climate Action, Environment, Energy, Mobility, Innovation, and Technology (BMK).

I confirm, that the printing of this thesis requires the approval of the examination board.

Affidavit

I declare in lieu of oath, that I wrote this thesis and carried out the associated research myself, using only the literature cited in this volume. If text passages from sources are used literally, they are marked as such. I confirm that this work is original and has not been submitted for examination elsewhere, nor is it currently under consideration for a thesis elsewhere. I acknowledge that the submitted work will be checked electronically-technically using suitable and state-of-the-art means (plagiarism detection software). On the one hand, this ensures that the submitted work was prepared according to the high-quality standards within the applicable rules to ensure good scientific practice "Code of Conduct" at the TU Wien. On the other hand, a comparison with other student theses avoids violations of my personal copyright.

Vienna, 26. September 2024

Signature

Acknowledgements

Completing this PhD thesis has been an unforgettable experience – one that I could not have undertaken alone.

First and foremost, I would like to express my gratitude to all of my colleagues from the Austrian Institute of Technology. Especially to my supervisor, Katja Fröhlich, for granting me the freedom and providing the literal and metaphorical "Roten Faden" that I needed to achieve my goals. Thank you for believing in me, for your guidance, and encouragement throughout the past years. Special thanks go to my colleagues and fellow researchers in the Battery Technologies group, the S²BAM group, and the Balcony Office. Your camaraderie, insightful discussions, and collaboration have made this process not only fruitful but truly enjoyable. I am grateful for the knowledge and friendship we have shared, knowing I can always rely on you.

I would also like to express my sincere appreciation to Franz Winter from TU Wien for your supervision and enthusiasm for my work. Your insights, especially in the final writing phase, helped me recognize the value in my findings and encouraged me to articulate them clearly and effectively on paper.

To my friends and family, thank you for your constant encouragement and understanding throughout this challenging journey. I especially want to thank my sister Anna for always being there for me. Big thanks also to Fuchsthal+1 for distracting and comforting me even after the most frustrating day in the lab. Thank you all for your contributions, whether big or small, to this thesis. I could not have done it without you.

Ich brauch' Power für mein' Akku

Keine Power in mein' Akku

Baby, leih' mir deinen Lader

Ich brauch' mehr Strom

- *Maurice Ernst (Bilderbuch)*

Abstract

Increasing the energy density of lithium-ion traction batteries is one of many challenges in electromobility. One way of increasing the energy density lies in fabricating electrodes with high active material loadings and correspondingly increased coating thicknesses. Unfortunately, producing such thick electrodes involves a high degree of complexity and requires innovative methods in electrode production. Additionally, there is a need for more sustainable and cost-effective ways of producing these electrodes.

In this work, a special coating technique was used, which ensures defect-free electrodes with coating thicknesses of over 200 μm , by subsequent coating of material layers on top of each other. This multi-layer coating technique was used in particular to process cathode materials with a high nickel content ($\text{LiNi}_{0.8}\text{Mn}_{0.1}\text{Co}_{0.1}\text{O}_2$, NMC811). With this method, an areal loading of $>8.6 \text{ mAh/cm}^2$ was realised. Great improvements in both mechanical properties and electrochemical performance were achieved by switching to this innovative coating method. For example, the adhesion to the current collector film was increased by 40%. Moreover, the specific discharge capacity was improved for all tested current rates in rate capability tests. Especially for low current rates (0.1C), an increase of more than 20% was achieved. Furthermore, multi-layer coating was used to create a binder gradient in the thickness direction of the coated layer. Here, the quantity of polymethyl acrylate (PMA) in the top layer was reduced in three steps (50%, 25% and 0% of the initial proportion of PMA). The electrodes produced were again tested in coin cells and, particularly at a C-rate of 1C, improvements in the specific discharge capacity of up to 39% were achieved compared to single-layer coatings. Electrochemical

impedance spectroscopy, Raman spectroscopy and scanning electron microscopy provide additional information about the importance of a distinct domain and distribution of conductive carbon black and binder in the coating.

As the coating thickness increases, the importance of optimal transport of Li^+ -ions through the electrode layer coating also rises. The tortuosity can be used as a characteristic parameter, especially for porous material layers. Using electrochemical impedance spectroscopy of symmetrical cells, the dependence of the tortuosity on the layer thickness was determined. A drastic increase in tortuosity was detected, for electrodes exceeding a certain thickness threshold of the coating (150 μm). This indicates a change in the material composition in the coating during the fabrication process. Subsequently, cathodes, produced using the multi-layer coating technique were examined. The results show that merely switching to this coating method can improve the tortuosity by approximately 55 %. Introducing a binder gradient further enhances this effect and enables minimum tortuosity values of $\tau \approx 2$, which correspond to a reduction of more than 80 % compared to thick single-coated layers. Finally, a strong negative correlation between tortuosity values and specific discharge capacities was determined.

Kurzfassung

Die Steigerung der Energiedichte in Li-Ionen Traktionsbatterien hat sich in den vergangenen Jahren als große Herausforderung im Bereich der Elektromobilität herausgestellt. Eine Möglichkeit, um die Energiedichte zu erhöhen liegt in der Fertigung von Elektroden mit hohen Aktivmaterialbeladungen und dementsprechend erhöhter Beschichtungsdicken. Die Herstellung solcher dicken Elektroden birgt ein großes Maß an Komplexität und verlangt nach innovativen Methoden in der Elektrodenfertigung. Hinzu kommt ein Streben nach immer nachhaltigeren und kostengünstigen Möglichkeiten diese Elektroden herzustellen.

Im Zuge dieser Arbeit wurde auf ein Beschichtungsverfahren zurückgegriffen, durch welches sich mittels mehrmaligen, aufeinanderfolgenden Aufbringens von Materialschichten defektfreie Schichten von über 200 μm ermöglichen lassen. Diese Technik der Mehrlagenbeschichtung (multi-layer coating) wurde im speziellen verwendet um Kathodenmaterialien mit hohem Nickelanteil ($\text{LiNi}_{0.8}\text{Mn}_{0.1}\text{Co}_{0.1}$, NMC811) ohne die Verwendung von toxischen Lösungsmitteln zu verarbeiten. Dabei konnte eine Flächenbeladungen von $>8.6 \text{ mAh/cm}^2$ erzielt werden. Das Umstellen der Beschichtungsmethode und Realisieren eines Zweischichtsystems bringt zudem sowohl große Verbesserungen in mechanischen Eigenschaften als auch in der elektrochemischen Performance mit sich. So konnte zum Beispiel die Adhäsion zur Stromsammlerfolie um 40% erhöht werden. Auch bei Ratenfestigkeitstests konnte für alle getesteten Stromraten eine Erhöhung der spezifischen Entladekapazität erzielt werden. Vor allem für niedrige Stromraten (0.1C) wurde eine Steigerung um mehr als 20% erreicht. Dieselbe Methode wurde in weitere Folge benutzt, um einen Bindemittelgradienten in Dickenrichtung der Beschichtung zu erzielen. Hierbei wurde der

Materialanteil an Polymethylacrylat (PMA) in der oberen Schicht in 3 Schritten (50%, 25% und 0% des initialen Anteils an PMA) reduziert. Die hervorgebrachten Elektroden wurden wiederum in Knopfzellen getestet und besonders bei C-Raten von 1C konnten Verbesserungen in der spezifischen Entladekapazität von bis zu 39% gegenüber einlagigen Beschichtungen erzielt werden. Analysen mittels Elektrochemischer Impedanzspektroskopie, Ramanspektroskopie und Rasterelektronenmikroskopie geben zusätzlich Aufschluss über die Wichtigkeit einer ausgeprägten Domäne aus Leittruss und Bindemittel in der Schicht.

Bei einer Erhöhung der Beschichtungsdicke nimmt auch die Bedeutung eines optimalen Transports von Li^+ -Ionen durch die Schicht zu. Die Tortuosität, als Maß an Gewundenheit einer porösen Materialschicht, kann hierbei als charakteristischer Parameter für den Li^+ -Transport herangezogen werden. Mittels Elektrochemischer Impedanzspektroskopie von symmetrischen Zellen, wurde die Abhängigkeit der Tortuosität von der Schichtdicke eruiert. Beim Überschreiten eines Diczegrenzwerts (150 μm) der Beschichtung konnte ein drastischer Tortuositätsanstieg festgestellt werden. Dieser indiziert eine Veränderung der Materialzusammensetzung während des Beschichtungsvorganges in der Schicht. In weiterer Folge wurden auch die Kathoden, welche mittels Mehrlagenbeschichtung hergestellt wurden, untersucht. Die Ergebnisse zeigen, dass allein durch ein Umstellen auf diese unkonventionelle Beschichtungstechnik eine Verbesserung der Tortuosität um ungefähr 55% erzielt werden kann. Das Einbringen eines Bindemittelgradienten verstärkt diesen Effekt noch weiter, und ermöglicht Minimalwerte der Tortuosität von $\tau \approx 2$, was einer Erniedrigung gegenüber einfachbeschichteten Elektroden von mehr als 80% entspricht. Analysiert man einen Zusammenhang von Tortuositätswerten und spezifischen Entladekapazitäten lässt sich zudem eine starke negative Korrelation der beiden Parameter feststellen.

List of Publications

Journal Publications

- I Lukas Neidhart, Katja Fröhlich, Nicolas Eshraghi, Damian Cupid, Franz Winter, and Marcus Jahn. Aqueous Manufacturing of Defect-Free Thick Multi-Layer NMC811 Electrodes. *Nanomaterials*, 12(3):317, 2022.
- II Lukas Neidhart, Katja Fröhlich, Franz Winter, and Marcus Jahn. Implementing Binder Gradients in Thick Water-Based NMC811 Cathodes via Multi-Layer Coating. *Batteries*, 9(3):171, 2023.
- III Lukas Neidhart, Katja Fröhlich, Buket Boz, Franz Winter, and Marcus Jahn. Layer by Layer: Improved Tortuosity in High Loading Aqueous NMC811 Electrodes, *Journal of The Electrochemical Society*, 171(5):050532, 2024

Further Publications

Journal Publications as Co-Author

1. Buket Boz, Katja Fröhlich, Lukas Neidhart, Palanivel Molaiyan, Giovanni Bertoni, Marco Ricci, Francesco De Boni, Miljana Vuksanovic, Martina Romio, Karin Whitmore, Marcus Jahn. Evaluating Polyacrylic Acid as a Universal Aqueous Binder for Ni-rich Cathodes NMC811 and Si Anodes in Full cell Lithium-ion Batteries. *ChemPlusChem*, e202400195, 2024.

Conference Contributions

1. Critical Parameter Evaluation of Thick, Multi-Layer Cathodes in Li-Ion Batteries; 22nd Advanced Batteries, Accumulators and Fuel Cells (ABAF)- Brno, Czech Republic; 2021 (oral presentation)
2. Establishing Multi-Layer Architectures in Thick Aqueous Cathodes for Li-Ion Battery Applications; Batteries Event 2021 – Lyon, France; 2021 (poster presentation)
3. Tortuosity Measurements as a Tool to Analyse Thick, Multi-Layered Cathodes for Li-Ion Batteries; 32nd Topical Meeting of the International Society of Electrochemistry (ISE) – Stockholm, Sweden; 2022 (oral presentation)
4. Benefits of Tuned Binder Distribution in Multi-Layered Thick NMC811 Cathodes; 242nd ECS Meeting - Atlanta, US; 2022 (oral presentation)
5. Enabling High Loadings for Aqueous NMC811 Cathodes via Multi-Layer Coating; International Battery Production Conference (IBPC) - Braunschweig, Germany; 2022 (oral presentation)
6. Innovative coating technique to increase the electrochemical performance of thick electrodes for Lithium-ion batteries; 7. GÖCh-Symposium - Physikalische Chemie und Elektrochemie in Österreich - Vienna, Austria; 2023 (poster presentation)
7. Impact of Coating Layer Parameters on Electrode Tortuosity; 244th ECS Meeting – Gothenburg, Sweden; 2023 (poster presentation)

Awards

1. Multi-Layer Manufacturing of Thick Electrodes for Li-Ion Batteries; AIT Poster Award 2022 (2nd place) sponsored by accent Inkubator GmbH and tecnet equity NÖ Technologiefinanzierungs-Invest GmbH

Contents

Abstract	vii
Kurzfassung	ix
List of Publications	xi
Contents	xiii
1 Introduction	1
1.1 Motivation	1
1.2 Aim of the Thesis	3
1.3 Outline	4
1.4 Working Principle of a Li-ion Battery	5
1.5 Electrode processing	9
1.6 High-Loading Electrodes	15
1.7 Multi-Layered Electrodes	18
2 Materials and Methods	21
2.1 Electrode Manufacturing and Analysis	21
2.2 Electrochemical Testing	24
3 Results and Discussion	31
3.1 Thick electrode processing	31
3.2 Tortuosity Evaluation	34
	xiii

4 Conclusion	37
5 Outlook	41
List of Figures	43
List of Tables	45
Acronyms	47
Bibliography	49
Journal Publications	61

Introduction

This chapter aims to give the reader insights into the motivation, objective, thesis outline.

1.1 Motivation

Intending to fight climate change, the global demand for efficient and long-lasting energy storage is higher than ever. The foundation for portable energy storage was laid out with Sony commercialising the first **lithium-ion battery (LIB)** in 1991 [1]. Since then, intensive research has been conducted to optimise secondary **LIBs** and make them accessible for different market applications. The e-mobility sector has received more attention from car manufacturers and legislators recently. Cheap, long-range traction batteries could push **electric vehicles (EVs)** to be a serious alternative to conventional cars with combustion engines. The global EV fleet is expected to drastically increase in size, making up 8–14% of the total light-duty vehicles by 2030. [2] From a European point of view, this progress is crucial since the recently negotiated European Green Deal enforces a climate-neutral transport sector by banning the sale of new cars with combustion engines by 2035. These ambitious goals enforce an increase in range and a drastic cost reduction. Both directly depend on the traction battery in use – so improving this crucial component needs to be tackled. Furthermore, there is also a demand for sustainable raw materials and a

green manufacturing process of the LIBs. The electrodes' raw material and the electrode fabrication are responsible for more than half of the costs of the whole battery – here, the production of cathodes takes the largest share. [3] The energy density of a battery is defined as the energy storage capability per volume. Maximising this value is especially important for traction batteries of electric vehicles, where space is limited and lightweight components are favourable. An increase in energy density can be achieved by amplifying the amount of material that actively participates in the electrochemical reactions (active materials) inside the battery and thus to the battery's capacity. Developing new active materials with higher capacities is one way of increasing the energy density of a battery. However, possibilities for Li-ion batteries are restricted by the number of suitable materials and have largely been explored. A different approach is to find solutions on a process engineering level. Fabrication of thicker electrode layers leads to an increased amount of active material and thus to higher capacities of the electrodes. Unfortunately, this is often accompanied by limitations in the manufacturing process and restricted electrochemical performance.

In state-of-the-art cathodes, polyvinylidene difluoride (PVDF) is still used as the standard binder due to its high chemical and electrochemical stability, necessary in the harmful environment prevalent in a battery cell. Its elastic and adhesive characteristics are also advantageous for the electrode fabrication process. [4] PVDF is hardly soluble and often needs volatile organic compounds like N-methyl-2-pyrrolidone (NMP) during the process. NMP is expensive, reproductionally toxic, and has a high boiling point – hampering green processing tremendously. Unfortunately, the combination of PVDF and NMP is still state-of-the-art in cathode processing. [5] To reduce the NMP emissions into the environment, solvent recovery systems with high energy demand are necessary during electrode manufacturing. [6] Moreover, people involved in the production process often need high personal protective equipment or are exposed to the released fumes during the drying process of the electrode. Additionally, PVDF belongs to the group of per- and poly-fluoroalkyl substances (PFAS) which pose a risk to the environment and public health when accumulated in living organisms. Switching to a process with water as

a solvent can solve these issues. Cost reduction, safety increase, and minimisation of environmentally harmful materials motivate the change to an aqueous process. [7-10]

1.2 Aim of the Thesis

The general objective of this thesis is to maximise the energy density of secondary Li-ion batteries. Optimising the manufacturing process of electrodes with high active material loading and hence increasing the layer thicknesses is to be examined as a possible solution. Since standard coating techniques are insufficient to fabricate thick electrodes, alternative methods must be developed. An additional goal is to increase the sustainability of the fabrication process, by substituting toxic **NMP** with water as a solvent during the process. Moreover, the electrode production steps should be upscalable from the lab scale to an industrially relevant roll-to-roll process. Ultimately, methods to validate the improved electrochemical performance of the produced electrodes need to be evaluated. All experiments are performed on electrodes with **LiNi_{0.8}Mn_{0.1}Co_{0.1}O₂ (NMC811)** as active material.

In summary, the presented thesis answers the general research question:

RQ: How can the energy density of Li-ion secondary batteries be increased?

To thoroughly answer this question, the following more specific research questions emerge:

RQ1: How can the manufacturing process be improved for high-loading electrodes?

RQ2: How can the production process of secondary battery electrodes be made more sustainable?

RQ3: What methods can be used to verify that a changed fabrication process positively influences the electrodes' electrochemical performance?

1.3 Outline

The global aim was to find a sustainable method to manufacture defect-free high-loading **NMC811** cathodes. Three open-access peer-reviewed publications form the basis of this cumulative thesis. The newly developed method of multi-layer electrode coating builds the foundation of this work.

Publication I, *Aqueous Manufacturing of Defect-Free Thick Multi-Layer NMC811 Electrodes*, [11] is the proof that **multi-layer (ML)** coating can be utilised to fabricate defect-free aqueous high-loading **NMC811** electrodes. A comparison to conventionally produced cathodes - coated in a **single-layer (SL)** - shows the positive effects **ML**-coating has on the electrochemical performance and mechanical integrity of the electrodes. Research questions 1 & 2 are covered by replacing toxic volatile organic compounds from the cathode fabrication process in combination with achieving high areal loadings.

In **Publication II**, *Implementing Binder Gradients in Thick Water-Based NMC811 Cathodes via Multi-Layer Coating*, [12] the multi-layer coating technique was used to implement a gradient in inactive binder material through the cross-section of the electrode. Cycling tests revealed the positive effect of the introduced 3D-like architecture and the importance of a well-established **carbon-binder-domain (CBD)**. This publication covers answers to research questions 1 & 2.

Finally, in **Publication III**, *Layer by Layer: Improved Tortuosity in High Loading Aqueous NMC811 Electrodes*, [13] **electrochemical impedance spectroscopy (EIS)** was used to investigate the tortuosity of water-based **NMC811** cathodes. An evaluation of the impact of the layer thickness as well as the benefits of the multi-layer approach has been analysed. The correlation between tortuosity and cycling performance can give information on the quality of the coating and can help to fine-tune the fabrication process accordingly. The results answer research question 3.

While **Publications I and II** share their focus on the aqueous manufacturing part of ML-coated electrodes, **Publication III** completes the preliminary results by connecting

electrochemical performance with tortuosity values.

The relationship between the publications and the research questions is visualised in Figure 1.1.

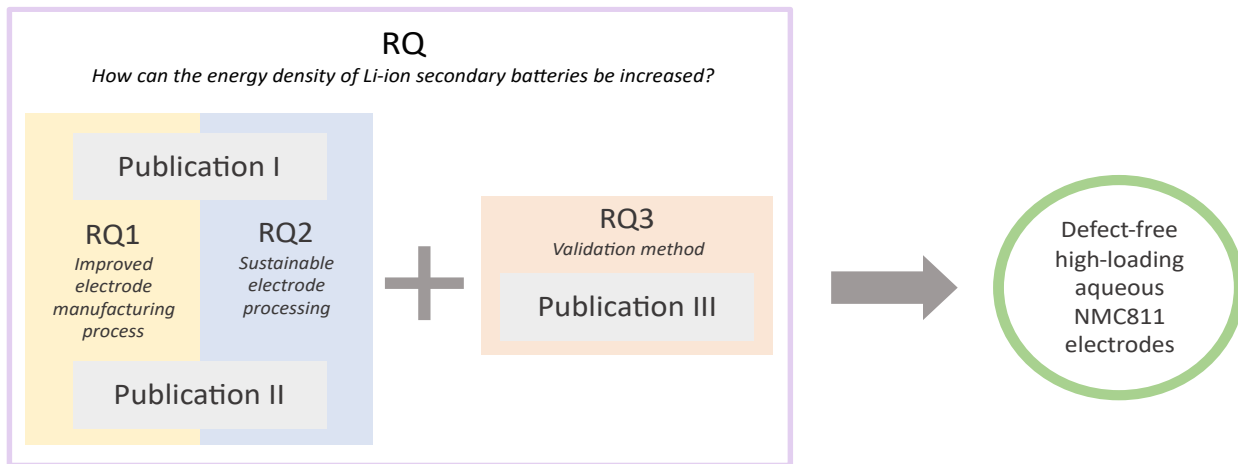


Figure 1.1: Connection between the publications and the research questions.

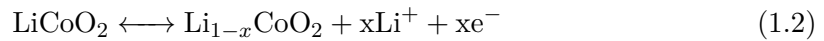
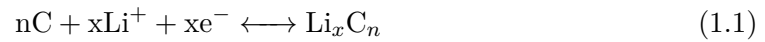
The main body of this thesis provides further theoretical background of the electrode manufacturing process and its restrictions for high-loading electrodes. Moreover, electrochemical limitations of thick electrodes including the influence of layer tortuosity are described. Key methods used in this thesis are given and the core results of all publications are put into context.

1.4 Working Principle of a Li-ion Battery

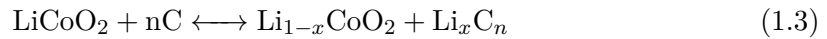
Li-ion battery cells usually consist of an electrode pair, with a separator in-between as insulation to avoid short circuits. They are encapsulated in a housing to be protected from external influences, which is filled with an ion-conducting electrolyte. A redox reaction takes place when the battery is charged and discharged. By convention, the electrode where the oxidation reaction occurs during the discharge is called the anode (negative electrode), whereas the reduction reaction happens at the cathode (positive

electrode). Figure 1.2 shows a rechargeable lithium-ion battery's basic components and principle with a graphitic anode and a layered metal oxide cathode. During discharge, Li^+ -ions deintercalate from the graphite, migrate through the separator, and intercalate in the cathode active material. The equivalent number of electrons travels simultaneously through an external electrical circuit from the anode to the cathode. When applying an external current, this process can be reversed and the battery will be charged.

As an example, the following reactions take place at the electrodes for a system consisting of graphite as anode (Equation 1.1) and LiCoO_2 as cathode (Equation 1.2):



The combination of both reactions leads to the overall cell reaction of (Equation 1.3):



In principle, the components of a battery can be separated into compounds which actively take part in the intercalation process (see above) and contribute to the capacity (active material) and everything else (e.g. separators, current collectors, binder material, housing etc.). Various types of active material, for both anode and cathode, have been the target of battery research within the last decades. The material selection for the positive and negative electrodes influences the cell's impedance, capacity and voltage due to the chemical potential difference of Li^+ in the electrodes. The target is to have high capacity and operational voltages to maximise the cell's energy density. Equation 1.4 shows the relation of the nominal energy E_n in Wh, the nominal voltage U_n in V and the nominal capacity C_n in Ah. [14]

$$E_n = U_n \cdot C_n \quad (1.4)$$

Increasing the cells' capacity directly leads to the development and synthesis of novel active materials. While commercial anodes mainly consist of graphite [15] and its

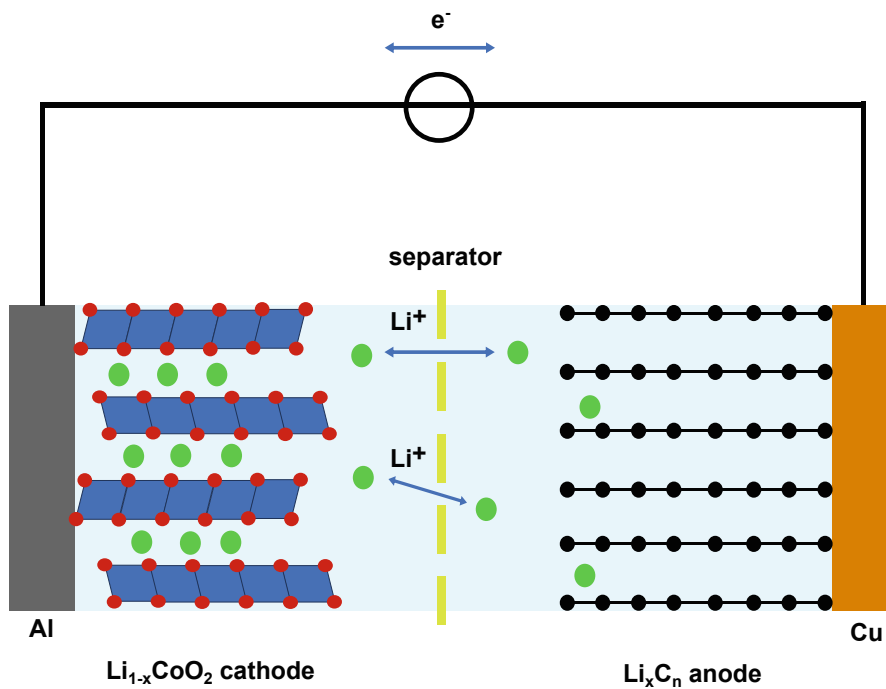


Figure 1.2: Schematic working principle of a Li-ion battery.

modifications, the urge for higher theoretical capacities enhances research in materials such as Si [16, 17], SiO_x [18, 19] or Sn [20, 21].

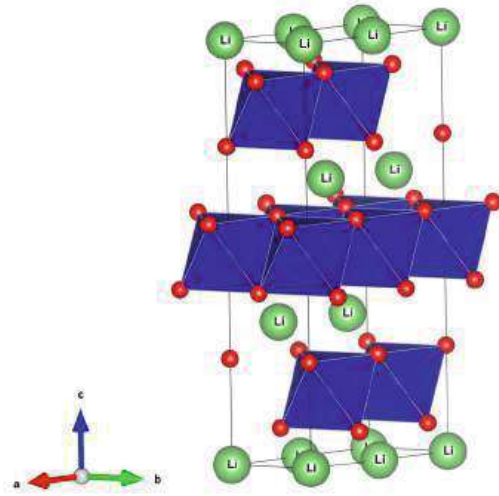
Cathode Materials

Choosing a suitable cathode material depends on the application's requirements and is always a compromise between cost, safety, life span, performance, specific energy and power. Generally, the options can be categorised depending on their crystal structure into layered (e.g. LiCoO_2 (LCO), $\text{LiNi}_x\text{Mn}_y\text{Co}_z\text{O}_2$ (NMC), $\text{LiNi}_x\text{Co}_y\text{Al}_z\text{O}_2$ (NCA)), spinel (e.g. LNMO, LMO) and olivine (e.g. LiFePO_4 (LFP)) materials. This thesis focuses on layered oxides which are described in more detail below.

Layered Oxides

Lithium cobalt oxide (LCO), introduced by Goodenough in the early 1980s [22], is a cathode active material with a layered rhombohedral structure (R3m space group)

consisting of transition metal oxides. Its layered structure facilitates Li-ion diffusion in the material during charge and discharge (Figure 1.3). LCO is still very prominent in the sector of portable consumer electronics, due to its high energy density and great cycling stability. However, Co's thermal instability, cost and toxicity encouraged researchers to replace this critical raw material with other transition metals. Incorporation of Ni leads to an increase in capacity and energy density, while simultaneously reducing the cost. The poor thermal stability of Ni is a trade-off. Further improvements can be made by adding Mn to the system, which cost-effectively increases the cycle life and safety of the battery. This leads to active materials with optimised Ni, Mn and Co percentages in the lattice. These lithium nickel manganese cobalt oxides (NMC) ideally combine all beneficial characteristics of the transition metals. Properties of $\text{LiNi}_x\text{Mn}_y\text{Co}_z\text{O}_2$ can be tuned by altering the ratio of x,y and z. By convention, materials with $x=y=z=1/3$ are called NMC111; $x=6, y=z=2$ NMC622 and $x=8, y=z=1$ NMC811 and so forth. With Ni being the main species involved in the redox reaction of the host structure, high Ni content leads to an increase in the practical specific capacity. E.g. NMC111 has a practical specific capacity of 160 mAhg^{-1} and NMC811 of 190 mAhg^{-1} . [23] At the expense of a Ni increase, a higher sensibility to ambient water and oxygen evolves mainly caused by the reduction of Mn. In addition, a low amount of Co can lead to a decrease in electronic conductivity. Another commercially used layered oxide material is $\text{LiNi}_x\text{Co}_y\text{Al}_z\text{O}_2$ (NCA), which is commonly available with an 80% share of Ni, 15% Co and 5% Al ($\text{LiNi}_{0.8}\text{Co}_{0.15}\text{Al}_{0.05}\text{O}_2$) — with a future tendency to lower Al contents. Thermal stability and capacity retention benefit from the small amount of Al-dopant, at the cost of a marginal decrease in cycling capacity. [24] In combination with a high practical capacity, these characteristics make NCA especially of interest for EV applications.

Figure 1.3: Layered structure of LiCoO_2 .

1.5 Electrode processing

In general, the manufacturing of a battery can be divided into two main processes: electrode production and cell assembly. The former can be subdivided into 3 steps: slurry mixing, coating, and calendaring (Figure 1.4).

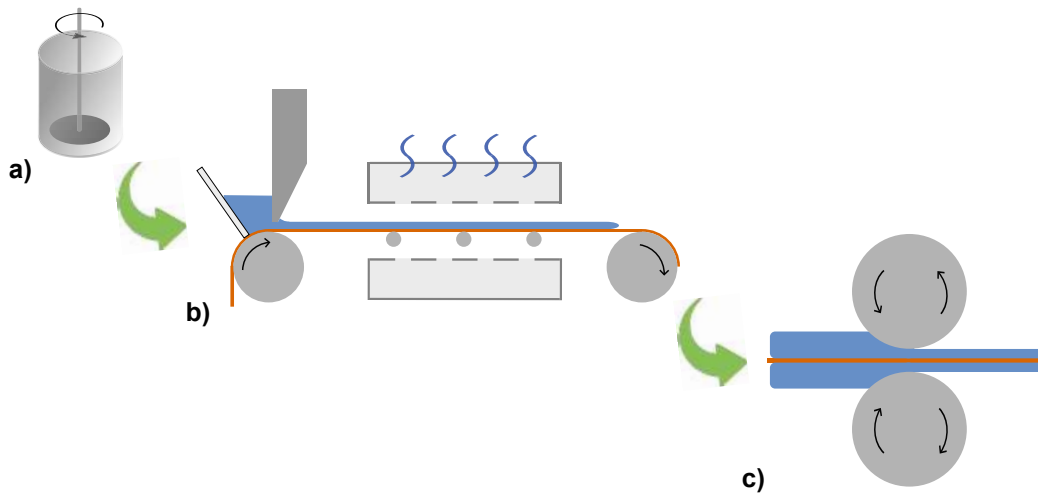


Figure 1.4: Steps of electrode manufacturing; a) slurry mixing, b) electrode coating, c) calendaring.

Slurry Mixing

A battery slurry consists of a few key ingredients: The active material, actively taking part in the electrochemical reaction; a conductive agent, to increase the electrical conductivity; and a set of binder materials that are necessary to make the slurry processable and to ensure mechanical properties of the electrode for further procedures. Wet processing is still state-of-the-art; thus, a solvent is needed for dispersing the dry components. While for graphitic anodes, water is already the state-of-the-art process solvent, cathodes are still produced with **NMP**. The ratio of the materials needs to be selected considering the final use case. On a laboratory scale, one will often find compositions of 90:5:5 wt% (active material:conductive agent:binder). The high binder concentration can help to fabricate mechanically stable electrodes for initial testing of the active materials at the expense of capacity. On an industrial level, inactive material needs to be minimised without compromising the mechanical integrity of the electrode. In principle, most larger slurry mixing systems consist of a fixed container and a rotating stirring attachment of various shapes. Ideally, all solid components are homogeneously dispersed within the solvent and no aggregates are formed, which can cause defects later in the process. Depending on the materials' physical characteristics, different shear forces are needed to guarantee equal distribution of all components without simultaneously destroying their physical structure. Furthermore, the mixing sequence plays an important role in keeping all components intact and suppressing the formation of agglomerates in the slurry. Through controlling the ratio between wet and dry ingredients and cautious selection of the binder, viscosity can be tuned to a range that fits the used coating technique. All of these factors need to be considered for a successful electrode coating.

Coating Process

The electrode coating process is crucial for the final morphology and quality of the fabricated battery electrode. Independently from the used technique, the previously mixed slurry will be applied to a metal foil substrate and dried afterwards. Ideally this

results in a coated layer with a homogeneous thickness in the coating direction and the width of the coating. There are multiple different coating methods applicable for electrode fabrication. The most prominent in battery manufacturing are slot-die and doctor-blade coating; of the working principles are shown in Figure 1.5.

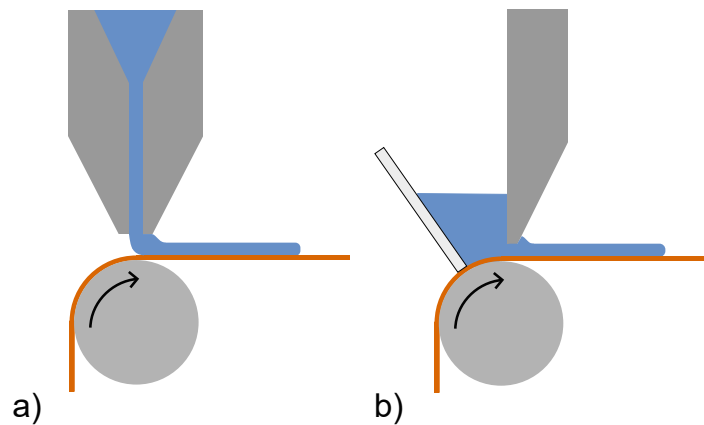


Figure 1.5: Principle and schematics of different coating techniques, a) slot-die coating, b) doctor blade coating

For the former, the slurry is pumped through a nozzle of certain dimensions and with a defined volume flow rate to control the thickness of the coated layer. One of the biggest advantages of this method is, that a high coating uniformity can be achieved. Additionally, it is also possible to perform intermittent coatings, which can be beneficial for increasing the electrode quality and production yield after calendaring. [25] The doctor-blade technique, also called knife-coating, is a solely mechanically metered coating method. The slurry is stored in a container directly next to the rake, positioned within a specific distance to the substrate foil. This gap width determines the wet-coating thickness and thus the active material loading of the electrode. The main advantages of doctor-blade coating are the setup's flexibility and cost-effectiveness, which enables fast prototyping and small-scale manufacturing. As most laboratory-scale coating systems are based on the same functional principle, scale-up is easily feasible without drastic changes in slurry and coating parameters. Another advantage is that it is less sensitive to particle size and viscosity of the slurry compared to slot-die coating, [26] where filters

need to be installed before the nozzle to prevent clogging and the rheology of the slurry has to be precisely monitored. However, only continuous coating is possible. This can lead to irregular layer thicknesses, especially at the coating edges.

Removing the solvent from the electrode is the final step of the coating process. Special attention needs to be paid on the temperature and time during the drying process of a coated electrode layer. These parameters must be matched to the materials in the slurry and the targeted layer thickness, otherwise, it can negatively affect the quality and further processability of the coating. Solvent evaporation and resulting capillary forces as well as phase separation of the slurry components and diffusion can lead to unwanted defects of the dry coating, [27] These can range from mechanical defects (e.g. cracks, pinholes and delamination) to changes in the microstructure of the coating (porosity and component segregation). Both can be detrimental to the electrochemical performance of the battery, due to higher internal resistances and lower capacity. [28] Drying rate, slurry formulation and binder selection play an important role during this complex process step. Optimisation of these parameters is necessary to keep the defects to a minimum. Taking up 20-30% of the energy consumption during cell production - drying is also the most energy-intensive manufacturing step. In particular, there are high costs if solvent recovery is necessary - as is the case with NMP as a process solvent. In general, substrate foils are coated on both sides (double-sided). Apart from the discussed coating methods other techniques such as spray coating [29], gravure coating [30], curtain coating [31], or screen printing exist [32], however, they are mostly used for specific applications or at a low technology readiness level (TRL).

Calendering

After the coating process is completed and the electrodes are dry, the coated layer is compacted to a specific porosity or density. The electrode is guided through two heatable steel rolls. The reason for calendering is manifold. First, the decrease in coating volume results in an increase of energy density for the battery cell - more energy is stored per unit volume. Second, the adhesion between the coating and substrate foil can be increased,

reduce the risk of delamination during further process steps and battery operation. [33] Overall, the structural integrity of a battery electrode can be enhanced throughout its lifetime. Densifying the material layers can be beneficial for particle cohesion and thus result in improved capacity retention, higher rate capability and greater cycling stability. [34] However, a sufficient pore structure across the layer thickness is needed to allow ion diffusion and penetration with electrolyte. [35, 36] Monitoring a good balance between porosity and tortuosity is therefore key for optimising the battery performance. Potential risks of overcompacting can also lead to the insertion of particles into the current collector or the damaging of active material particles.

Water-Based Electrode Manufacturing

The transition from an **NMP**-based process to a fully aqueous fabrication of battery electrodes bears many challenges, yet has a lot of benefits to offer and thus is a main focus of current electrode production research. [5, 7-9] Starting at the beginning of the electrode production chain, materials that are suitable for water-based processing need to be chosen. The main focus is here on water-soluble binders or binder systems, that experience no structural changes in the operational voltage window of the battery, and are chemically inert to all other cell components, especially to the electrolyte. Since **PVDF** is not soluble in water, **sodium-carboxymethyl cellulose (CMC)**(Na-CMC) is often the preferred binder substitution. Its remarkable properties are ideal for slurry mixing and electrode coating. **CMC** improves the rheological properties of the slurry during mixing, by functioning as a thickening agent. The long polymer chains also create a shear-thinning flow curve — favourable for the coating process. Due to the hydrophilic functional groups, it can electro-sterically interact with the hydrophobic surface of active material particles or carbon black and ensure a stabilised slurry. [37-40] **CMC** solidifies to very brittle and defective structures after the solvent has evaporated. Therefore, additional binder components (such as styrene-butadiene rubber/synthetic latex and acrylic-based binders) are used to increase the processability and mechanical integrity of the electrode. [41, 42] They increase the flexibility of the coating and lead

to a better adhesion to the current collector and improved cohesion of the coating layer itself. The binder system in combination with the conduction agent (mostly carbon black) creates a so-called carbon-binder-domain (CBD) that is responsible for a well-established conductive network through the coating layer, connecting active materials of all depths and ultimately with the current collector. [43]

In addition to the many advantages that water-based processing offers, there are unfortunately also a few undesirable effects that need to be considered. Some cathode active materials (e.g. NMC, NCA, LNMO) react with the process water, leading to Li^+ leaching out of the host lattice. This causes a proton exchange mechanism that results in the formation of reaction products such as lithium hydroxide (LiOH) or lithium carbonates (e.g. Li_2CO_3). [44] Irreversible loss in charge capacity happens, followed by an increased slurry pH. Since Al-foil is the typical current collector for the positive electrode, the slurry pH should be within a range of 4 and 8.6 to prevent the substrate from corroding. [45] A breakdown of the thin oxide layer of the Al can create water-soluble species, that can coat the active material particles and increase the interfacial resistance of the electrode. [46] The evolution of hydrogen gas also poses a problem for the mechanical integrity and defect density of the coating. Gas inclusions can either form cavities inside the layer when staying below its surface or otherwise generate detrimental crates and cracks. Thus, pH control is an important task in aqueous slurry processing and can be done by incorporating different acids [47-52] or forming an insoluble carbonate layer on the active material particles via pressurised CO_2 gas treatment. [53]

From a productional perspective, substantial energy savings can be achieved when switching from NMP to water-based coating processes, particularly in the drying step. Water has a considerably lower boiling point compared to NMP (202 °C). Consequently, either the drying time can be significantly reduced - leading to higher throughput in production - or the drying temperature can be reduced significantly. Both lead to a reduction in production costs. [10]

1.6 High-Loading Electrodes

As discussed previously, only the active material particles directly contribute to the capacity of a battery. Maximizing the ratio between active and inactive components leads to an increase in energy density. This can be done by increasing the active material loading in the coated layer, either by changing the slurry formulation or by increasing the coating thickness. [27, 54, 55] The former is limited by the necessary functionalities of the inactive components. Limitations for thick coating layers can arise from the fabrication process of the electrodes and the handling during cell assembly or can be of an electrochemical nature. Whereas commercially available LIB electrodes usually range in thickness between 50-100 μm , electrodes exceeding these values are referred to as thick [56, 57] or even ultra-thick in literature. [58, 59] However, this definition also greatly differs for different cell designs, porosities, and active materials used and thus needs to be used carefully. Although the differentiation on behalf of the active material loading would be the most accurate, the geometrical categorisation is sometimes more relevant considering the selection of certain process parameters.

Thicker electrodes would lead to fewer anode-cathode pairs needed to provide the same capacity. Therefore, less separator material and current collectors are required. Additionally, the time to assemble the cell is reduced. This can reduce cell cost by an order of magnitude. [7, 54, 60-62] However, an increase in energy density is often gained at the expense of power density and can cause many challenges during the production process. [60-62]

Productional Limitations

In contrast to standard electrode production, there are several points to consider when manufacturing thick electrodes, to minimise the risk of quality loss and subsequently the battery performance. When coating thick layers it is necessary to increase the viscosity of the slurry, to achieve and maintain a stable and uniform wet-thickness. Depending on the coating method, this can lead to considerable difficulties. Slot-die coaters for

example have a narrow viscosity window for defect-free fabrication. Increasing the slurry viscosity is done by increasing the solid content or utilisation of polymer binders with high molecular weight. However, this can cause problems during the mixing process, due to irregularities or inhomogeneities in the slurry emerging from insufficient dispersion. [63], [64] Longer mixing times or different mixing types are necessary to counteract this effect. Further, drying is the most critical manufacturing step when increasing the electrodes' loading. If the length of the dryers remains the same, either the temperature or the drying time must be increased. This is necessary to completely remove the solvent and thus enable a subsequent production process. However, increasing the drying rate can lead to unwanted problems. Fast solvent evaporation on the top of the coating can cause an upward bend of the foil edges, resulting in severe cracking of the coated layer when winded on the process rolls. Furthermore, this inhomogeneous solvent evaporation can result in a concentration gradient of certain slurry components in the cross-section of the layer. Binder particles of lower mass can be dragged to the top of the coating. Due to the rapid drying of the upper part of the coating, a liquid link to the region near the current collector can not be maintained and binder particles cannot distribute evenly throughout the coated layer. The result is a binder gradient, with a high amount of binder on top and a scarce distribution near the substrate foil. [59, 65-68] Since the binder system is responsible for good adhesion, this can lead to complete or partial exfoliation. [69] The phenomenon of binder migration can be controlled by gentle drying conditions [65] - low temperature, long drying times and carefully selected drying profiles. Unfortunately, this is not suitable for industrial applications.

The fabrication of thick electrodes also limits the choice of battery type almost entirely to pouch cells. This limitation is due to the restraint bending properties of thick layers and their disability to maintain mechanical integrity at a certain winding diameter. Especially, for cylindrical cells, the inner radius of a jelly roll can be as small as 1 mm, causing severe cracking and delamination of the coating. [60] Prismatic cells face similar issues at the long edge of the cell - however, an intermittent coating technique could enable thick electrodes here.

Electrochemical Limitations

Increased layer thickness also affects the electrochemical performance of an electrode. Previously discussed regions of high binder concentration lead to elongating the Li^+ -ion transport pathways within the layer. The electrode tortuosity is the limiting factor here. It describes the path length the Li^+ -ions need to travel within the porous electrode structure and is highly dependent on the electrode morphology. The tortuosity is defined as the ratio of the real path length to the ideal, straight path length Li^+ -ions need to travel through the coated layer. [70, 71] An inhomogeneous distribution of material components inside the layer can cause an extension of the ionic transport pathways, resulting in an increased tortuosity value. This electrode parameter can also be significantly influenced by dead ends, branches or surface impurities within the coated layer. [72] Accumulating binder particles on the coating surface can lead to insulating blockages and thus to a considerable increase of the tortuosity. In the case of an inhomogeneous distribution of conducting agents, a continuous electrical conductivity between active materials in all layer depths and to the current collector can result in high internal electrical resistances. Here, the electrical conductivity can be increased for high-loading electrodes by replacing a share of carbon black with graphite. Due to their larger diameter, compared to carbon black particles, graphite can help to maintain long-range electrical resistance in the electrode. This can improve the electrical conductivity throughout thick coating layers. Inhomogeneous distribution of binder and/or conductive additive can lead to capacity loss due to the non-utilisation of active material in areas of the electrode that are not well cross-linked, and uneven heat distribution can lead to rapid degradation of the material and ultimately to a shorter lifetime of the cell. Partial use of active material particles can also happen due to bad electrode wetting with the electrolyte. Sites near the current collector foil which are not in contact with the electrolyte cannot take part in intercalation processes leading to notable capacity losses.

1.7 Multi-Layered Electrodes

Manufacturing of high-loading electrodes can be challenging and alternative ways of coating defect-free layers need to be investigated. A technique that has strong roots in the paint and textile industry is multi-layer coating. It is a simultaneous or subsequent application of dispersion layers on a substrate. In battery electrode fabrication, this can be realised by either slot-die or knife coating (Figure 1.6). For the slot-die coating technique, two or more slurries are coated at the same time. The die has two nozzles, connected to separate slurry tanks, so slurries with different material compositions can be coated on top of one another. Since liquid diffusion is already happening pre-drying, the formation of a distinct interface between the different layers can be avoided. A big advantage here is, that only one drying unit is needed saving a lot of time and cost in production. Unfortunately, this can still cause issues like binder migration and foil curling for thick coatings, limiting the maximum loading of the electrode. Some effects can be counteracted by proper choice of material ratios in the slurries, e.g. high binder content in the bottom-layer slurry to suppress delamination. Doctor blade coating on the other hand has a drying step in between each layer application. This is also the biggest advantage of this method. All negative effects of thick coatings can be circumvented, with this method — leading to easier fabrication of defect-free electrodes. Nevertheless, intermixing of the separately coated layers needs to be monitored, to prevent additional effects of an interfacial layer between them.

Multi-layering is a feasible way of creating 3D-like architectures into the electrode coatings. Changing the material compositions of the laminate is realisable by varying the active or inactive ingredients of the slurry. Several research groups have used this technique to create gradients of porosity [73-76], particle size [77, 78], and material components [79], in the coated layers. This can enhance the mechanical integrity as well as the electrochemical performance of the electrodes.

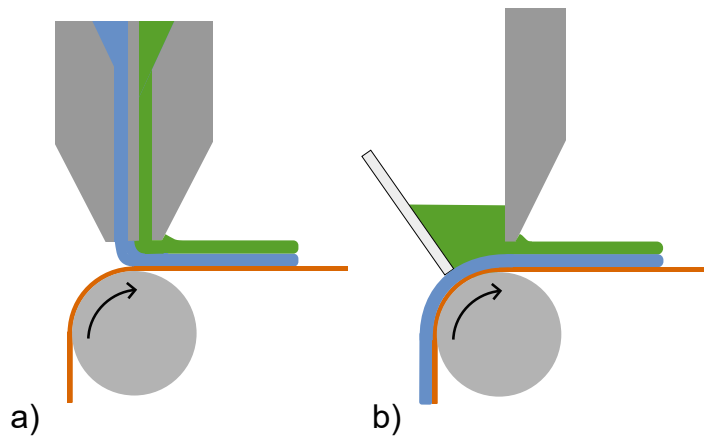


Figure 1.6: Principle and schematics of multi-layer coating for a) slot-die coating, and b) doctor blade coating

Materials and Methods

2.1 Electrode Manufacturing and Analysis

Optimizing the process of electrode manufacturing and transitioning to a more sustainable fabrication process were the main objectives of this thesis. The final slurry recipes and corresponding mixing procedures and coating parameters are published in **Publication I and II**. They are briefly described in this chapter together with all relevant analysis techniques.

2.1.1 Slurry Mixing

All samples consist of the same material components, however in different ratios. $\text{LiNi}_{0.8}\text{Mn}_{0.1}\text{Co}_{0.1}\text{O}_2$ (NMC811) (BASF SE) with an average secondary particle size of $d_{\text{avg}} = 7.8 \mu\text{m}$ was the investigated active material (AM). Carbon black (CB) (C-ENERGYTM SUPER C65, TIMCAL Ltd.) with an average particle size of $d_{\text{avg}} = 37 \text{ nm}$ and artificial graphite (C-ENERGYTM KS6L, TIMCAL Ltd.; $d_{\text{avg}} = 3.5 \text{ nm}$) were used as conductive agents. A combination of Na-carboxy-methyl-cellulose (CMC) (WALOCELTM CRT 2000 PA, DuPont de Nemours Inc.) and polymethyl acrylate (PMA) (ENEOS Cathode Binder, ENEOS Materials Belgium BV) formed the binder complex. Deionized

water was used as a solvent for all slurries. Phosphoric acid (H_3PO_4) was added for pH stabilisation. In total four different slurries were prepared. For all the single-layer electrodes with various thicknesses and the multi-layer sample without binder reduction, a weight ratio of 92:3:2:1:2 (AM:CB:KS6L:CMC:PMA) was used. For the multi-layer samples with binder modification in the top layer, a reduction of PMA of 50%, 25% and 0% of its initial value was implemented, which are referred to as 50PMA, 25PMA, and 0PMA from here on, respectively. The reduction of PMA caused a slight increase of the other material components. Table 2.1 lists the final slurry formulations.

Table 2.1: Total amount of active material (AM), carbon black (CB), graphite additive (KS6L), Na-carboxymethyl-cellulose (CMC), and polymethyl acrylate (PMA) used in different electrodes: single-layer (SL), multi-layer (ML), and binder-reduced samples (50PMA, 25PMA & 0PMA)

	SL & ML	50PMA	25PMA	0PMA
AM (wt%)	92.00	92.47	92.70	92.94
CB (wt%)	3.00	3.015	3.025	3.03
KS6L (wt%)	2.00	2.01	2.017	2.02
CMC (wt%)	1.00	1.005	1.008	1.01
PMA (wt%)	2.00	1.50	1.25	1.00

First mixing trials were conducted on a small scale (~ 25 g) in a centrifugal mixer (ARE-250 CE, Thinky Corporation) to find optimal material ratios, mixing sequence, and solid content. Later, they were transferred to a temperature-controlled dissolver (DISPERMAT CV3PLUS, VMA GETZMANN GMBH) with a dispersing disc and a total slurry mass of ~ 375 g. The mixing sequence is crucial for receiving a homogeneous slurry and thus a foundation for a defect-free coating. First, CMC was dissolved in water to obtain a 2 wt% solution. Carbon black and artificial graphite are added stepwise, with mixing in between. Due to the hygroscopicity of the carbonaceous components, thorough mixing of 20 min with high mixing speed (2000 rpm) was performed to minimise the risk of agglomerate formation. 0.16 g of 1M H_3PO_4 per g of active material was added dropwise under constant stirring, to prevent local minima of the pH, followed by a 2 min mixing step at 2000 rpm. NMC811 was added and mixed under high shear force

(3000 rpm) for 8 min. Finally, the polymethyl acrylate was added and slowly mixed at 500 rpm for 2 min to ensure that the polymer chains of **PMA** stay intact. The solid content of the slurry was 60 % and pH was measured to be 7.6. Figure 2.1 shows the sequence of mixing including relevant mixing parameters.

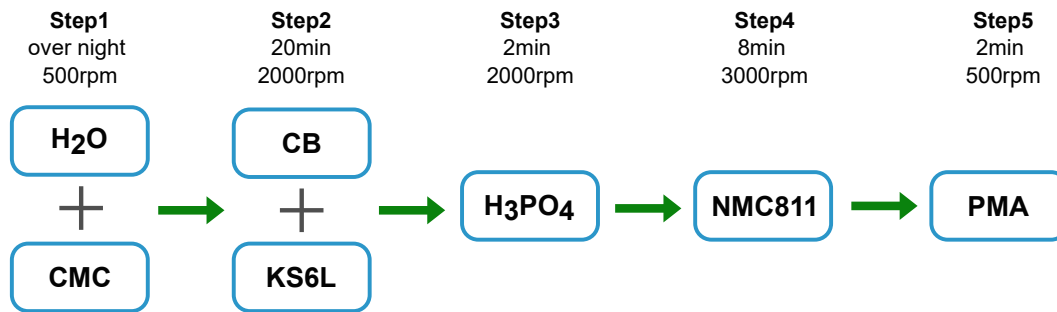


Figure 2.1: Mixing sequence of the slurry components including step times and rotational speeds of the dissolver disc.

2.1.2 Coating and Calendering

All coatings were performed on a roll-to-roll coating machine (SC 30, COATEMA Coating Machinery GmbH) with a doctor blade casting device. An aluminium foil (Norsk Hydro ASA) of 22 μm thickness was used as substrate. Coating gaps were set between 100 and 550 μm for the tortuosity study on thickness dependency. For the high-loading cathodes wet coating thicknesses were 550 μm for **SL** coatings, 250 μm for the bottom layer of the **ML** cast, and 330 μm for the top layer. The three-segment drying unit was set to the temperature profile of 45°C, 55°C, and 50°C with a drying time of 3 min per sector and a coating speed of 0.3 m min^{-1} .

Density values ρ_i of the raw materials and their shares in the coating p_i were used to determine the physical density ρ_{ph} of the coating (Equation 2.1). Discs of 15 mm diameter were punched out and their masses m_c and volumes V_c were used to receive the coating density ρ_c . As-coated porosities ε of the electrodes were calculated using equations 2.1-2.3. All cathodes are calendered to a final porosity of 40 %.

$$\rho_{ph} = \sum_i p_i \rho_i, \quad (2.1)$$

$$\rho_c = \frac{m_c}{V_c}, \quad (2.2)$$

$$\varepsilon = 1 - \frac{\rho_c}{\rho_{ph}}. \quad (2.3)$$

2.2 Electrochemical Testing

2.2.1 Constant Current Constant Voltage Cycling (CCCV)

Constant current constant voltage cycling (CCCV) cycling is a standard technique to define cycling performance in lithium-ion battery research. A constant current (CC) is applied to charge the battery until an upper cut-off cell potential is reached. This threshold voltage is kept constant until the resulting current reaches a predefined lower limit or if a predetermined maximum time is exceeded. At this point, a negative constant current is applied, to discharge the battery to a lower cut-off voltage. Typical voltage and current profiles of a CCCV charge and CC discharge cycle are displayed in Figure 2.2. The charge process can be divided into a galvanostatic and a potentiostatic phase, which can give insights into the share both processes have during the charging step. Large potentiostatic charge can indicate high ohmic resistances caused by high internal resistances in the system (e.g. electrodes, electrolyte). The resulting charge and discharge capacities (Q) can be calculated by integrating the time-dependent current $i(t)$ (Equation 2.4) within the cycling boundaries (a & b).

$$Q = \int_a^b i(t) dt \quad (2.4)$$

For an easy comparison of cells with differing nominal capacities, cycling at different current rates (C-rates) is common. C-rates are defined as nominal capacity per hour.

For example, a C-rate of 1 C means that a cell is fully charged/discharged within 1 h, 0.5 C would be 2 h, accordingly. Unfortunately, degradation effects during cycling lead to lower discharge capacity values. Typically, a reduction charge/discharge capacity can be noticed for higher current densities. To evaluate this effect, a rate-capability test can be performed, to test the cycling behaviour for multiple C-rates. Such a test was performed in the scope of this work for all high-loading electrodes using C-rates from 0.1, 0.2, 0.5 up to 1C, to investigate the specific discharge capacity with respect to the applied current.

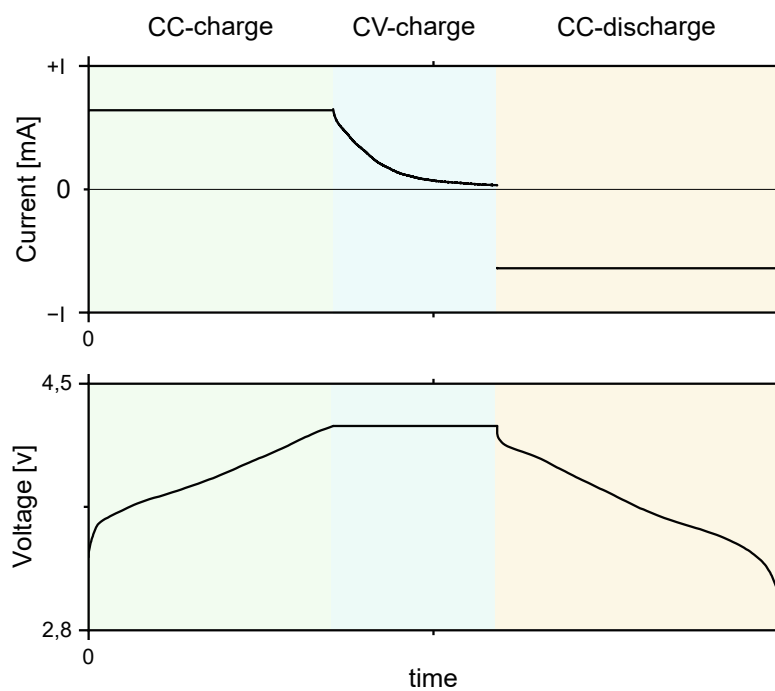


Figure 2.2: Typical voltage and current profile for a CCCV charge and CC discharge cycle.

2.2.2 Electrochemical Impedance Spectroscopy

Electrochemical impedance spectroscopy (EIS) is a powerful analysis tool in LIB research. With performing an EIS measurement on a battery cell, the total cell resistance can be divided into the shares rooting from the bulk, interfacial layers, charge transfer and

diffusion processes. For the separation of the resistance contributions, an equivalent circuit needs to be selected that represents the present physical conditions as closely as possible. For a proper representation of a battery system elements in addition to resistances (R), capacitors (C) and inductions (L) are necessary. The non-ideal capacitative behaviour of electrical double layers (which are formed for example between the electrode and electrolyte) can be described using constant phase elements (CPE) and Li-ion diffusion processes are represented by so-called Warburg elements (W). Typically, a sinusoidal AC voltage is applied, and the current response is measured, in a defined frequency range. The frequency dependence of the individual elements can be linked to their contribution to the total resistance. [80]

Blocking Electrode Experiments

EIS can also be used to analyse processes where no charge transfer occurs through an interface - so-called non-Faradaic processes. [81] In the case of a Li-ion battery, for example between an electrode and the electrolyte. It can give valuable information on the electrode's morphologies, through the determination of the ionic resistance (R_{ion}) of the electrode.

A transmission-line model (TLM) can be used to describe the porous system of an electrode filled with electrolyte. The general equivalent circuit of such a porous electrode is displayed in Figure 2.3a, where the liquid and the solid parts are represented by a series of ohmic resistors, R_{ion} and R_{eon} respectively. [82] The interface between the solid and liquid phase is represented by the electrical double layer (C_{dl}) and the charge transfer resistance (R_{ct}). In blocking conditions, no charge transfer occurs between active material particles and electrolyte, and R_{ct} can be omitted. For LIB electrodes, the electrical conductivity in the solid is many times higher than the ionic conductivity of the liquid and thus R_{eon} can be neglected. This results in a simplified transmission-line model (TLM-Q) for blocking conditions (Figure 2.3 b). Landesfeind et al. [82] showed that a simplified transmission line model can be selected as an equivalent circuit for the detailed analysis of symmetric cells in a blocking state, with a non-intercalating electrolyte (Figure

2.3).

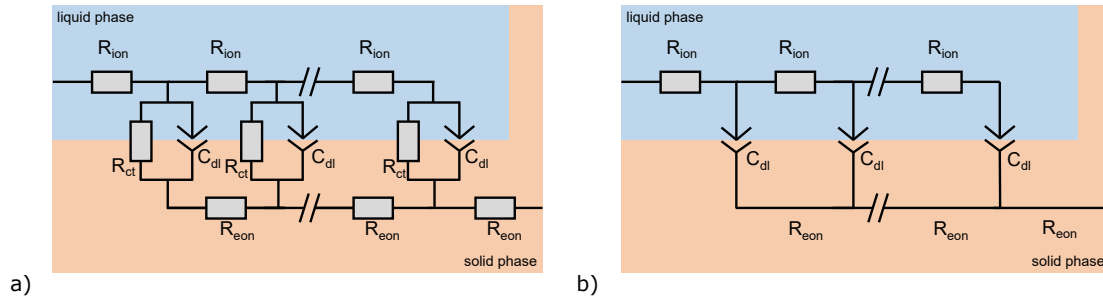


Figure 2.3: Equivalent circuits of a) the transmission line model (TLM) for faradaic processes, b) the simplified transmission line model (TLM-Q) for blocking conditions in a reflective state. [13]

Equation 2.5 is the corresponding formula for calculating the impedance Z for a TLM-Q. R_{ion} represents the ionic resistance and Q is the total constant-phase capacitance of the model. α is the constant phase exponent, ω is the angular frequency, and i is the imaginary unit.

$$Z(\omega) = \sqrt{\frac{R_{ion}}{Q(i\omega)^\alpha}} \coth \left(L \sqrt{R_{ion} Q (i\omega)^\alpha} \right). \quad (2.5)$$

A fast but decent approximation of the ionic resistance (R_{ion}) can also be determined by analyzing the x-axis offset of the high (R_{hfr}) and low-frequency regions in the Nyquist plot. [83] For $\omega \rightarrow 0$ the limiting values of the $Z'(\omega)$ and $Z''(\omega)$ simplify to Equation 2.6 and 2.7. [84]

$$Z'(\omega \rightarrow \infty) = \frac{R_{ion}}{3} + R_{hfr}, \quad (2.6)$$

$$Z''(\omega \rightarrow \infty) = 0 \quad (2.7)$$

The electrodes' tortuosity can be calculated with the knowledge of the layer thickness d , the porosity ε , the area of the investigated substrate A , the electrical conductivity of the electrolyte κ , and the ionic resistance R_{ion} (Equation 2.8).

$$\tau = \frac{R_{ion}A\kappa\varepsilon}{2d} \quad (2.8)$$

This measurement requires symmetrical cells - two electrodes of the same material facing each other and an electrolyte that does not enable a Faradaic reaction within a certain voltage range, so no charge transfer happens. A typical spectrum of a cell in a blocking state can be separated into a high and low-frequency region (Figure 2.4).

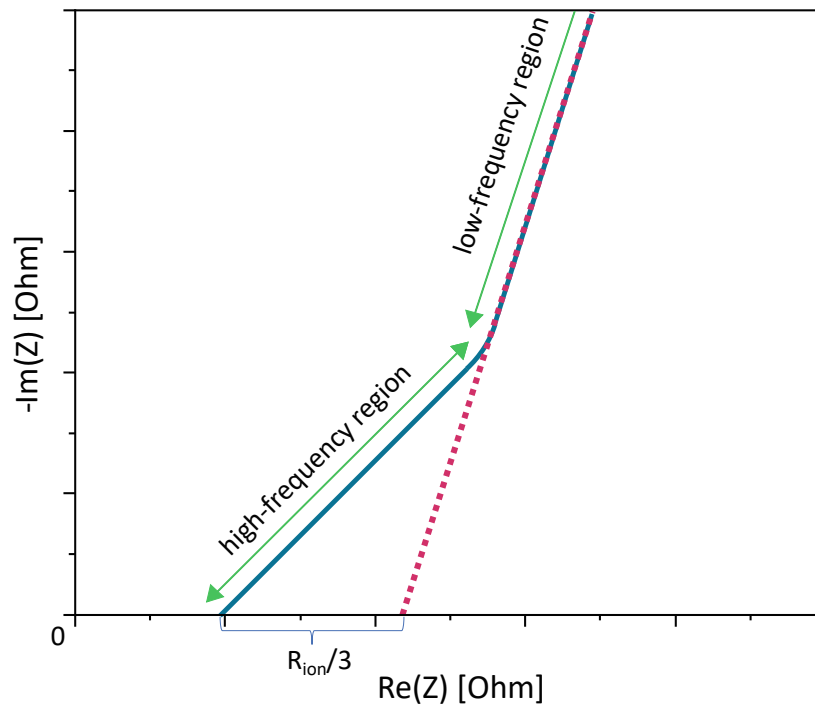


Figure 2.4: A typical spectrum of a symmetric cell in blocking condition showing the high and low frequency regions.

The parameters for all performed measurements in the blocking stage were as follows.

The frequency range was set between 500 kHz and 100 mHz with an amplitude of 10 mV, to ensure, that no charge transfer occurs during the measurement carried out in this thesis. The analysis of the performed measurements was done in two ways. On the one hand, with a **TLM-Q** model fit and on the other hand, with a linear fit of relevant regions. **[82]**

2.2.3 Cell assembly

Cycling tests were performed in a full-cell configuration against graphite anodes. Water-based fabrication of graphite anodes with the required loading and thickness are also very prone to show defects. Therefore, **NMP** was used as a solvent to minimise the potential influence on the cycling performance stemming from the counter electrode. The areal loading of the anodes was 9.5 mAhcm^{-2} , resulting in an N/P ratio of approximately 1.1 for all samples. Coin cells of type 2032 were assembled in an Ar-filled glovebox. Figure **2.5a** shows the order of additional cell components; a 1.5 mm stainless steel spacers, a 1.1 mm wave spring, and a trilayer polypropylene/polyethylene/polypropylene separator (Celgard 2500). 150 μL of 1M LiPF_6 in 3:7 EC:EMC + 2 wt% VC were used as electrolyte. Coin cells for tortuosity measurements were assembled with two cathodes facing each other (Figure **2.5b**). The number of stainless steel spacers was adapted depending on the thickness of the electrodes. The used electrolyte consisted of ethylene carbonate (EC) and dimethyl carbonate (DMC) in a 1:1 (w:w) mixture with 20 mM tetrabutylammonium perchlorate (TBAClO_4), to ensure a blocking behaviour.

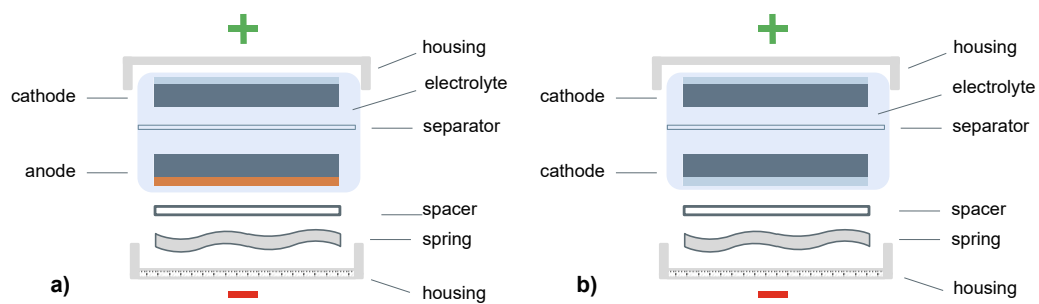


Figure 2.5: Structure and components of a coin cell in a) full-cell configuration (anode and cathode) and b) symmetric configuration (2 identical electrodes).

Results and Discussion

Key results and findings of the three publications will be displayed and shortly discussed in this chapter.

3.1 Thick electrode processing

Publications I & II focus on optimising, analysing and adapting the production process of water-based **NMC811** cathodes with high active material loading. The transformation of the production process from a laboratory scale to an upscaled roll-to-roll coating line while maintaining defect-free layers with increased thickness was performed for all investigated samples. Single and multi-layer samples with thicknesses around 200 μm and areal capacities of $\sim 8.6 \text{ mAh cm}^{-2}$ were produced (exact values are displayed in Table **3.1**).

A vast improvement independently from the C-rate can be seen in the specific discharge capacity between SL and **ML** samples (Figure **3.1** & Table **3.2**). The largest improvements are achieved for low current densities at 0.1C. Specific discharge capacities of 144 mAh/g and 176 mAh/g are reached for **SL** and **ML** electrodes, respectively, which implies an improvement of 22%. This was accomplished solely by changing the coating method

3. RESULTS AND DISCUSSION

Table 3.1: Comparison of electrode types concerning their thickness and areal capacity

Electrode Type	Total Electrode Thickness [μm]	Areal Capacity [mAh cm^{-2}]
SL	202 ± 2	8.60 ± 0.10
ML	208 ± 4	8.60 ± 0.20
50PMA	198 ± 5	8.51 ± 0.15
25PMA	200 ± 5	8.58 ± 0.10
0PMA	200 ± 4	8.52 ± 0.20

from a single to a multi-layer approach. Implementing a gradient in binder concentration further enhances the performance for higher current densities at the rate-capability test. For a C-rate of 1C an increase in specific discharge capacity of 18% and 37% was achieved compared to the **ML** and the **SL** electrodes, respectively, for the best-performing 25PMA sample.

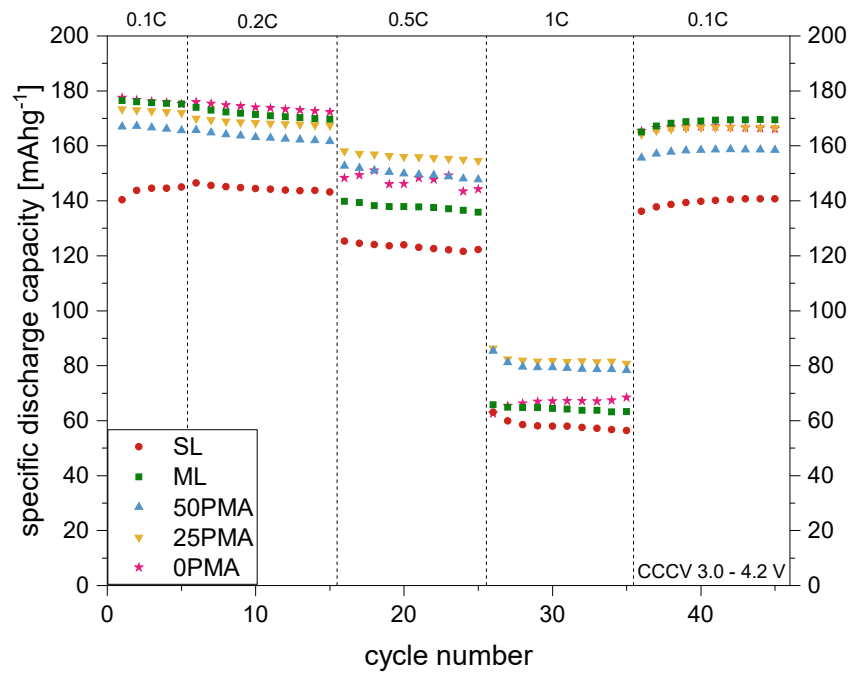


Figure 3.1: Results from the rate-capability test for the specific discharge capacity in a full cell configuration. [11, 12]

The combination of scanning electron microscopy (SEM) images, Raman spectroscopy and

Table 3.2: Specific discharge capacities for different C-rates. [11, 12]

C-rate	specific discharge capacity [mAh g ⁻¹]				
	SL	ML	50PMA	25PMA	0PMA
0.1C	144 ± 6.6	176 ± 0.44	167 ± 1.3	173 ± 4.7	176 ± 1.8
0.2C	146 ± 4.4	171 ± 0.63	163 ± 2.24	158 ± 6.5	174 ± 1.4
0.5C	128 ± 6.4	138 ± 9.8	150 ± 1.8	156 ± 4.7	148 ± 2.5
1C	59 ± 6.8	64 ± 9.1	80 ± 3.1	82 ± 7.1	67 ± 0.4
0.1C	139 ± 7.5	170 ± 2.5	159 ± 0.6	169 ± 6.7	169 ± 0.9

electrochemical impedance spectroscopy reveals differences in the samples with differing binder concentrations in the top layer. Inspection of the SEM top-view images (Figure 3.2) of 25PMA and 0PMA samples show a significant difference in the material composition. Exemplary elements are coloured in Figure 3.2b (NMC811 secondary particles in purple, carbon black in yellow and graphite additive in green). This observation is also in accordance with higher Raman peak intensities of the 25PMA and 50PMA samples at wavelengths corresponding to carbon species. It appears, that a well-established carbon-binder-domain — a conglomerate of binder and carbon components — is present in the top layer of the coating. The CBD is necessary to maintain a conductive network between the active material particles, which is particularly important for higher current densities and explains the superior cycling performance of 25PMA and 50PMA at a C-rate of 1C. A sufficient amount of binder is necessary to form a continuous interconnection in the electrode layer and to maximise the accessible active surface.

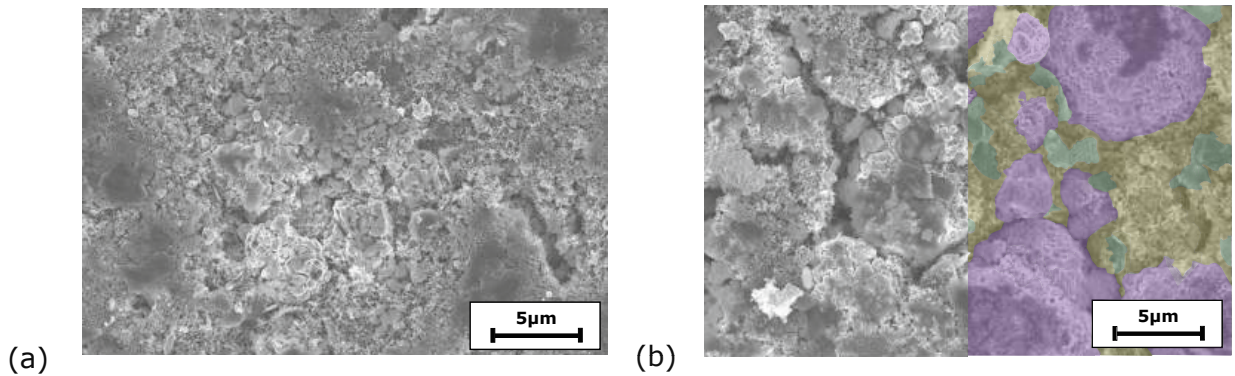


Figure 3.2: Top-view SEM images of a) 25PMA and b) 0PMA samples. [12]

3.2 Tortuosity Evaluation

The main objectives of **Publication III** were to identify if a dependency of layer thickness and tortuosity (τ) is present and if the multi-layer structure can improve this critical parameter. **EIS** measurements revealed that for the investigated **NMC811** electrodes, a drastic increase in ionic resistance in the coating happens after a threshold thickness of around 150 μm is reached. Below, the value of τ was determined to be fluctuating around 5. At the same time, the thickest layer showed a tortuosity of ~ 13 (Figure 3.3 a). With tortuosity being an intrinsic material parameter — which should be independent of layer-thickness if the material distribution stays the same in all layer directions — changes in the electrode morphology occur during fabrication. Electrodes produced with the multi-layer coating technique are less tortuous, even though the slurry composition was unchanged. τ values similar to thin-layer coatings can be achieved using this method. Figure 3.3b displays the improvement of tortuosity for **ML** samples compared to **SL** electrodes. Inhomogenous distribution of material components of the coating can be suppressed - especially detrimental binder migration was prevented. Reduction of **PMA** binder concentration in the top layer helps to minimise the tortuosity even further. All binder-reduced samples are approximately in the same range, with 25PMA reaching the

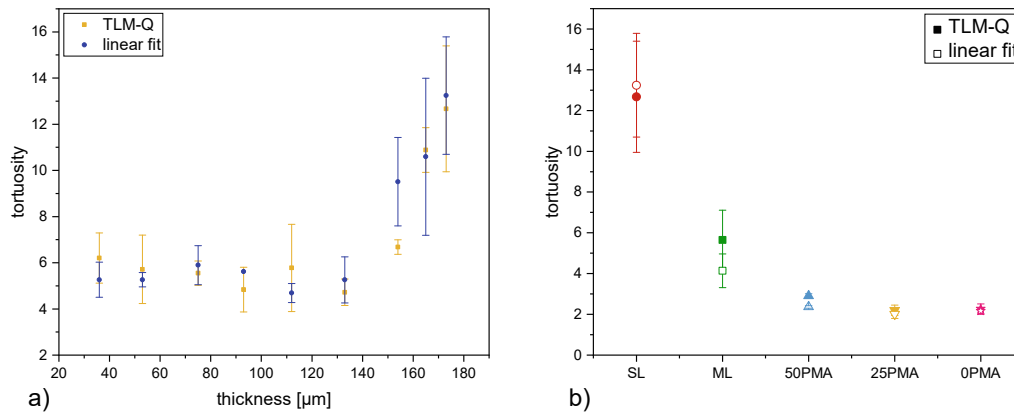


Figure 3.3: a) Thickness dependency of the tortuosity b) tortuosity for SL and ML samples with reduced binder content. [13]

lowest value at $\tau = 2$. The combination of SEM analysis and rheological measurements show that slurries have a higher tendency for particle aggregation when the concentration in the acrylic binder is increased. Correlating the rate capability results from **Publication I & II** with the received tortuosity values reveals a strong negative correlation between the specific discharge capacity of the high-loading samples and the electrode tortuosities. Thus it can be used as a performance indicator for electrode manufacturing.

An additional aspect of this study was to compare two different methods to evaluate the ionic resistance from the received impedance spectra, which were explained previously. The results show that for an industrial production setting a rough tortuosity estimation can be made using the simpler linear fitting method. However, for a more in-depth analysis, a more elaborate investigation can be employed.

Conclusion

Innovative ways of coating are needed to fabricate defect-free cathodes for battery applications with high loading. A transfer from a manufacturing process based on organic solvents to an aqueous process increases the complexity of the coating procedure and affects the electrochemical performance of such thick electrodes. Within the scope of this work, the following conclusions can be drawn.

Research question 1 (RQ1): *How can the manufacturing process be improved for high-loading electrodes?*

Multi-layer coating — subsequent coating of multiple layers on top of each other — is a promising technique for manufacturing high-loading electrodes. This technique was successfully employed, in this thesis, to fabricate thick ($>200\ \mu\text{m}$), high-loading ($>8.6\ \text{mAh}/\text{cm}^2$) NMC811 electrodes. Furthermore, it was demonstrated that all fabrication steps are upscaleable and compatible with industrially relevant roll-to-roll processes. Compared to the conventional coating of a single layer, mechanical integrity (45 % higher adhesion strength to the current collector) and cycling performance can be increased ($>20\ \%$ increase in specific discharge capacity for low current densities). Additionally, the multi-layer method was effectively used to modify the distribution of poly(methyl) acrylic binder within the coating's cross-section. Reducing the binder material and

creating concentration gradients lead to additional improvements in the electrochemical performance. Especially for current densities of 1C, an increase in specific discharge capacity of 37% compared to single-layer cathodes was achieved.

Particularly when producing thick electrodes, attention must be paid to a homogeneous distribution of the individual electrode components. Binder aggregation on the electrode surface caused by migration during drying can be reduced using the multi-layer coating method. Further reduction of these ion-blocking layers can be realised by introducing a binder gradient through **ML**-coating. However, a minimum amount of binder should be present to maintain the essential carbon-binder-domain and avoid an increase in electrical resistance, which can be particularly noticeable at higher current rates.

Research question 2 (RQ2): *How can the production process of secondary battery electrodes be made more sustainable?*

The substitution of **NMP** with water is currently state-of-the-art only in the fabrication of graphitic anodes. Within this work, an aqueous process for **NMC811** cathodes was investigated. Phosphoric acid was used to counteract the detrimental rise in pH during slurry mixing. The conventional **NMP-PVDF** system of solvent and binder was successfully changed to a water-based process using **CMC** and **PMA** as binder materials. This results in an electrode which contains no perfluorinated compounds and is thus in accordance with the upcoming PFAS regulation. However, switching to a more sustainable aqueous process also requires adaptations of the electrode manufacturing process. Fabricating defect-free water-based electrodes demands special attention to the mixing sequence of the electrode slurry. Particularly when fabricating thick layers, careful consideration of the coating and drying parameters is essential to receive processable electrodes.

Research question 3 (RQ3): *What methods can be used to verify that a changed fabrication process positively influences the electrodes' electrochemical performance?*

Electrochemical impedance spectroscopy is a convenient method for a fast determination of the electrode tortuosity. First, the dependency between the thickness of the coated layer and the electrode tortuosity was shown. A drastic increase in tortuosity happens

after a certain thickness threshold is exceeded. Whereas, thinner layers show stable tortuosity values. This effect is due to a change in the component distribution within the cross-section of the layer. A decrease in tortuosity was achieved by using the innovative multi-layer coating technique. Additionally, further improvements were made, by reducing the binder content in the layer close to the separator, to 25 % of the initial amount of **PMA** used in non-modified ML samples. For 200 μm thick electrodes (8.6 mAh/cm^2) tortuosity was reduced from 12.7 to 2.2 (decrease of $> 80 \%$) by introducing a binder concentration gradient through multi-layer coating. In addition, a negative correlation was found between the electrode tortuosity and the specific discharge capacity independent of the current density. A simple linear fit of the **EIS** spectra has proven to be reliable for a fast evaluation of thickness-dependent tortuosity thresholds for electrode coatings.

In summary, an answer to the general research question (RG): *How can the energy density of Li-ion secondary batteries be increased* can be given. An increase in energy density can be achieved by using the multi-layer coating technique during the electrode production process and fine-tuning the binder concentration in the coated layer.

Outlook

The drive to maximise the energy density of existing Li-ion technologies will continue to enforce the demand for further developing creative and innovative solutions for electrode fabrication. The multi-layer coating method is a promising solution for optimising the production of high-loading electrodes as it can be implemented in existing processes with little effort. Transferring to a multi-stage coating process also allows additional flexibility in the material composition of the electrodes. It is a key enabler in expanding the process limitations for ultra-thick coating layers. Especially the fast charging capability of thick electrodes could be improved by integrating a 3D-like electrode architecture and poses an important issue to tackle in future research. Implementation of multi-layer coated electrodes into cells with higher nominal capacity needs to be the logical next step in evaluating their operational capabilities. Additionally, it has to be acknowledged that electrode optimisation also needs to be performed on the anode side, to reach the full potential of the high-loading NMC811 cathodes.

Inevitably, water-based processing needs to become state-of-the-art in commercial cathode production processes. This will not only help to reduce the largest course of costs during Li-ion battery manufacturing, but also push towards more sustainable and energy-efficient fabrication processes.

5. OUTLOOK

Furthermore, the tortuosity measurements can act as an indicator to identify maximum layer thicknesses in standard (single-layer) coating processes. Due to the simplicity of the measurement technique, integration into industrial processes can be done easily. The obtained information can provide conclusions about electrochemical limitations related to the electrodes' material composition and, if necessary, indicate the need for optimisation.

List of Figures

1.1	Connection between the publications and the research questions.	5
1.2	Schematic working principle of a Li-ion battery.	7
1.3	Layered structure of LiCoO_2	9
1.4	Steps of electrode manufacturing; a) slurry mixing, b) electrode coating, c) calendaring.	9
1.5	Principle and schematics of different coating techniques, a) slot-die coating, b) doctor blade coating	11
1.6	Principle and schematics of multi-layer coating for a) slot-die coating, and b) doctor blade coating	19
2.1	Mixing sequence of the slurry components including step times and rotational speeds of the dissolver disc.	23
2.2	Typical voltage and current profile for a CCCV charge and CC discharge cycle.	25
2.3	Equivalent circuits of a) the transmission line model (TML) for faradaic processes, b) the simplified transmission line model (TML-Q) for blocking conditions in a reflective state. [13]	27
2.4	A typical spectrum of a symmetric cell in blocking condition showing the high and low frequency regions.	28
2.5	Structure and components of a coin cell in a) full-cell configuration (anode and cathode) and b) symmetric configuration (2 identical electrodes).	30
		43

3.1	Results from the rate-capability test for the specific discharge capacity in a full cell configuration. [11, 12]	32
3.2	Top-view SEM images of a) 25PMA and b) 0PMA samples. [12]	34
3.3	a) Thickness dependency of the tortuosity b) tortuosity for SL and ML samples with reduced binder content. [13]	35

List of Tables

2.1	Total amount of active material (AM), carbon black (CB), graphite additive (KS6L), Na-carboxymethyl-cellulose (CMC), and polymethyl acrylate (PMA) used in different electrodes: single-layer (SL), multi-layer (ML), and binder-reduced samples (50PMA, 25PMA & 0PMA)	22
3.1	Comparison of electrode types concerning their thickness and areal capacity	32
3.2	Specific discharge capacities for different C-rates. [11] [12]	33

Acronyms

AM active material. [21](#), [22](#)

CB Carbon black. [21](#), [22](#)

CBD carbon-binder-domain. [4](#), [14](#), [33](#)

CC constant current. [24](#)

CCCV Constant current constant voltage cycling. [24](#)

CMC sodium-carboxymethyl cellulose. [13](#), [21](#), [22](#), [38](#)

EIS electrochemical impedance spectroscopy. [4](#), [25](#), [26](#), [34](#), [39](#)

EVs electric vehicles. [1](#)

H₃PO₄ Phosphoric acid. [22](#)

LCO Lithium cobalt oxide. [7](#), [8](#)

LIB lithium-ion battery. [1](#), [2](#), [15](#), [25](#), [26](#)

LiOH lithium hydroxide. [14](#)

ML multi-layer. [4](#), [23](#), [31](#), [32](#), [34](#), [38](#)

NCA LiNi_xCo_yAl_zO₂. [8](#)

NMC nickel manganese cobalt oxides. [8](#)

NMC811 $\text{LiNi}_{0.8}\text{Mn}_{0.1}\text{Co}_{0.1}\text{O}_2$. [3](#), [4](#), [21](#), [22](#), [31](#), [33](#), [34](#), [37](#), [38](#)

NMP N-methyl-2-pyrrolidone. [2](#), [3](#), [10](#), [12–14](#), [29](#), [38](#)

PFAS per- and poly-fluoroalkyl substances. [2](#)

PMA polymethyl acrylate. [21–23](#), [34](#), [38](#), [39](#)

PVDF polyvinylidene difluoride. [2](#), [13](#), [38](#)

SEM scanning electron microscopy. [32](#), [33](#), [35](#)

SL single-layer. [4](#), [23](#), [31](#), [32](#), [34](#)

TLM transmission-line model. [26](#)

TLM-Q simplified transmission-line model. [26](#), [29](#)

TRL technology readiness level. [12](#)

Bibliography

- [1] T Nagaura. Lithium ion rechargeable battery. *Progress in Batteries & Solar Cells*, 9:209, 1990.
- [2] Chengjian Xu, Qiang Dai, Linda Gaines, Mingming Hu, Arnold Tukker, and Bernhard Steubing. Future material demand for automotive lithium-based batteries. *Communications Materials*, 1(1):99, 2020.
- [3] Nikita Akhmetov, Anton Manakhov, and Abdulaziz S Al-Qasim. Li-ion battery cathode recycling: An emerging response to growing metal demand and accumulating battery waste. *Electronics*, 12(5):1152, 2023.
- [4] Ming Wang, Dingying Dang, Andrew Meyer, Renata Arsenault, and Yang-Tse Cheng. Effects of the mixing sequence on making lithium ion battery electrodes. *Journal of The Electrochemical Society*, 167(10):100518, 2020.
- [5] Ritu Sahore, David L Wood III, Alexander Kukay, Kelsey M Grady, Jianlin Li, and Ilias Belharouak. Towards understanding of cracking during drying of thick aqueous-processed $\text{LiNi}_{0.8}\text{Mn}_{0.1}\text{Co}_{0.1}\text{O}_2$ cathodes. *ACS Sustainable Chemistry & Engineering*, 8(8):3162–3169, 2020.
- [6] David L Wood, Jeffrey D Quass, Jianlin Li, Shabbir Ahmed, David Ventola, and Claus Daniel. Technical and economic analysis of solvent-based lithium-ion electrode drying with water and nmp. *Drying technology*, 36(2):234–244, 2018.

- [7] David L Wood III, Jianlin Li, and Claus Daniel. Prospects for reducing the processing cost of lithium ion batteries. *Journal of Power Sources*, 275:234–242, 2015.
- [8] Silje Nornes Bryntesen, Anders Hammer Strømman, Ignat Tolstorebrov, Paul R Shearing, Jacob J Lamb, and Odne Stokke Burheim. Opportunities for the state-of-the-art production of lib electrodes—a review. *Energies*, 14(5):1406, 2021.
- [9] Jianlin Li, Zhijia Du, Rose E Ruther, Seong Jin An, Lamuel Abraham David, Kevin Hays, Marissa Wood, Nathan D Phillip, Yangping Sheng, Chengyu Mao, et al. Toward low-cost, high-energy density, and high-power density lithium-ion batteries. *Jom*, 69(9):1484–1496, 2017.
- [10] Naresh Susarla, Shabbir Ahmed, and Dennis W Dees. Modeling and analysis of solvent removal during li-ion battery electrode drying. *Journal of Power Sources*, 378:660–670, 2018.
- [11] Lukas Neidhart, Katja Fröhlich, Nicolas Eshraghi, Damian Cupid, Franz Winter, and Marcus Jahn. Aqueous manufacturing of defect-free thick multi-layer nmc811 electrodes. *Nanomaterials*, 12(3):317, 2022.
- [12] Lukas Neidhart, Katja Fröhlich, Franz Winter, and Marcus Jahn. Implementing binder gradients in thick water-based nmc811 cathodes via multi-layer coating. *Batteries*, 9(3):171, 2023.
- [13] L Neidhart, K Fröhlich, B Boz, F Winter, and M Jahn. Layer by layer: Improved tortuosity in high loading aqueous nmc811 electrodes. *Journal of The Electrochemical Society*, 171(5):050532, 2024.
- [14] Andreas Jossen, Wolfgang Weydanz, et al. Moderne akkumulatoren richtig einsetzen. 2006.
- [15] Kenji Fukuda, Kazuhiko Kikuya, Kennichi Isono, and Masaki Yoshio. Foliated natural graphite as the anode material for rechargeable lithium-ion cells. *Journal of power sources*, 69(1-2):165–168, 1997.

- [16] Michael Holzapfel, Hilmi Buqa, Laurence J Hardwick, Matthias Hahn, Andreas Würsig, Werner Scheifele, Petr Novák, Rüdiger Kötz, Claudia Veit, and Frank-Martin Petrat. Nano silicon for lithium-ion batteries. *Electrochimica acta*, 52(3):973–978, 2006.
- [17] Hui Wu and Yi Cui. Designing nanostructured si anodes for high energy lithium ion batteries. *Nano today*, 7(5):414–429, 2012.
- [18] Jie Chen, Huiping Yang, Tianhao Li, Chaoyang Liu, Hui Tong, Jiabin Chen, Zengsheng Liu, Lingfeng Xia, Zhaoyong Chen, Junfei Duan, et al. The effects of reversibility of h2-h3 phase transition on ni-rich layered oxide cathode for high-energy lithium-ion batteries. *Frontiers in chemistry*, 7:500, 2019.
- [19] Zhaojin Li, Mengjiao Du, Xu Guo, Di Zhang, Qiujun Wang, Huilan Sun, Bo Wang, and Yimin A Wu. Research progress of six-based anode materials for lithium-ion batteries. *Chemical Engineering Journal*, page 145294, 2023.
- [20] Meiqing Guo, Xiaogang Zhang, Weijia Meng, Xiao Liu, Genwei Wang, Zhongchao Bai, Zhihua Wang, and Fuqian Yang. Electrochemical performance and morphological evolution of hollow sn microspheres. *Solid state ionics*, 325:120–127, 2018.
- [21] Danni Lei, Ming Zhang, Baihua Qu, Jianmin Ma, Qihong Li, Libao Chen, Binggan Lu, and Taihong Wang. Hierarchical tin-based microspheres: Solvothermal synthesis, chemical conversion, mechanism and application in lithium ion batteries. *Electrochimica Acta*, 106:386–391, 2013.
- [22] K Mizushima, PC Jones, PJ Wiseman, and John B Goodenough. Lixco₂ (0 < x ≤ 1): A new cathode material for batteries of high energy density. *Solid State Ionics*, 3:171–174, 1981.
- [23] Michel Armand, Peter Axmann, Dominic Bresser, Mark Copley, Kristina Edström, Christian Ekberg, Dominique Guyomard, Bernard Lestriez, Petr Novák, Martina Petranikova, et al. Lithium-ion batteries—current state of the art and anticipated developments. *Journal of Power Sources*, 479:228708, 2020.

- [24] Eunmi Jo, Jae-Ho Park, Junbeom Park, Jieun Hwang, Kyung Yoon Chung, Kyung-Wan Nam, Seung Min Kim, and Wonyoung Chang. Different thermal degradation mechanisms: Role of aluminum in ni-rich layered cathode materials. *Nano Energy*, 78:105367, 2020.
- [25] Marcel Schmitt, Ralf Diehm, Philip Scharfer, and Wilhelm Schabel. An experimental and analytical study on intermittent slot die coating of viscoelastic battery slurries. *Journal of Coatings Technology and Research*, 12:927–938, 2015.
- [26] Marcel Schmitt, Michael Baunach, Lukas Wengeler, Katharina Peters, Pascal Junges, Philip Scharfer, and Wilhelm Schabel. Slot-die processing of lithium-ion battery electrodes—coating window characterization. *Chemical Engineering and Processing: Process Intensification*, 68:32–37, 2013.
- [27] Zhijia Du, KM Rollag, Jianlin Li, Seong Jin An, Marissa Wood, Yangping Sheng, PP Mukherjee, Claus Daniel, and DL Wood Iii. Enabling aqueous processing for crack-free thick electrodes. *Journal of Power Sources*, 354:200–206, 2017.
- [28] Ye Shui Zhang, Nicola E Courtier, Zhenyu Zhang, Kailong Liu, Josh J Bailey, Adam M Boyce, Giles Richardson, Paul R Shearing, Emma Kendrick, and Dan JL Brett. A review of lithium-ion battery electrode drying: mechanisms and metrology. *Advanced Energy Materials*, 12(2):2102233, 2022.
- [29] Mohanad Al-Shroofy, Qinglin Zhang, Jiagang Xu, Tao Chen, Aman Preet Kaur, and Yang-Tse Cheng. Solvent-free dry powder coating process for low-cost manufacturing of $\text{LiNi}_{1/3}\text{Mn}_{1/3}\text{Co}_{1/3}\text{O}_2$ cathodes in lithium-ion batteries. *Journal of Power Sources*, 352:187–193, 2017.
- [30] Maria Montanino, Giuliano Sico, Anna De Girolamo Del Mauro, and Margherita Moreno. Lfp-based gravure printed cathodes for lithium-ion printed batteries. *Membranes*, 9(6):71, 2019.
- [31] Paul Baade and Vanessa Wood. Ultra-high throughput manufacturing method for composite solid-state electrolytes. *Iscience*, 24(2), 2021.

- [32] A Gören, J Mendes, HM Rodrigues, RE Sousa, J Oliveira, L Hilliou, CM Costa, MM Silva, and S Lanceros-Méndez. High performance screen-printed electrodes prepared by a green solvent approach for lithium-ion batteries. *Journal of Power Sources*, 334:65–77, 2016.
- [33] David Schreiner, Maximilian Oguntke, Till Günther, and Gunther Reinhart. Modelling of the calendaring process of nmc-622 cathodes in battery production analyzing machine/material–process–structure correlations. *Energy Technology*, 7(11):1900840, 2019.
- [34] Charles F Oladimeji, Pedro L Moss, and Mark H Weatherspoon. Analyses of the calendaring process for performance optimization of li-ion battery cathode. *Advances in Chemistry*, 2016(1):7395060, 2016.
- [35] Honghe Zheng, Li Tan, Gao Liu, Xiangyun Song, and Vincent S Battaglia. Calendaring effects on the physical and electrochemical properties of li [ni₁/3mn₁/3co₁/3]o₂ cathode. *Journal of Power Sources*, 208:52–57, 2012.
- [36] Yangping Sheng, Christopher R Fell, Yong Kyu Son, Bernhard M Metz, Junwei Jiang, and Benjamin C Church. Effect of calendaring on electrode wettability in lithium-ion batteries. *Frontiers in Energy Research*, 2:56, 2014.
- [37] Jeong Hoon Park, Sun Hyung Kim, and Kyung Hyun Ahn. Role of carboxymethyl cellulose binder and its effect on the preparation process of anode slurries for li-ion batteries. *Colloids and Surfaces A: Physicochemical and Engineering Aspects*, 664:131130, 2023.
- [38] Ronald Gordon, Raquel Orias, and Norbert Willenbacher. Effect of carboxymethyl cellulose on the flow behavior of lithium-ion battery anode slurries and the electrical as well as mechanical properties of corresponding dry layers. *Journal of Materials Science*, 55(33):15867–15881, 2020.

- [39] Carlos G Lopez and Walter Richtering. Oscillatory rheology of carboxymethyl cellulose gels: Influence of concentration and ph. *Carbohydrate Polymers*, 267:118117, 2021.
- [40] Jin-Hyon Lee, Ungyu Paik, Vincent A Hackley, and Young-Min Choi. Effect of carboxymethyl cellulose on aqueous processing of natural graphite negative electrodes and their electrochemical performance for lithium batteries. *Journal of The Electrochemical Society*, 152(9):A1763, 2005.
- [41] A Guerfi, M Kaneko, M Petitclerc, M Mori, and K Zaghib. Lifepo4 water-soluble binder electrode for li-ion batteries. *Journal of Power Sources*, 163(2):1047–1052, 2007.
- [42] Z Karkar, D Guyomard, L Roué, and BJEALestriez. A comparative study of polyacrylic acid (paa) and carboxymethyl cellulose (cmc) binders for si-based electrodes. *Electrochimica Acta*, 258:453–466, 2017.
- [43] Jake Entwistle, Ruihuan Ge, Kunal Pardikar, Rachel Smith, and Denis Cumming. Carbon binder domain networks and electrical conductivity in lithium-ion battery electrodes: A critical review. *Renewable and Sustainable Energy Reviews*, 166:112624, 2022.
- [44] Ilya A Shkrob, James A Gilbert, Patrick J Phillips, Robert Klie, Richard T Haasch, Javier Bareño, and Daniel P Abraham. Chemical weathering of layered ni-rich oxide electrode materials: evidence for cation exchange. *Journal of The Electrochemical Society*, 164(7):A1489, 2017.
- [45] A Ya Chatalov. Effet du ph sur le comportement électrochimique des métaux et leur résistance à la corrosion. *Dokl. Akad. Naouk SSSR*, 86:775, 1952.
- [46] SY Li and BC Church. Effect of aqueous-based cathode slurry ph and immersion time on corrosion of aluminum current collector in lithium-ion batteries. *Materials and Corrosion*, 67(9):978–987, 2016.

- [47] Arefeh Kazzazi, Dominic Bresser, Agnese Birrozzi, Jan von Zamory, Maral Hekmatfar, and Stefano Passerini. Comparative analysis of aqueous binders for high-energy li-rich nmc as a lithium-ion cathode and the impact of adding phosphoric acid. *ACS applied materials & interfaces*, 10(20):17214–17222, 2018.
- [48] Alexander Kukay, Ritu Sahore, Anand Parejiya, W Blake Hawley, Jianlin Li, and David L Wood III. Aqueous ni-rich-cathode dispersions processed with phosphoric acid for lithium-ion batteries with ultra-thick electrodes. *Journal of Colloid and Interface Science*, 581:635–643, 2021.
- [49] Diogo Vieira Carvalho, Nicholas Loeffler, Guk-Tae Kim, Mario Marinaro, Margret Wohlfahrt-Mehrens, and Stefano Passerini. Study of water-based lithium titanate electrode processing: the role of ph and binder molecular structure. *Polymers*, 8(8):276, 2016.
- [50] Ines Hamam, Ning Zhang, Aaron Liu, MB Johnson, and JR Dahn. Study of the reactions between ni-rich positive electrode materials and aqueous solutions and their relation to the failure of li-ion cells. *Journal of The Electrochemical Society*, 167(13):130521, 2020.
- [51] Chia-Chen Li, Jyh-Tsung Lee, Yi-Ling Tung, and Chang-Rung Yang. Effects of ph on the dispersion and cell performance of licoo 2 cathodes based on the aqueous process. *Journal of materials science*, 42(14):5773–5777, 2007.
- [52] Werner Bauer, Fatih A Çetinel, Marcus Müller, and Ulrike Kaufmann. Effects of ph control by acid addition at the aqueous processing of cathodes for lithium ion batteries. *Electrochimica Acta*, 317:112–119, 2019.
- [53] Katsuya Kimura, Taichi Sakamoto, Takashi Mukai, Yuta Ikeuchi, Naoto Yamashita, Keiichiro Onishi, Keiichi Asami, and Masahiro Yanagida. Improvement of the cyclability and coulombic efficiency of li-ion batteries using li [ni_{0.8}co_{0.15}al_{0.05}]o₂ cathode containing an aqueous binder with pressurized co₂ gas treatment. *Journal of The Electrochemical Society*, 165(2):A16, 2018.

- [54] Yudi Kuang, Chaoji Chen, Dylan Kirsch, and Liangbing Hu. Thick electrode batteries: principles, opportunities, and challenges. *Advanced Energy Materials*, 9(33):1901457, 2019.
- [55] Madhav Singh, Jörg Kaiser, and Horst Hahn. Effect of porosity on the thick electrodes for high energy density lithium ion batteries for stationary applications. *Batteries*, 2(4):35, 2016.
- [56] Kevin G Gallagher, Stephen E Trask, Christoph Bauer, Thomas Woehrle, Simon F Lux, Matthias Tschech, Peter Lamp, Bryant J Polzin, Seungbum Ha, Brandon Long, et al. Optimizing areal capacities through understanding the limitations of lithium-ion electrodes. *Journal of The Electrochemical Society*, 163(2):A138, 2015.
- [57] Byoung-Sun Lee, Zhaohui Wu, Victoria Petrova, Xing Xing, Hee-Dae Lim, Haodong Liu, and Ping Liu. Analysis of rate-limiting factors in thick electrodes for electric vehicle applications. *Journal of The Electrochemical Society*, 165(3):A525–A533, 2018.
- [58] Lukas Ibing, Tobias Gallasch, Patricia Schneider, Philip Niehoff, Andreas Hintennach, Martin Winter, and Falko M Schappacher. Towards water based ultra-thick li ion battery electrodes—a binder approach. *Journal of Power Sources*, 423:183–191, 2019.
- [59] Lea Sophie Kremer, Alice Hoffmann, Timo Danner, Simon Hein, Benedikt Prifling, Daniel Westhoff, Christian Dreer, Arnulf Latz, Volker Schmidt, and Margret Wohlfahrt-Mehrens. Manufacturing process for improved ultra-thick cathodes in high-energy lithium-ion batteries. *Energy Technology*, 8(2):1900167, 2020.
- [60] Madhav Singh, Jörg Kaiser, and Horst Hahn. Thick electrodes for high energy lithium ion batteries. *Journal of The Electrochemical Society*, 162(7):A1196, 2015.
- [61] Stephanie Golmon, Kurt Maute, and Martin L. Dunn. A design optimization methodology for Li+ batteries. *Journal of Power Sources*, 253:239–250, 2014.

- [62] Wenquan Lu, Andrew Jansen, Dennis Dees, Paul Nelson, Nicholas R. Veselka, and Gary Henriksen. High-energy electrode investigation for plug-in hybrid electric vehicles. *Journal of Power Sources*, 196(3):1537–1540, 2011.
- [63] Kentaro Kuratani, Kaoru Ishibashi, Yoshiyuki Komoda, Ruri Hidema, Hiroshi Suzuki, and Hironori Kobayashi. Controlling of dispersion state of particles in slurry and electrochemical properties of electrodes. *Journal of The Electrochemical Society*, 166(4):A501, 2019.
- [64] Alice Hoffmann, Emanuel A Heider, Christian Dreer, Claudia Pfeifer, and Margret Wohlfahrt-Mehrens. Influence of the mixing and dispersing process on the slurry properties and the microstructure and performance of ultrathick cathodes for lithium-ion batteries. *Energy Technology*, 11(5):2200484, 2023.
- [65] Francesc Font, Bartosz Protas, Giles Richardson, and Jamie M Foster. Binder migration during drying of lithium-ion battery electrodes: Modelling and comparison to experiment. *Journal of Power Sources*, 393:177–185, 2018.
- [66] Marcus Müller, Lukas Pfaffmann, Stefan Jaiser, Michael Baunach, Vanessa Trouillet, Frieder Scheiba, Philip Scharfer, Wilhelm Schabel, and Werner Bauer. Investigation of binder distribution in graphite anodes for lithium-ion batteries. *Journal of Power Sources*, 340:1–5, 2017.
- [67] Stefan Jaiser, Marcus Müller, Michael Baunach, Werner Bauer, Philip Scharfer, and Wilhelm Schabel. Investigation of film solidification and binder migration during drying of li-ion battery anodes. *Journal of Power Sources*, 318:210–219, 2016.
- [68] Bastian G Westphal and Arno Kwade. Critical electrode properties and drying conditions causing component segregation in graphitic anodes for lithium-ion batteries. *Journal of Energy Storage*, 18:509–517, 2018.
- [69] M Baunach, S Jaiser, S Schmelzle, H Nirschl, P Scharfer, and W Schabel. Delamination behavior of lithium-ion battery anodes: Influence of drying temperature during electrode processing. *Drying Technology*, 34(4):462–473, 2016.

- [70] Bernhard Tjaden, Dan JL Brett, and Paul R Shearing. Tortuosity in electrochemical devices: a review of calculation approaches. *International Materials Reviews*, 63(2):47–67, 2018.
- [71] Zhengyu Ju, Xiao Xu, Xiao Zhang, Kasun U Raigama, and Guihua Yu. Towards fast-charging high-energy lithium-ion batteries: from nano-to micro-structuring perspectives. *Chemical Engineering Journal*, 454:140003, 2023.
- [72] Tuan-Tu Nguyen, Arnaud Demortière, Benoit Fleutot, Bruno Delobel, Charles Delacourt, and Samuel J Cooper. The electrode tortuosity factor: why the conventional tortuosity factor is not well suited for quantifying transport in porous li-ion battery electrodes and what to use instead. *npj Computational Materials*, 6(1):123, 2020.
- [73] Lin Liu, Pengjian Guan, and Changhong Liu. Experimental and simulation investigations of porosity graded cathodes in mitigating battery degradation of high voltage lithium-ion batteries. *Journal of The Electrochemical Society*, 164(13):A3163, 2017.
- [74] Yanbo Qi, Taejin Jang, Venkatasailanathan Ramadesigan, Daniel T Schwartz, and Venkat R Subramanian. Is there a benefit in employing graded electrodes for lithium-ion batteries? *Journal of The Electrochemical Society*, 164(13):A3196, 2017.
- [75] Daniel Müller, Imanol Landa-Medrano, Aitor Eguia-Barrio, Iker Boyano, Idoia Urdampilleta, Iratxe de Meatzza, Alexander Fill, and Peter Birke. Electrochemical characterization of bi-layered graphite anodes combining high and low porosity in lithium-ion cells to improve cell performance. *Electrochimica Acta*, 391:138966, 2021.
- [76] Yiling Dai and Venkat Srinivasan. On graded electrode porosity as a design tool for improving the energy density of batteries. *Journal of The Electrochemical Society*, 163(3):A406, 2015.
- [77] Marissa Wood, Jianlin Li, Zhijia Du, Claus Daniel, Alison R Dunlop, Bryant J Polzin, Andrew N Jansen, Gregory K Krumdick, and David L Wood Iii. Impact of secondary particle size and two-layer architectures on the high-rate performance

of thick electrodes in lithium-ion battery pouch cells. *Journal of Power Sources*, 515:230429, 2021.

- [78] Sergiy Kalnaus, Kelsey Livingston, W Blake Hawley, Hong Wang, and Jianlin Li. Design and processing for high performance li ion battery electrodes with double-layer structure. *Journal of Energy Storage*, 44:103582, 2021.
- [79] Michael Kespe, Susanne Cernak, Marco Gleiß, Simon Hammerich, and Hermann Nirschl. Three-dimensional simulation of transport processes within blended electrodes on the particle scale. *International Journal of Energy Research*, 43(13):6762–6778, 2019.
- [80] Woosung Choi, Heon-Cheol Shin, Ji Man Kim, Jae-Young Choi, and Won-Sub Yoon. Modeling and applications of electrochemical impedance spectroscopy (eis) for lithium-ion batteries. *Journal of Electrochemical Science and Technology*, 11(1):1–13, 2020.
- [81] PM Biesheuvel, S Porada, and JE Dykstra. The difference between faradaic and non-faradaic electrode processes. *arXiv preprint arXiv:1809.02930*, 2018.
- [82] Johannes Landesfeind, Johannes Hattendorff, Andreas Ehrl, Wolfgang A Wall, and Hubert A Gasteiger. Tortuosity determination of battery electrodes and separators by impedance spectroscopy. *Journal of The Electrochemical Society*, 163(7):A1373, 2016.
- [83] Fezzeh Pouraghajan, Hannah Knight, Michael Wray, Brian Mazzeo, Ram Subbaraman, Jake Christensen, and Dean Wheeler. Quantifying tortuosity of porous li-ion battery electrodes: Comparing polarization-interrupt and blocking-electrolyte methods. *Journal of The Electrochemical Society*, 165(11):A2644–A2653, 2018.
- [84] Masayuki Itagaki, Satoshi Suzuki, Isao Shitanda, and Kunihiro Watanabe. Electrochemical impedance and complex capacitance to interpret electrochemical capacitor. *Electrochemistry*, 75(8):649–655, 2007.

Journal Publications

Publication I

Aqueous Manufacturing of Defect-Free Thick Multi-Layer NMC811 Electrodes.

Lukas Neidhart, Katja Fröhlich, Nicolas Eshraghi, Damian Cupid, Franz Winter and Marcus Jahn.

Nanomaterials, 12(3):317, 2022; DOI:[https://doi.org/ 10.3390/nano12030317](https://doi.org/10.3390/nano12030317)

Publication II

Implementing Binder Gradients in Thick Water-Based NMC811 Cathodes via Multi-Layer Coating.

Lukas Neidhart, Katja Fröhlich, Franz Winter, and Marcus Jahn.

Batteries, 9(3):171, 2023; DOI: <https://doi.org/10.3390/batteries9030171>

Publication III

Layer by Layer: Improved Tortuosity in High Loading Aqueous NMC811 Electrodes.

Lukas Neidhart, Katja Fröhlich, Buket Boz, Franz Winter, and Marcus Jahn. *Journal of The Electrochemical Society*, 171(5):050532, 2024; DOI: <https://doi.org/10.1149/1945-7111/ad47d2>

Publication I

Article

Aqueous Manufacturing of Defect-Free Thick Multi-Layer NMC811 Electrodes

Lukas Neidhart ^{1,2,*} , Katja Fröhlich ¹, Nicolas Eshraghi ¹ , Damian Cupid ¹, Franz Winter ² 
and Marcus Jahn ^{1,*} 

¹ Electric Vehicle Technologies, Center for Low Emission Transport, Austrian Institute of Technology GmbH (AIT), Giefinggasse 2, 1210 Vienna, Austria; katja.froehlich@ait.ac.at (K.F.); nicolas.eshraghi@ait.ac.at (N.E.); damian.cupid@ait.ac.at (D.C.)

² Institute of Chemical, Environmental and Bioscience Engineering, TU Wien, Getreidemarkt 9, 1060 Vienna, Austria; franz.winter@tuwien.ac.at

* Correspondence: lukas.neidhart@ait.ac.at (L.N.); marcus.jahn@ait.ac.at (M.J.)

Abstract: Manufacturing thick electrodes for Li-ion batteries is a challenging task to fulfill, but leads to higher energy densities inside the cell. Water-based processing even adds an extra level of complexity to the procedure. The focus of this work is to implement a multi-layered coating in an industrially relevant process, to overcome issues in electrode integrity and to enable high electrochemical performance. $\text{LiNi}_{0.8}\text{Mn}_{0.1}\text{Co}_{0.1}\text{O}_2$ (NMC811) was used as the active material to fabricate single- and multi-layered cathodes with areal capacities of 8.6 mA h cm^{-2} . A detailed description of the manufacturing process is given to establish thick defect-free aqueous electrodes. Good inter-layer cohesion and adhesion to the current collector foil are achieved by multi-layering, as confirmed by optical analysis and peel testing. Furthermore, full cells were assembled and rate capability tests were performed. These tests show that by multi-layering, an increase in specific discharge capacity (e.g., 20.7% increase for C/10) can be established for all tested C-rates.

Keywords: multi-layer coating; aqueous electrode processing; NMC811; thick electrode



Citation: Neidhart, L.; Fröhlich, K.; Eshraghi, N.; Cupid, D.; Winter, F.; Jahn, M. Aqueous Manufacturing of Defect-Free Thick Multi-Layer NMC811 Electrodes. *Nanomaterials* **2022**, *12*, 317. <https://doi.org/10.3390/nano12030317>

Academic Editor: Likun Pan

Received: 10 December 2021

Accepted: 16 January 2022

Published: 19 January 2022

Publisher's Note: MDPI stays neutral with regard to jurisdictional claims in published maps and institutional affiliations.



Copyright: © 2022 by the authors. Licensee MDPI, Basel, Switzerland. This article is an open access article distributed under the terms and conditions of the Creative Commons Attribution (CC BY) license (<https://creativecommons.org/licenses/by/4.0/>).

1. Introduction

The demand for Lithium-ion batteries (LIBs) used in xEVs has grown steadily over the past years alongside the interest to increase driving range and lower prices. A decrease in manufacturing cost combined with more environmentally friendly cell production methods are key aspects in battery research, helping e-mobility to establish itself as a day-to-day form of transportation.

One way of tackling the issue of high production costs is to exchange the organic solvent, used in state-of-the-art electrode slurry formulations, with water [1–3]. Commercially available cathodes are produced with polyvinylidene fluoride (PVDF) as the binder material. Unfortunately, due to its low solubility, PVDF is commonly dissolved in the high-priced N-methylpyrrolidone (NMP) organic solvent. Furthermore, expensive measures must be implemented to properly trap and filter the highly toxic NMP, which evaporates during the drying process of the electrodes. Binder materials, which are essential components in slurries, must fulfill several requirements. First, they are essential to guarantee good adhesion between the particle components as well as to the current collector foil. Uniform coatings rely on well dispersed slurries, which in turn depend on properly chosen binders. Moreover, the harsh environment inside the battery cell also requires chemically inert materials. Aqueous slurry preparation is advantageous, as it eliminates the utilization of both PVDF and NMP, leading to an overall reduction of material and production costs. Additionally, evaporation of water is not only more efficient but also needs up to 90% less energy during the drying process [4].

Although there are several advantages associated with replacing NMP by water, there are also some disadvantages due to the reactions of the cathode active materials with water. For example, cathode active materials are prone to react with water, causing extra complexity to the whole procedure. Li^+ ions are leached from the lattice of the cathode active material, which is accompanied by the oxidation of the transition metal cations and loss of charge capacity. Furthermore, the leached Li^+ ions induce a raise in the pH of the slurry, due to the formation of LiOH . However, oxide layers on aluminum current collectors are only stable up to a pH lower than 8.6 [5] before the Al foil corrodes. The corrosion is not only associated with an increase in interface resistance, but also with the evolution of hydrogen gas, which can result in large cavities inside the electrode layer. To prevent the development of defects during and after the coating process, several strategies exist to regulate pH values during slurry mixing. The usage of different acids, such as phosphoric acid [6–8], hydrochloric acid [9,10], poly acrylic acid [11] or acetic acid [12] is the most common method for maintaining the pH of the slurry within an adequate range between 4 and 8.6. The utilization of certain acids has another positive effect on the Li^+ leaching mechanism. For example, adding phosphoric acid to the slurry can lead to the formation of an insoluble layer of phosphate compounds deposited on the surface of the active material particles, which suppress the ongoing leaching of transition metal cations from $\text{LiNi}_x\text{Mn}_y\text{Co}_z\text{O}_2$ (NMC) [13,14]. Zhu et al. showed that the viscosity of the slurry is also affected by the amount of acid added [12], as increasing the quantity of acetic acid leads to an increase in viscosity. Especially when targeting thick coatings, the viscosity has a significant influence on the film quality, which is influenced by the solid content of the slurry and binder characteristics. The solid loading of the slurry impacts the sedimentation rate of the coating and needs to be balanced carefully with solvent evaporation [15]. Binder concentration and molecular weight also affect the rheological behavior [15,16] and, consequently, the morphology of the electrode. In addition, a certain viscosity is necessary to maintain the desired thickness and shape of the electrode after the coating and drying process.

Increased energy densities can be realized by maximizing the ratio of active to inactive material [17–19]. Reducing separator and current collector materials leads not only to an increase in energy density, but also reduces the time required for cell assembly [19–21]. Energy density can further be increased by manufacturing thicker electrodes. However, thick electrodes tend to exhibit lower rate capabilities due to higher charge transfer resistance and blocked pore structures. The use of slurry additives and adjustment of coating parameters are widespread strategies to create crack free thick films. Controlling capillary pressures during the drying procedure by adding isopropyl alcohol to the slurry to regulate surface tensions [18] is one approach to reduce crack formation. Vapor grown graphite tubes as a replacement for carbon black can also help to minimize the amount of pinholes as recommended by Sahore et al. [22]. Beside maintaining mechanical integrity of the coating, a homogeneous distribution of the electrode material components are desirable, as accumulations of binder material can lead to unwanted side effects and diminished electrochemical performance. Binder migration is a large challenge during drying, thereby necessitating well optimized coating parameters. For example, the higher concentration of binder particles near the electrode-separator interface is a phenomenon that can be observed during the drying of thick coatings [23–27]. Light binder particles float on top of the layer due to a lack of liquid linkage between the surface and current collector. As a result, ion pathways are blocked and Li^+ transport is impeded. The absence of binder at lower regions is also problematic for adhesion between coating and current collector [28].

This manuscript presents an alternative strategy to circumvent these difficulties in thick layer manufacturing by multi-layer coating. Applying multiple layers of coating on top of each other can help control film properties in a desired manner. Graded porosity was already investigated and presented as an interesting opportunity in the past [29–33]. Reduction in resistance, a more uniform overpotential distribution, and an increase in diffusivity of Li-ions are affected by establishing low porosity regions near the substrate and

areas with high porosity in the vicinity of the separator [29–32]. However, implementing such a gradient is complicated as several subsequent calendaring steps are necessary, which reduces the expected positive effects [33]. Multi-layering also opens the doors to realize different material combinations inside the electrode. Blends of active materials can lead to higher ionic current densities [34], improvements against overcharging [35] and higher discharge rates [36]. For example, NMC442 cathodes [37] and graphite anodes that were fabricated [38] via dual layered slot-die coating show better electrochemical performance when the binder content of the top layer is reduced.

The purpose of this manuscript is to highlight the benefits of using multi-layering as a method to achieve high energy densities in cathode production. An industry oriented roll-to-roll (R2R) process was used to demonstrate the procedure using NMC811 as the cathode active material, which was coated in aqueous slurries. The resulting improvements in mechanical integrity and electrochemical performance are displayed. Due to its simplicity for industrial implementation, this technique is a stepping stone for the fabrication of unique electrode architectures. To the best of our knowledge, no defect free water-based NMC811 cathodes were established before with presented high areal capacity using the multi-layer approach.

2. Materials and Methods

Two different cathode coatings were performed—one thick single-layer (SL) of Ni-rich lithium nickel manganese cobalt oxide (NMC811) and one multi-layer (ML) coating with similar total electrode thickness. Each of the electrodes were analyzed with respect to their physical properties. In addition, coin cells were assembled to investigate their electrochemical performance.

2.1. Electrode Preparation

The cathode coatings consist of 92 wt% NMC811 powder (BASF SE, Ludwigshafen am Rhein, Germany; $d_{\text{avg}} = 7.8 \mu\text{m}$) as active material, 3 wt% carbon black (C-ENERGY™ SUPER C65, TIMCAL Ltd., Bodio, Switzerland; $d_{\text{avg}} = 37 \text{ nm}$) and 2 wt% artificial graphite (C-ENERGY™ KS6L, TIMCAL Ltd.; $d_{50} = 3.5 \mu\text{m}$) as conducting agents, 2 wt% of CMC (WALOCCEL™ CRT 2000 PA, DuPont de Nemours Inc., Wilmington, DE, USA) and 1 wt% of poly(meth)acrylate (PMA) (JSR SX8684(A)-64, JSR Micro NV, Leuven, Belgium) as binder. A total of 0.16 g of 1M phosphoric acid (H_3PO_4) per g of NMC811 was added prior to addition of NMC to control the pH-value throughout the mixing process. All solid components used in this study were dried over night at 105 °C.

Slurry mixing was done in a 250 mL container using a dissolver (DISPERMAT CV3-PLUS, VMA GETZMANN GMBH, Reichsdorf, Germany). Under constant stirring at 200 rpm, carbon black (CB) and artificial graphite (KS6L) were added to a 2 wt% CMC solution, following 10 min of stirring at 2000 rpm. H_3PO_4 was added, followed by another 2 min of stirring. NMC811 was added at 3000 rpm for 8 min. Finally, PMA was added at maximum 500 rpm stirring for 2 min to keep material integrity, terminating in a solid content of 60%. The pH was measured (SevenCompact S210, Mettler Toledo, Columbus, OH, USA) to monitor that values are below 8.6 before coating.

Electrode casting was performed continuously on a R2R coating machine (SC 30, COATEMA Coating Machinery GmbH, Dormagen, Germany) on 22 μm aluminum foil (Norsk Hydro ASA, Oslo, Norway). Three consecutively arranged drying chambers were set to temperatures of 45, 55 and 50 °C. The flow rates at the air inlet and outlet valves were set to 70 $\text{m}^3 \text{ h}^{-1}$ and 98 $\text{m}^3 \text{ h}^{-1}$, respectively. The coating speed was fixed at 0.3 m min^{-1} . The gap size of the coating knife was set to 550 μm for the thick single-layer, whereas for the multi-layer coatings, the wet thickness of the bottom layer was set to 250 μm and of the top layer was set to 330 μm . The bottom layer was fully dried before adding the second coating. To remove residual water, all samples were dried at 80 °C under vacuum for 12 h. Afterwards, the porosity ϵ of the electrodes was calculated by using Equations (1)–(3),

where ρ_c , m_c and V_c are the density, mass, and volume of the coating, respectively and ρ_{ph} is the sum of all bulk densities ρ_i with respect to their share p_i of the coating:

$$\rho_c = \frac{m_c}{V_c}, \quad (1)$$

$$\rho_{ph} = \sum_i p_i \rho_i, \quad (2)$$

$$\epsilon = 1 - \frac{\rho_c}{\rho_{ph}}. \quad (3)$$

Dried electrode sheets were calendared at 55 °C roll temperature (GK 300L, SAUER-ESSIG Group, Vreden, Germany) to a target porosity of 40% and a final thickness of approximately 205 μm including the current collector foil.

In the full cell investigations, anodes fabricated at the pilot line facilities were used as standard counter electrodes. All anodes used in this study were made of 90 wt% high energy density graphite (HED graphite 918-A2, Targray Technology International Inc, Kirkland, QC, Canada.; $d_{50} = 14.93 \mu\text{m}$), 4 wt% carbon black (C-ENERGY™ SUPER C65, TIMCAL Ltd.) and 6 wt% PVDF (Solef® PVDF, Solvay SA, Brussels, Belgium). The slurry was prepared in a planetary mixer (HIVIS DISPER MIX Model 3D-2, PRIMIX Corporation, Awaji-shi, Japan). First the active material and the carbon black were mixed together. PVDF, which was dissolved in an 8 wt% solution of NMP, was added and the slurry was mixed with increasing rotational speed. Additional NMP was added to dilute to a final solid content of 50%. The anode was coated on 11 μm copper foil (Carl Schlenk AG, Roth, Germany) with a wet thickness of 560 μm and afterwards dried and calendared to a porosity of 38%. A practical specific capacity for the graphite active material was assumed to be 350 mA h g^{-1} . An areal capacity of 9.5 mA h cm^{-2} for graphite anodes leads to a N/P ratio of 1.1.

Coating parameters and electrode materials are changed as little as necessary compared to a standardized manufacturing process to demonstrate the feasibility of the water based multi-layering technique to an existing production procedure.

2.2. Cell Assembly and Electrochemical Analysis

For coin cell tests, cathodes and anodes were cut into discs of 1.5 cm and 1.6 cm diameter, respectively. The anodes were dried at 120 °C and the cathodes at 80 °C under vacuum for 12 h before being transferred in vacuum into an Ar-filled glove box ($\text{O}_2 < 0.1 \text{ ppm}$, $\text{H}_2\text{O} < 0.1 \text{ ppm}$) (LabMaster Glove Box MB200-G, MBRAUN, Garching, Germany). Then, 2032 coin cells (CR2032) were assembled with 1.1 mm springs, 1.5 mm spacers and a Celgard 2500 separator. In total 150 μL of the electrolyte were added before crimping (MSK-110 Hydraulic Crimping Machine, MTI Corporation, Richmond, CA, USA) at 60 bar pressure.

After a resting time of 4 h, cycling tests were performed on an Arbin BT-21084, assuming 200 mA h g^{-1} capacity for the cathode active material. Two cycles with a C-rate of C/20 were carried out for formation, followed by five preconditioning cycles at C/10. The discharge capacity for further tests was adjusted to be in-line with the capacity of the third C/10 cycle. Thus, further tests were carried out with a specific capacity of 146 mA h g^{-1} and 177 mA h g^{-1} for SL and ML electrodes, respectively. Constant current constant voltage (CCCV) rate capability tests with symmetric charge/discharge rates of C/5, C/2, 1C and C/10 were also conducted in a voltage window of 3 to 4.2 V. To determine the long term cycling behavior, 50 cycles at a C-rate of C/5 were performed for both cell types.

Electrochemical impedance spectroscopy (EIS) was used to investigate the influence of multi-layering on the kinetics during cycling within the cell. Measurements were performed at 4.2 V/100% state of charge (SOC) during the two formation cycles at a C-rate of C/20. Potentiostatic electrochemical impedance was measured between 20 kHz and 100 mHz with a voltage amplitude of 10 mV on a Biologic MPG-2 instrument. Cyclic voltammetry (CV) measurements were performed to compare reduction and oxidation processes for

SL and ML electrodes in half cell configurations. The applied range of potential was set between 2.8 V and 4.5 V with a scan rate of 0.05 mV s^{-1} on an Arbin BT-21084.

2.3. Slurry and Electrode Properties

Surface topologies and cross-sectional imaging of the electrode samples were carried out via a digital microscope (VHX7000, Keyence Corporation, Osaka, Japan), to evaluate coating homogeneity and investigate inter-layer transitions of the multi-layered electrodes. The electrode samples were also investigated via scanning electron microscopy (SEM) at an electron acceleration voltage of 5 kV (SUPRA 40, Carl Zeiss AG, Oberkochen, Germany). Furthermore, the adhesive strength of the coating to the current collector foil was characterized using a 180° peel test (EKM-5KN, Jinan Marxtest Technology Co., Ltd., Jinan, China).

Viscosity measurements were performed under ambient conditions (DV-II+Pro Viscometer, AMETEK Brookfield, Middleboro, MA, USA), and dynamic viscosity was recorded with respect to increasing shear rates between 0 and 14 s^{-1} .

3. Results and Discussion

3.1. Characterization of Slurries and Electrodes

Since the pH of the slurry has a huge impact on the process, the pH evolution was carefully monitored to stay below the recommended coating limit of 8.6 [5] to suppress possible corrosion of the Al substrate. This is also important with regard to the emergence of agglomerations within the slurry reported to occur when the pH of 10 is exceeded in the slurry mixing process as described above in Section 2.1. Viscosity measurements showed a shear thinning behavior of 18 Pa s at zero shear rate and 4 Pa s at the shear rate applied during the coating process. Porosity and areal capacity were calculated based on the measured thicknesses and mass loadings in SL and ML electrodes. The values of the measured parameters are given in Table 1. Coating thicknesses are slightly higher than $200 \mu\text{m}$ for both types of electrodes. The as-coated porosity values of the SL and ML samples are calculated to be almost identical with each other, attaining values of 52.7 and 52.6% for the SL and ML electrodes, respectively. Both coatings show the same areal capacity of 8.6 mA h cm^{-2} , which was calculated assuming a 200 mA h g^{-1} specific capacity for the NMC811 active material. The lower layer constitutes a 43% share of the overall bi-layer electrode thickness. On average, a porosity of 59.3% was calculated for the base layer with an areal capacity of 3.1 mA h cm^{-2} .

Table 1. Coating parameters after coating and drying.

Electrode Type	Total Thickness [μm]	Porosity [%]	Areal Capacity [mA h/cm^2]
Single-layer	202 ± 2	52.7 ± 0.3	8.6 ± 0.1
Multi-layer	208 ± 4	52.6 ± 0.2	8.6 ± 0.2
Bottom layer	89 ± 5	59.3 ± 0.9	3.1 ± 0.0

Investigating the surface of each coating, it is evident that a continuous film without defects of any kind was fabricated (Figure 1a,c). Even before calendaring, a smooth homogeneous surface was present in both samples. This is a huge improvement considering the high thickness and aqueous processing of the electrode [18,22].

Analysis of cross sectional images taken via digital microscope are shown in Figure 1b,d for single- and multi-layer electrodes, respectively. Both samples are determined to have a thickness of $190 \mu\text{m}$ after calendaring to 40% porosity, verifying the measurements via a thickness gauge. Slightly inhomogeneous distribution of lighter gray particles is noticeable for SL samples, but overall no severe irregularities, such as entrapped air, cracks, or delamination from the substrate are recognizable. No distinct transition line between top and bottom layer is visible for the multi-layer sample, which is evidence of a good mechanical connection of both layers. SEM images of the multi-layer sample are displayed

in Figure 2. Merging of the layers is visible in agreement with the analysis via digital microscope. Images of higher magnification reflect an intertwining behavior of the secondary NMC811 particles of the top and bottom layers, which is necessary for strong cohesion. The indistinguishability of the two layers can also be accredited to the slight “dissolution” of the surface of the bottom layer into the freshly applied electrode slurry of the upper layer during coating. Furthermore, the surface film of the prime coating absorbs the slurry of the second coating forming a diffuse transition layer. This is a key aspect in guaranteeing good mechanical linkage of both layers.

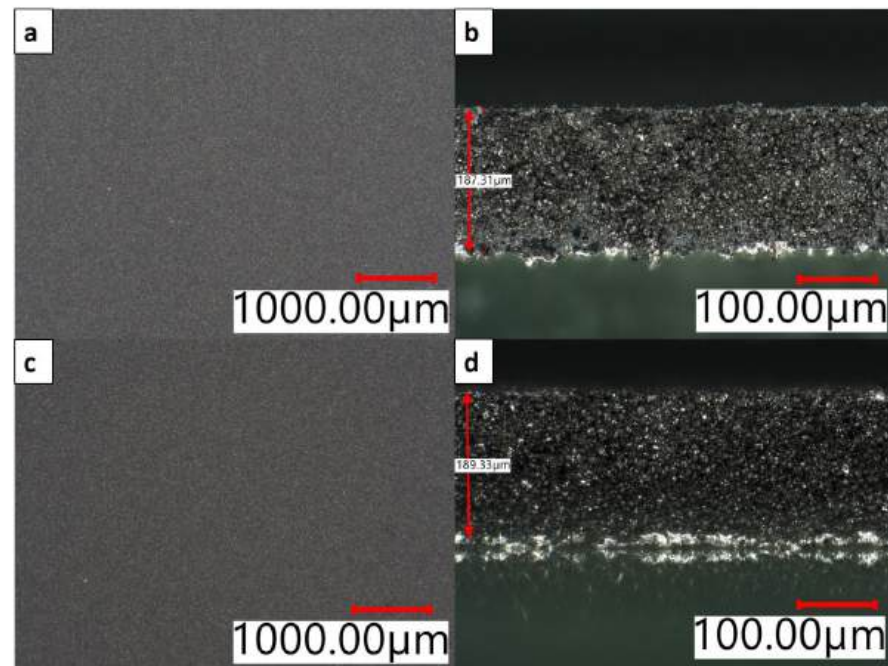


Figure 1. Digital microscope images of (a) SL top-view, (b) SL cross-section, (c) ML top-view, (d) ML cross-section after drying in air.

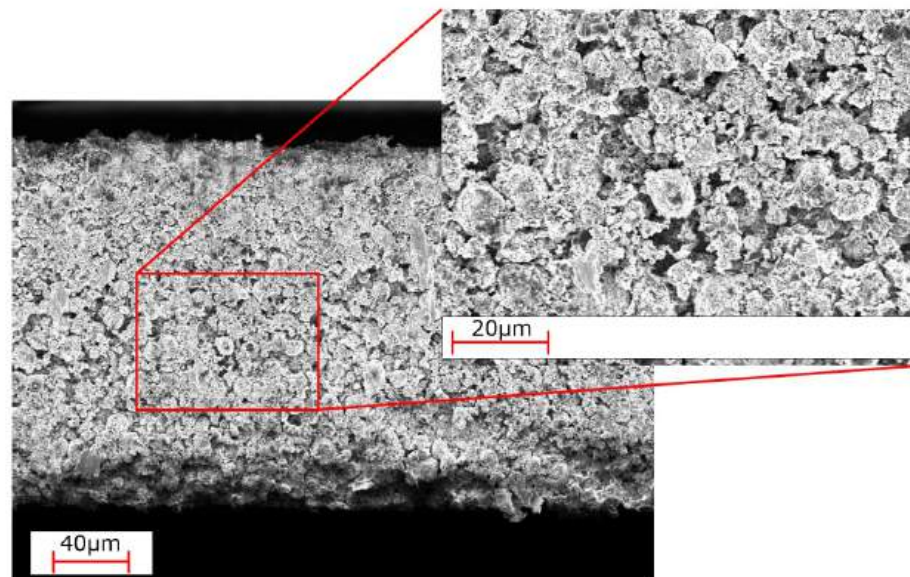


Figure 2. SEM image of the transition area from top to bottom layer of a multi-layer coated sample.

The significantly higher porosity of the lower layer also implies either a change in porosity of the layer itself due to the coating of the upper layer, or a porosity gradient with remarkably higher porosity in the vicinity of the current collector. Assuming no porosity

transition of the base after the second coating, the porosity of the top layer should be 47.5%. According to both Qi et al. [30] and Fang et al. [31] this lower porosity of the top layer would lead to a decreased cell performance as they suggest an electrode design with an opposite porosity gradient (higher porosity at the top of the electrode with decreasing porosity in the direction of the current collector) to reduce electrode resistance and enhance performance at high C-rates by increasing Li-ion diffusivity. However, the higher observed porosity of the upper layer, as well as the observed bubbles which develop after the second coating is applied, imply that cavities inside the base layer are filled with applied slurry. Figure 3 illustrates this mechanism. First, the slurry of the second coating comes in contact with the low porosity base layer (Figure 3a). As the water evaporates, porosity decreases in the top layer (Figure 3b) and the particles from the top layer migrate, and occupy the cavities in the bottom layer. This causes a mixing of both coatings (Figure 3c) and results in an increase in porosity of the initial layer (Figure 3d). This influences the porosity gradient to generate lower porosity values near the substrate foil and higher porosity values closer to the coating surface.

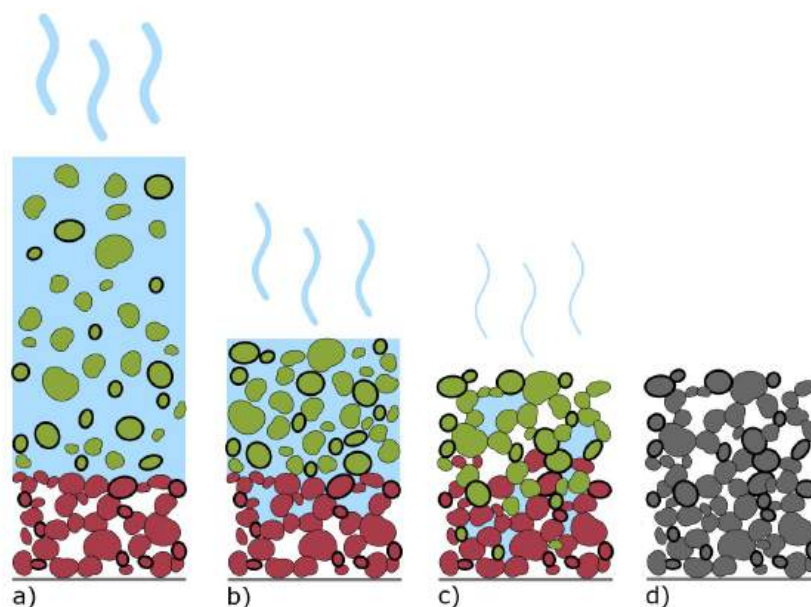


Figure 3. Visualization of the trickling behaviour after the second coating is applied. Particles in red and green, of the first and second layer, respectively. (a) situation right after coating the second layer, (b) sedimentation of particles during water evaporation, (c) mixing of second and first layer particles creating a diffuse interface, (d) coating after full solvent evaporation with higher porosity close to the current collector.

The results of the peel testing measurements confirm significant improvement following the multi-layer approach. In comparison to SL samples with $\sim 45 \text{ Nm}^{-1}$, ML coatings show values of $\sim 66 \text{ Nm}^{-1}$ (Figure 4). Therefore, on account of the second coating, an increase of approximately 45% in adhesion can be achieved. The reason for this vast enhancement is due to more homogeneously distributed binder particles, which is enhanced by the multi-layer processing.

3.2. Electrochemical Performance of Cells

Rate capability tests were performed to assess the electrochemical performance of both cell configurations. Results of statistically significant cells are displayed for clear visualization (Figure 5a). Formation cycles are not presented in the graph. It is worth mentioning, that after preconditioning at C/10 for 5 cycles, the C-rate was adjusted according to the measured cell discharge capacity of cycle number 3 (these preconditioning cycles are labels as C/10* in Figure 5a). Therefore, all cathodes are exposed to the same C-rate independent

of the actual specific capacity of the cathode after the preconditioning cycles. In accordance, the ML cells show higher specific discharge capacities throughout all the tests, even though the same C-rates are applied. Especially for low current densities, cells with ML cathodes outperform the SL samples by over 20%, which is a remarkable enhancement considering that both electrodes are fabricated using the same materials. Therefore, changing the coating procedure has a positive impact on material distribution inside the coating. The beneficial effect of multi-layering is even more pronounced for lower C-rates. For thick electrodes, limiting effects on Li^+ diffusion are evident at high current densities, and resulting losses in discharge capacity can not be compensated fully by multi-layering. Therefore the difference in capacity is slightly less distinct for 1C. Approximate improvements of the discharge capacities are listed in Table 2. When returning back to C/10, both cell configurations show initial high capacities, implying that cycling at high rates is not detrimental to their stability. Long term cycling tests show no significant decrease in specific discharge capacity after 50 cycles at C/5 for SL and ML electrodes (Figure 5b). Moreover, the coulombic efficiency for both SL and ML electrodes is determined to be close to 100%.

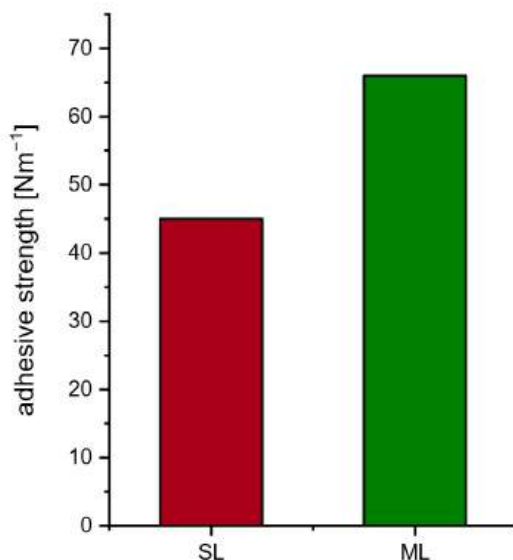


Figure 4. Comparison of the adhesive strength for SL and ML electrodes.

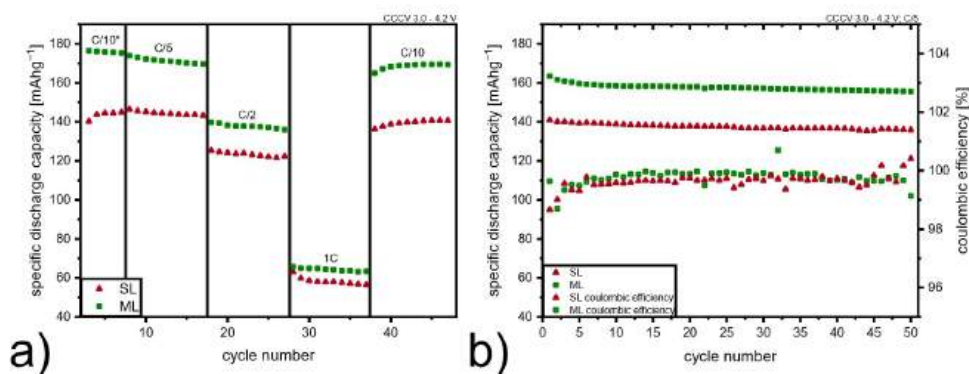


Figure 5. (a) Rate capability tests for single-layer (SL, red) and multi-layer (ML, green) electrodes with C-rates of C/10, C/5, C/2 and 1C. Cycles for preconditioning are labeled with C/10*. (b) Long term cycling at C/5 and coulombic efficiency of both electrode types.

Table 2. Increase of discharge capacities by multi-layering, compared to single-layer cathodes.

	C/10*	C/5	C/2	1C	C/10
Improvement [%]	23.3	18.6	11.7	10.3	20.7

Specific capacities of representative charge and discharge cycles are selected for comparison at each C-rate and are plotted in Figure 6 against applied voltages. The specific discharge capacity data as a function of C-rate are also given in Table 3. SL cells show values of 146 mA h g^{-1} , 128 mA h g^{-1} and 59 mA h g^{-1} for C/5, C/2, and 1C, respectively. ML cells have the overall highest specific discharge capacity of 171 mA h g^{-1} at C/5, whereas at C/2 and 1C, capacities of 136 mA h g^{-1} and 65 mA h g^{-1} are measured. Substantial differences in discharge capacity between the two types of electrodes are present for low current densities. For single layers only the region close to the electrode/separator interface is electrochemically active, since Li ion diffusion lengths are not sufficient enough to reach underlying areas [39]. However, in ML electrodes, areas located closer to the current collector foil also contribute to specific discharge capacity. Figure 6 shows the voltage-capacity curves of the SL and ML electrodes at C-rates of C/5 (a), C/2 (b) and 1C (c). All of them show a sloping profile, which is characteristic for NMC cathode active materials. In all cases, the charge and discharge capacities of the cells with the ML electrodes are larger than those for the SL electrodes, despite the fact that all electrodes have the same mass of active material. At high current densities, the benefits of multi-layering on Li-ion diffusion compensate for the drawbacks accompanied by electrode thickness itself [40]. Li-ion mobility definitely poses the most difficulties for thick electrodes to compete at high C-rates.

The potentiostatic contribution to the specific charge capacity is represented by the plateau at 4.2 V in Figure 6. Its length is directly proportional to the resistance inside the electrode during charge at constant voltage. The presence of multiple layers causes additional interfacial resistances within ML coated electrodes. Especially at C/5 (Figure 6a), a distinct difference in potentiostatic specific charge capacity is noticeable. At low C-rate in particular, a great part of the capacity is reached due to a elongated constant voltage step during charge. Nevertheless, it is worth mentioning that at C/5 higher specific charge capacities are already reached before the constant voltage step takes place.

The cyclic voltammograms shown in Figure 7 were recorded to compare the reduction and oxidation reactions of SL and ML electrodes during cycling. Both electrode types show no peak at 3 V, indicating the absence of Mn^{3+} [41]. Two pairs of oxidation/reduction peaks were observed for each sample. The small reduction peaks for SL and ML at around 3.9 V are not visible in the CV during oxidation due to overlapping with the lower voltage reduction peaks. Table 4 displays the potentials of oxidation/reduction peaks and corresponding polarizations for each electrode type. SL cells show oxidation peaks at $V_{\text{ox1}} = 3.90 \text{ V}$ and $V_{\text{ox2}} = 4.27 \text{ V}$ and reduction peaks at $V_{\text{red1}} = 3.63 \text{ V}$ and $V_{\text{red2}} = 4.09 \text{ V}$, with a polarization of $\Delta V_1 = 0.27 \text{ V}$ and $\Delta V_1 = 0.18 \text{ V}$ respectively. The polarizations for ML cells are $\Delta V_1 = 0.24 \text{ V}$ for peaks at $V_{\text{ox1}} = 3.86 \text{ V}$ and $V_{\text{red1}} = 3.62 \text{ V}$ and $\Delta V_1 = 0.16 \text{ V}$ for $V_{\text{ox2}} = 4.25 \text{ V}$ and $V_{\text{red2}} = 4.09 \text{ V}$. Comparing both electrode types, no significant differences in peak position and polarization are noticeable. However, ML samples show a larger area underneath the curve, which is in direct proportion to the capacity of the cell and is in accordance with the capacity difference shown in the rate capability test mentioned above. Besides the higher capacities, no obvious difference of the reaction kinetics were observed via CV measurements.

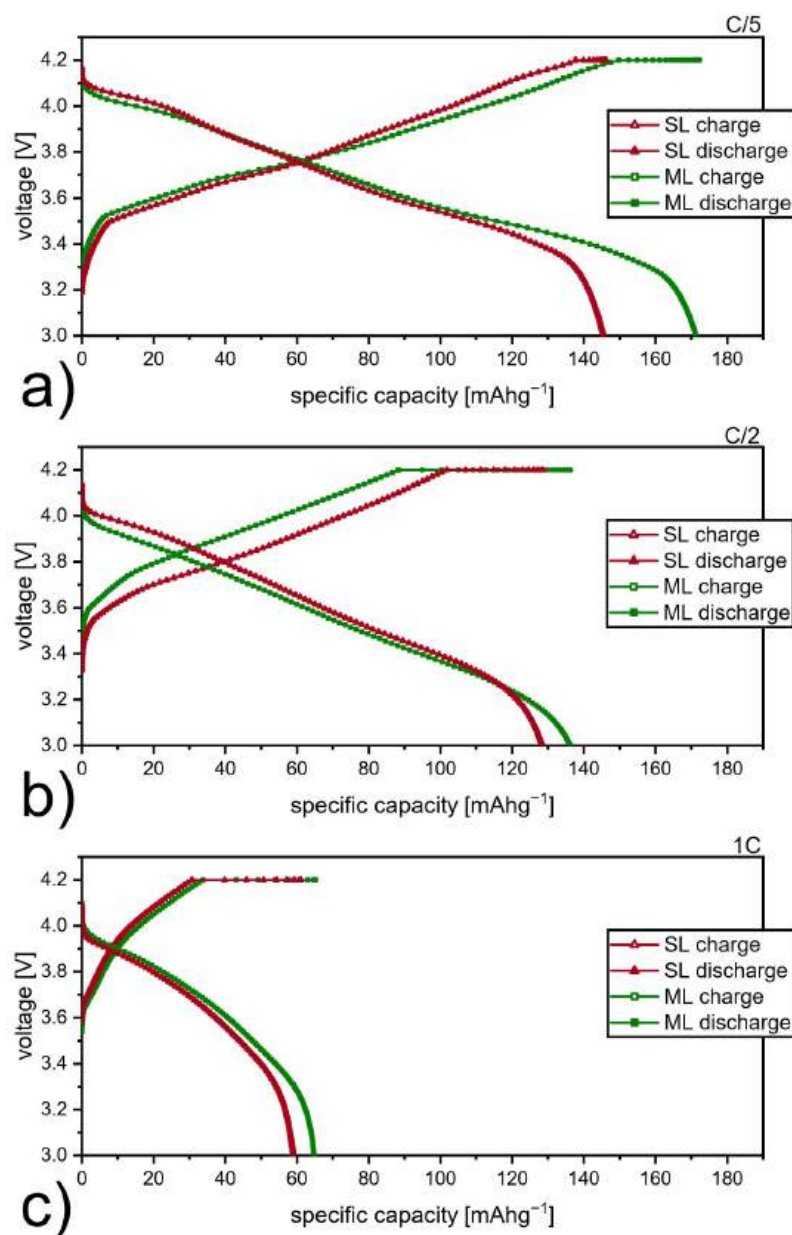


Figure 6. Voltage profiles of single-layer (SL, red) and multi-layer (ML, green) electrodes at (a) C/5, (b) C/2, and (c) 1C.

Table 3. Comparison of specific discharge capacities for different C-rates for SL and ML cells.

C-Rate	Electrode Type	Specific Discharge Capacity [mA h g ⁻¹]
C/5	SL	146
	ML	171
C/2	SL	128
	ML	136
1C	SL	59
	ML	65

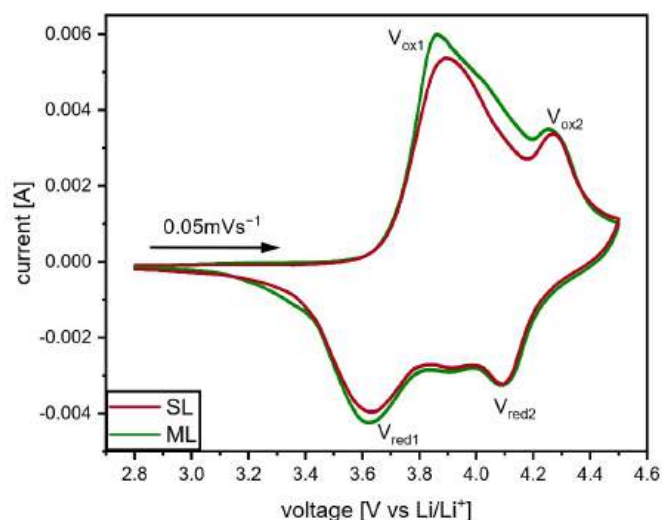


Figure 7. Cyclic voltammograms of single-layer (SL, red) and multi-layer (ML, green) electrodes between 2.8 and 4.5 V, with a scan rate of 0.05 mV s^{-1} .

Table 4. Comparison of anodic and cathodic peak positions and corresponding polarization from CV measurements for SL and ML half cells.

Electrode Type	V_{ox1} [v]	V_{red1} [v]	ΔV_1 [v]	V_{ox2} [v]	V_{red2} [v]	ΔV_2 [v]
SL	3.90	3.63	0.27	4.27	4.09	0.18
ML	3.86	3.62	0.24	4.25	4.09	0.16

EIS measurements were performed to help describe the transfer phenomena inside the cells during the formation cycles. The equivalent circuit used for the fitting is displayed in Figure 8. R_e corresponds to the bulk resistance resulting from the cell components (current collector, separator) and the electrolyte. The resistance contribution from the solid electrolyte interphase (SEI) formed on the graphite anode is fitted using R_{SEI} and a constant phase element Q_{SEI} , expressing its behavior as the non ideal capacitor. The charge transfer resistance R_{ct} and the double-layer capacitance represented by Q_{dl} show the contribution of charge transfer behaviour between the electrolyte and the electrode. The diffusion at low frequencies is represented by the Warburg element (W).

Figure 8 shows Nyquist plots of SL and ML cells during the first and second cycle at 4.2 V. The intercept of $\text{Re}(Z)$ at the high frequency region shows similar values in R_e for both samples, as shown in Table 5 and Figure 9a. This is expected, since all components apart from the cathodes are identical for each cell. The high to medium frequency semicircle shows the contribution of SEI formed during the first cycle on the anode side. At different stages of charge and discharge for the SL and ML electrodes the fitted data is comparable, highlighting the fact that the developed cathode in this work has no negative impact on the development of the SEI and its stability.

The mid to low frequency semicircle illustrates the charge transfer process, where a significant difference was observed between the charge transfer resistance of SL and ML electrodes. The higher specific discharge capacity, as shown in Figure 6, for the multi-layer cells, is attributed to the lower R_{ct} value. Heubner et al. [42] investigated the influence of electrode porosity and thickness on cell performance, with respect to limiting processes. They conclude that among other effects, decreased porosity leads to an increase in charge transfer resistance. Available areas for charge transfer reactions are reduced due to an increase in contacts between particles and particles with current collector foil and a reduction in the total contact area with the particles and the electrolyte [42]. The pore

size distribution in the ML electrode facilitates access of Li-ions from the electrolyte in the whole multi-layer electrode and thus lowering the R_{ct} . Figure 9 displays the acquired data for both electrode types and shows that a lower R_{ct} is achieved and a stable performance is established throughout cycling. The short inclined line at low frequencies represents the Li diffusion into the active material. Similar values for SL and ML samples lead to the conclusion that multi-layering does not negatively influence the diffusion of the Li-ions in the electrode and the mass transport controlled region of the cathode.

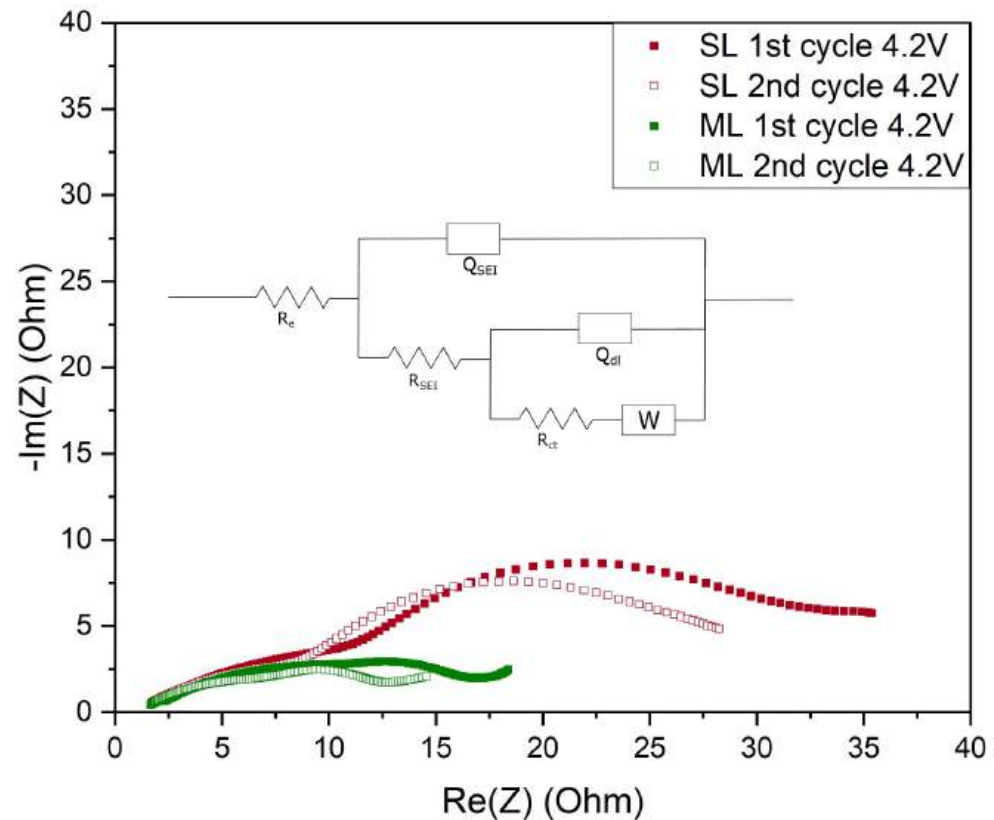


Figure 8. Equivalent circuit used to fit the measured impedance spectra and Nyquist plots of 1st and 2nd cycle at 4.2 V for single and multi-layer cathodes.

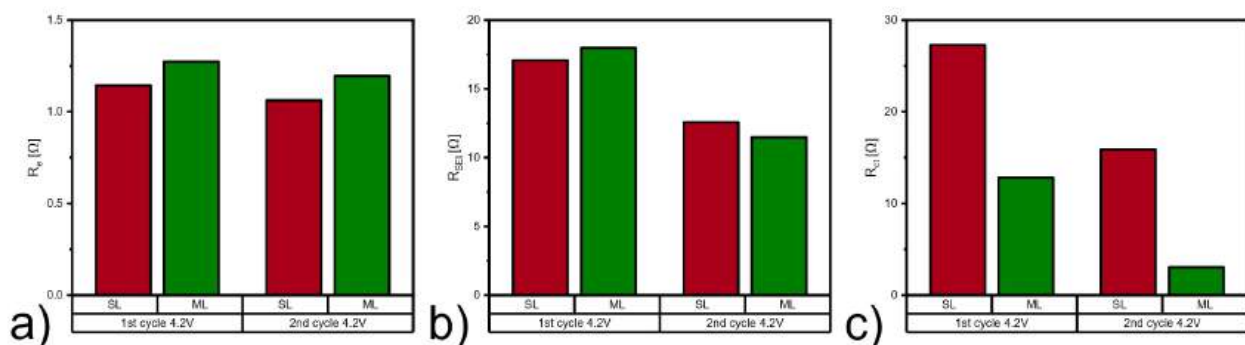


Figure 9. Comparison of resistance contributions (a) R_e , (b) R_{SEI} , and (c) R_{ct} for SL and ML cells during the 1st and 2nd cycle at 4.2 V.

The advantage of better adhesion in ML samples is not expected to be fully realized in coin cell configurations, since the high pressure inside the cells suppresses the delamination. Therefore, we anticipate a more pronounced benefit in pouch-cell configurations. Considering all electrochemical results, more homogeneous binder distribution and the resulting increase in charge transfer leads to higher discharge capacities in ML cells. In

addition, better electrochemical performance roots from a porosity gradient generated inside the cathode – as suggested in literature [30,31].

Table 5. Impedance parameters derived from the fitting of equivalent circuit models for SL and ML electrodes.

	Electrode Type	R_e [Ω]	R_{SEI} [Ω]	R_{ct} [Ω]	Q_{SEI} [mF]	α_{SEI}	Q_{dl} [mF]	α_{dl}	χ^2
1st cycle 4.2 V	SL	1.14	17.08	27.29	4.90	0.45	2.85	1	0.006
	ML	1.27	17.97	12.81	5.91	0.45	7.36	0.99	0.009
2nd cycle 4.2 V	SL	1.06	12.58	15.88	6.50	0.45	4.23	0.98	0.004
	ML	1.19	11.48	3.05	6.48	0.45	7.90	1	0.005

4. Conclusions

Aqueous fabrication of thick NMC811 electrodes was performed using an industrially relevant coating procedure. pH regulation with phosphoric acid and optimized coating parameters lead to smooth thick cathode films with superior areal capacities of 8.6 mA h cm^{-2} . It was demonstrated that multi-layer electrodes of equal active material loading can be fabricated in a subsequent tape casting procedure. The absence of morphological defects was confirmed for the presented manufacturing technique. Both electrodes exhibit sufficient mechanical integrity to be processed on a standard roll-to-roll system. Multi-layer casted cathodes show improved adhesion to the Al current collector, exemplified by a 45% higher adhesion strength for the ML electrodes compared to SL. In addition, optical inspection revealed a diffuse boundary between the separately coated layers, confirming good intra-layer adherence. ML electrodes show an improved electrochemical performance during rate capability tests compared to SL electrodes, expressed by higher specific discharge capacity for all investigated C-rates. It is worth mentioning that, especially for low current densities, improvements of over 20% are measured. This occurs due to more evenly distributed material inside the cathode coating and a possible gradient in coating porosity. All findings emphasize the potential of using multi-layering as a technique to gain energy density through increased electrode thickness. This technique can be easily adapted to R2R processing and a variety of electrode fabrication applications on an industrial scale. This study shows that by multi-layering, great improvements in electrochemical performance and mechanical stability can be achieved within aqueous fabrication of high energy density cathodes. It also opens up new possibilities for multiple design options by implementing various material components and properties into the electrode. The 3D architectures can be easily integrated within coatings in a consecutive large scale casting method. Future work will investigate cell performance for different material gradients, such as binder, conducting agents, and particle size in a two or more layer electrode design. Opportunities to decrease tortuosity and thereby shorten Li-ion pathways can be realized by varying film composition through multi-layer coating. This will be the subject of future investigations.

Author Contributions: Conceptualization, L.N.; methodology, L.N. and N.E.; validation, L.N.; formal analysis, L.N. and N.E.; investigation, L.N.; resources, K.F. and M.J.; writing—original draft preparation, L.N.; writing—review and editing, L.N., K.F., D.C., M.J. and F.W.; visualization, L.N.; supervision, K.F. and F.W.; project administration, K.F. and M.J.; funding acquisition, M.J. All authors have read and agreed to the published version of the manuscript.

Funding: This research was funded by the Austrian Federal Ministry for Climate Action, Environment, Energy, Mobility, Innovation, and Technology (BMK).

Institutional Review Board Statement: Not applicable.

Informed Consent Statement: Not applicable.

Data Availability Statement: The data presented in this study are available on request from the corresponding author.

Acknowledgments: The authors would like to thank Christiane Groher for performing the SEM measurements reported herein. In addition we would like to acknowledge the technical support from Andreas Gigl during electrode preparation.

Conflicts of Interest: The authors declare no conflict of interest.

Abbreviations

The following abbreviations are used in this manuscript:

CB	carbon black
CCCV	constant current constant voltage
CMC	carboxymethyl cellulose
CV	cyclic voltammetry
EIS	electrochemical impedance spectroscopy
ML	multi-layer
NMC	lithium nickel manganese cobalt oxide
NMP	N-Methyl-2-pyrrolidone
N/P ratio	negative/positive capacity ratio
PMA	poly(methyl)acrylate
PVDF	polyvinylidene fluoride
R2R	roll-to-roll
SEI	solid electrolyte interphase
SEM	scanning electron microscopy
SL	single-layer
SOC	state of charge

References

- Wood, D.L., III; Li, J.; Daniel, C. Prospects for reducing the processing cost of lithium ion batteries. *J. Power Sources* **2015**, *275*, 234–242. [[CrossRef](#)]
- Bryntesen, S.N.; Strømman, A.H.; Tolstorebrov, I.; Shearing, P.R.; Lamb, J.J.; Stokke Burheim, O. Opportunities for the State-of-the-Art Production of LIB Electrodes—A Review. *Energies* **2021**, *14*, 1406. [[CrossRef](#)]
- Li, J.; Du, Z.; Ruther, R.E.; An, S.J.; David, L.A.; Hays, K.; Wood, M.; Phillip, N.D.; Sheng, Y.; Mao, C.; et al. Toward low-cost, high-energy density, and high-power density lithium-ion batteries. *JOM* **2017**, *69*, 1484–1496. [[CrossRef](#)]
- Susarla, N.; Ahmed, S.; Dees, D.W. Modeling and analysis of solvent removal during Li-ion battery electrode drying. *J. Power Sources* **2018**, *378*, 660–670. [[CrossRef](#)]
- Chatalov, A.Y. Effet du pH sur le comportement électrochimique des métaux et leur résistance à la corrosion. *Dokl. Akad. Nauk SSSR* **1952**, *86*, 775.
- Kazzazi, A.; Bresser, D.; Birrozzi, A.; von Zamory, J.; Hekmatfar, M.; Passerini, S. Comparative analysis of aqueous binders for high-energy li-rich NMC as a Lithium-Ion cathode and the impact of adding phosphoric acid. *ACS Appl. Mater. Interfaces* **2018**, *10*, 17214–17222. [[CrossRef](#)] [[PubMed](#)]
- Kukay, A.; Sahore, R.; Parejiya, A.; Hawley, W.B.; Li, J.; Wood, D.L., III. Aqueous Ni-rich-cathode dispersions processed with phosphoric acid for lithium-ion batteries with ultra-thick electrodes. *J. Colloid Interface Sci.* **2021**, *581*, 635–643. [[CrossRef](#)] [[PubMed](#)]
- Carvalho, D.V.; Loeffler, N.; Kim, G.T.; Marinaro, M.; Wohlfahrt-Mehrens, M.; Passerini, S. Study of water-based lithium titanate electrode processing: The role of pH and binder molecular structure. *Polymers* **2016**, *8*, 276. [[CrossRef](#)]
- Hamam, I.; Zhang, N.; Liu, A.; Johnson, M.; Dahn, J. Study of the reactions between Ni-rich positive electrode materials and aqueous solutions and their relation to the failure of Li-ion cells. *J. Electrochem. Soc.* **2020**, *167*, 130521. [[CrossRef](#)]
- Li, C.C.; Lee, J.T.; Tung, Y.L.; Yang, C.R. Effects of pH on the dispersion and cell performance of LiCoO₂ cathodes based on the aqueous process. *J. Mater. Sci.* **2007**, *42*, 5773–5777. [[CrossRef](#)]
- Bauer, W.; Çetinel, F.A.; Müller, M.; Kaufmann, U. Effects of pH control by acid addition at the aqueous processing of cathodes for lithium ion batteries. *Electrochim. Acta* **2019**, *317*, 112–119. [[CrossRef](#)]
- Zhu, P.; Han, J.; Pfleging, W. Characterization and Laser Structuring of Aqueous Processed Li (Ni_{0.6}Mn_{0.2}Co_{0.2}) O₂ Thick-Film Cathodes for Lithium-Ion Batteries. *Nanomaterials* **2021**, *11*, 1840. [[CrossRef](#)] [[PubMed](#)]
- Loeffler, N.; Kim, G.T.; Mueller, F.; Diemant, T.; Kim, J.K.; Behm, R.J.; Passerini, S. In situ coating of Li [Ni_{0.33}Mn_{0.33}Co_{0.33}] O₂ particles to enable aqueous electrode processing. *ChemSusChem* **2016**, *9*, 1112–1117. [[CrossRef](#)]
- Kuenzel, M.; Bresser, D.; Diemant, T.; Carvalho, D.V.; Kim, G.T.; Behm, R.J.; Passerini, S. Complementary strategies toward the aqueous processing of high-voltage LiNi_{0.5}Mn_{1.5}O₄ lithium-ion cathodes. *ChemSusChem* **2018**, *11*, 562–573. [[CrossRef](#)]
- Ligneel, E.; Lestriez, B.; Hudhomme, A.; Guyomard, D. Effects of the solvent concentration (solid loading) on the processing and properties of the composite electrode. *J. Electrochem. Soc.* **2007**, *154*, A235. [[CrossRef](#)]

16. Lee, J.H.; Paik, U.; Hackley, V.A.; Choi, Y.M. Effect of carboxymethyl cellulose on aqueous processing of natural graphite negative electrodes and their electrochemical performance for lithium batteries. *J. Electrochem. Soc.* **2005**, *152*, A1763. [[CrossRef](#)]
17. Kuang, Y.; Chen, C.; Kirsch, D.; Hu, L. Thick electrode batteries: Principles, opportunities, and challenges. *Adv. Energy Mater.* **2019**, *9*, 1901457. [[CrossRef](#)]
18. Du, Z.; Rollag, K.; Li, J.; An, S.J.; Wood, M.; Sheng, Y.; Mukherjee, P.; Daniel, C.; Wood Iii, D. Enabling aqueous processing for crack-free thick electrodes. *J. Power Sources* **2017**, *354*, 200–206. [[CrossRef](#)]
19. Singh, M.; Kaiser, J.; Hahn, H. Thick Electrodes for High Energy Lithium Ion Batteries. *J. Electrochem. Soc.* **2015**, *162*, A1196–A1201. [[CrossRef](#)]
20. Golmon, S.; Maute, K.; Dunn, M.L. A design optimization methodology for Li⁺ batteries. *J. Power Sources* **2014**, *253*, 239–250. [[CrossRef](#)]
21. Lu, W.; Jansen, A.; Dees, D.; Nelson, P.; Veselka, N.R.; Henriksen, G. High-energy electrode investigation for plug-in hybrid electric vehicles. *J. Power Sources* **2011**, *196*, 1537–1540. [[CrossRef](#)]
22. Sahore, R.; Wood, D.L., III; Kukay, A.; Grady, K.M.; Li, J.; Belharouak, I. Towards understanding of cracking during drying of thick aqueous-processed LiNi_{0.8}Mn_{0.1}Co_{0.1}O₂ cathodes. *ACS Sustain. Chem. Eng.* **2020**, *8*, 3162–3169. [[CrossRef](#)]
23. Font, F.; Protas, B.; Richardson, G.; Foster, J.M. Binder migration during drying of lithium-ion battery electrodes: Modelling and comparison to experiment. *J. Power Sources* **2018**, *393*, 177–185. [[CrossRef](#)]
24. Müller, M.; Pfaffmann, L.; Jaiser, S.; Baunach, M.; Trouillet, V.; Scheiba, F.; Scharfer, P.; Schabel, W.; Bauer, W. Investigation of binder distribution in graphite anodes for lithium-ion batteries. *J. Power Sources* **2017**, *340*, 1–5. [[CrossRef](#)]
25. Kremer, L.S.; Hoffmann, A.; Danner, T.; Hein, S.; Prifling, B.; Westhoff, D.; Dreer, C.; Latz, A.; Schmidt, V.; Wohlfahrt-Mehrens, M. Manufacturing Process for Improved Ultra-Thick Cathodes in High-Energy Lithium-Ion Batteries. *Energy Technol.* **2020**, *8*, 1900167. [[CrossRef](#)]
26. Jaiser, S.; Müller, M.; Baunach, M.; Bauer, W.; Scharfer, P.; Schabel, W. Investigation of film solidification and binder migration during drying of Li-Ion battery anodes. *J. Power Sources* **2016**, *318*, 210–219. [[CrossRef](#)]
27. Westphal, B.G.; Kwade, A. Critical electrode properties and drying conditions causing component segregation in graphitic anodes for lithium-ion batteries. *J. Energy Storage* **2018**, *18*, 509–517. [[CrossRef](#)]
28. Baunach, M.; Jaiser, S.; Schmelzle, S.; Nirschl, H.; Scharfer, P.; Schabel, W. Delamination behavior of lithium-ion battery anodes: Influence of drying temperature during electrode processing. *Dry. Technol.* **2016**, *34*, 462–473. [[CrossRef](#)]
29. Liu, L.; Guan, P.; Liu, C. Experimental and simulation investigations of porosity graded cathodes in mitigating battery degradation of high voltage lithium-ion batteries. *J. Electrochem. Soc.* **2017**, *164*, A3163. [[CrossRef](#)]
30. Qi, Y.; Jang, T.; Ramadesigan, V.; Schwartz, D.T.; Subramanian, V.R. Is there a benefit in employing graded electrodes for lithium-ion batteries? *J. Electrochem. Soc.* **2017**, *164*, A3196. [[CrossRef](#)]
31. Fang, R.; Ge, H.; Wang, Z.; Li, Z.; Zhang, J. A two-dimensional heterogeneous model of lithium-ion battery and application on designing electrode with non-uniform porosity. *J. Electrochem. Soc.* **2020**, *167*, 130513. [[CrossRef](#)]
32. Müller, D.; Landa-Medrano, I.; Eguia-Barrio, A.; Boyano, I.; Urdampilleta, I.; de Meatza, I.; Fill, A.; Birke, P. Electrochemical characterization of bi-layered graphite anodes combining high and low porosity in lithium-ion cells to improve cell performance. *Electrochim. Acta* **2021**, *391*, 138966. [[CrossRef](#)]
33. Dai, Y.; Srinivasan, V. On graded electrode porosity as a design tool for improving the energy density of batteries. *J. Electrochem. Soc.* **2015**, *163*, A406. [[CrossRef](#)]
34. Kespe, M.; Cernak, S.; Gleiß, M.; Hammerich, S.; Nirschl, H. Three-dimensional simulation of transport processes within blended electrodes on the particle scale. *Int. J. Energy Res.* **2019**, *43*, 6762–6778. [[CrossRef](#)]
35. Imachi, N.; Takano, Y.; Fujimoto, H.; Kida, Y.; Fujitani, S. Layered cathode for improving safety of Li-ion batteries. *J. Electrochem. Soc.* **2007**, *154*, A412. [[CrossRef](#)]
36. Whitacre, J.; Zanghi, K.; West, W.; Ratnakumar, B. Dual active material composite cathode structures for Li-ion batteries. *J. Power Sources* **2008**, *177*, 528–536. [[CrossRef](#)]
37. Liu, D.; Chen, L.C.; Liu, T.J.; Chu, W.B.; Tiu, C. Improvement of lithium-ion battery performance by two-layered slot-die coating operation. *Energy Technol.* **2017**, *5*, 1235–1241. [[CrossRef](#)]
38. Diehm, R.; Kumberg, J.; Dörrer, C.; Müller, M.; Bauer, W.; Scharfer, P.; Schabel, W. In Situ Investigations of Simultaneous Two-Layer Slot Die Coating of Component-Graded Anodes for Improved High-Energy Li-Ion Batteries. *Energy Technol.* **2020**, *8*, 1901251. [[CrossRef](#)]
39. Zheng, H.; Li, J.; Song, X.; Liu, G.; Battaglia, V.S. A comprehensive understanding of electrode thickness effects on the electrochemical performances of Li-ion battery cathodes. *Electrochim. Acta* **2012**, *71*, 258–265. [[CrossRef](#)]
40. Gao, H.; Wu, Q.; Hu, Y.; Zheng, J.P.; Amine, K.; Chen, Z. Revealing the rate-limiting Li-ion diffusion pathway in ultrathick electrodes for Li-ion batteries. *J. Phys. Chem. Lett.* **2018**, *9*, 5100–5104. [[CrossRef](#)]
41. Fröhlich, K.; Abrahams, I.; Jahn, M. Determining phase transitions of layered oxides via electrochemical and crystallographic analysis. *Sci. Technol. Adv. Mater.* **2020**, *21*, 653–660. [[CrossRef](#)] [[PubMed](#)]
42. Heubner, C.; Nickol, A.; Seeba, J.; Reuber, S.; Junker, N.; Wolter, M.; Schneider, M.; Michaelis, A. Understanding thickness and porosity effects on the electrochemical performance of LiNi_{0.6}Co_{0.2}Mn_{0.2}O₂-based cathodes for high energy Li-ion batteries. *J. Power Sources* **2019**, *419*, 119–126. [[CrossRef](#)]

Publication II

Article

Implementing Binder Gradients in Thick Water-Based NMC811 Cathodes via Multi-Layer Coating

Lukas Neidhart ^{1,2*}, Katja Fröhlich ¹, Franz Winter ² and Marcus Jahn ¹

¹ Battery Technologies, Center for Low Emission Transport, Austrian Institute of Technology GmbH (AIT), 1210 Vienna, Austria; katja.froehlich@ait.ac.at (K.F.); marcus.jahn@ait.ac.at (M.J.)

² Institute of Chemical, Environmental and Bioscience Engineering, TU Wien, 1060 Vienna, Austria; franz.winter@tuwien.ac.at

* Correspondence: lukas.neidhart@ait.ac.at

Abstract: Multi-layer coating of electrodes with different material compositions helps unlock the full potential of high-loaded electrodes. Within this work, $\text{LiNi}_{0.8}\text{Mn}_{0.1}\text{Co}_{0.1}\text{O}_2$ (NMC811) cathodes with an areal capacity of $>8.5 \text{ mA h cm}^{-2}$ and tuned binder concentrations were fabricated by using an industrially relevant roll-to-roll process. Rate capability tests revealed an increase in practical specific discharge capacity independent from the C-rate for cathodes with reduced binder concentration in the top layer. At high current densities (C-rate of 1C) an improved performance of up to 27% was achieved. Additionally, at lower C-rates, binder gradients perpendicular to the current collector have beneficial effects on thick electrodes. However, surface analysis and electrochemical impedance spectroscopy revealed that without an adequate connection between the active material particles through a carbon-binder domain, charge transfer resistance limits cycling performance at high current densities.

Keywords: multi-layer coating; aqueous electrode processing; NMC811; thick electrode; binder gradient



Citation: Neidhart, L.; Fröhlich, K.; Winter, F.; Jahn, M. Implementing Binder Gradients in Thick Water-Based NMC811 Cathodes via Multi-Layer Coating. *Batteries* **2023**, *9*, 171. <https://doi.org/10.3390/batteries9030171>

Academic Editors: Yubin Niu and Marco Giorgetti

Received: 16 December 2022

Revised: 7 March 2023

Accepted: 14 March 2023

Published: 16 March 2023



Copyright: © 2023 by the authors. Licensee MDPI, Basel, Switzerland. This article is an open access article distributed under the terms and conditions of the Creative Commons Attribution (CC BY) license (<https://creativecommons.org/licenses/by/4.0/>).

1. Introduction

Maximizing energy densities in Li-ion batteries is a desirable goal in energy storage production that has emerged as a major challenge in the automotive sector. The increase in practical energy densities plays a central role for achieving low-price and long-range batteries for xEVs of the future. A possible solution to reaching that target is the fabrication of thick electrodes, thus keeping the ratio of active and inactive materials high within assembled cells [1,2]. However, the complexity of the manufacturing process increases with high loading electrodes and, thus, needs to be adapted. Coating parameters require thorough fine-tuning in order to suppress major defects within the coated layer. Uneven distribution of material components in the coating can affect its mechanical integrity, as well as electrochemical performance. Binder migration is a common problem, occurring during the drying process of thick electrodes, which can cause unfavorable results. A binder particle gradient with low concentrations next to the substrate foil can lead to delamination on the one hand, but also to an ion-blocking layer at the coating–separator interface. These phenomena have been documented by multiple research groups in the past [3–7]. Optimized drying parameters can suppress binder migration, which originates from inhomogeneous solvent evaporation. This is a consequence of loss of liquid pathways linking the upper and lower part of the coating [5]. However, especially for electrodes with high material loading, ensuring gentle drying conditions is not realistic for production throughput on an industrial scale. Multi-layer (ML) coating has proven itself as a possible technique to prevent unwanted coating defects. The improved material distribution within the coating not only has positive effects on the mechanical integrity of the electrode, but is also accompanied by higher specific discharge capacities and reduced cell impedance [8,9].

Applying the multi-layer technique to the coating process comes with additional room for customizing electrode production if one utilizes the opportunity to use different slurry formulations for each individual layer. These variations can be realized, e.g., in terms of varying particle sizes of the active material [10,11], active material blends [12], or porosity gradients [13–16]. Another possibility arising from multi-layering is tuning the material ratio in the slurry formulation. In particular for high-loading electrodes, regional material dependencies are more relevant—either for increased mechanical stability or higher ionic and electric conductivity [13,17].

Every material component of the electrode slurry has a specific purpose and their ratios and position in the mixing sequence have a large impact on the behavior of the resulting laminate after coating [18,19]. Firstly, one can distinguish between active and inactive materials—only the former contribute to the capacity of the electrode. Inactive materials can roughly be separated into those enhancing conductivity, and components which help by mechanically stabilizing both slurry and coating. Together they form a so-called carbon-binder domain (CBD) [20–22]. The interaction between carbon entities and binder particles and how they are embedded in the dry coating depends on their ratio and drying parameters. Carboxy methyl cellulose (CMC) is commonly used as a binder in aqueous electrode systems. It acts as a thickening agent in the slurry and stabilizes dispersion [23–25]. High viscosity is particularly important when depositing thick layers of coating. In general, the sole use of CMC as a binder is not recommended due to its brittleness after solvent evaporation. To enhance the flexibility of the coating, additional, mostly polymeric, binders are added to the slurry. A common combination in an aqueous system is with styrene butadiene rubber (SBR) [26,27], but acrylic-based binders can also be found in literature, such as polymethyl methacrylate (PMMA) [28,29], polymethyl acrylate (PMA) [8,30], or polyacrylic acid (PAA) [31]. Among inactive materials, there are components that help to increase the electrical conductivity of the electrode. Carbon black (CB) contributes essentially to the conductivity in the electrode matrix by connecting active material particles ensuring optimal capacity utilization in all depths of the coating. For thick electrodes, this is a critical feature to fully exploit higher capacities. Due to its high porosity, CB is often partially replaced by graphite additives to ensure high volumetric capacities for high loading electrodes [32]. The carbon binder domain is necessary to guarantee good adhesion of the coating to the substrate and to provide enough cohesion between the particles, whilst simultaneously sustaining sufficient electrical conductivity on a micro- and macroscopic level.

In addition to the demand for higher energy densities, sustainable processing is a key parameter in today's battery manufacturing. In particular for cathode fabrication, the usage of toxic solvents such as N-methyl-2-pyrrolidone (NMP) in combination with polyvinylidene fluoride (PVDF) binder is still the state of the art [19]. While for anodes, water-based systems are already commercialized, aqueous processing of cathode materials is still challenging [33]. Unfortunately, a rise in pH can occur during slurry mixing through Li^+ -ions leaching out of the active material and forming lithium hydroxide with water [34–37]. The protective oxide layer of the aluminum current collector can be dissolved when it is exposed to solutions with a pH lower than 4, or higher than 8.6, causing detrimental corrosion to the substrate [38]. Therefore, with rising alkalinity of the slurry caused by Li^+/H^+ exchange, the morphology and mechanical integrity of the electrode coating can be compromised. Various different acidic additives are used to counteract this detrimental effect [39–45]. Particle coating can also be chosen as another method to minimize the degradation of the active material particles and to prevent extensive Li-leaching [46].

In a previous study [8], we have shown the principle of the multi-layer technique and its general benefits when applied to high loading NMC811 cathodes. The promising results suggested that further optimization of the electrodes can be achieved with this method. In this work, we extend these initial findings via the implementation of a binder gradient to (1) further reduce the amount of inactive materials compared to state-of-the-art, and (2) increased inter-particle connection and correlated higher conductivity and

high current capability. Due to its high Ni content and thus high energy density, Ni-rich NMC811 cathode active material was processed in this work. The combination of PMA and CMC showed well-dispersed, agglomerate-free slurries in the past and, therefore, was chosen as binder combination. PMA has a high number of functional groups in the acrylic binder and, thus, can form hydrogen bonds with the graphite additive [30], increasing the connection between the active material and the conductive agents. The aim of this work is to show possible effects of tuning the binder content in water-based thick cathodes by making use of the multi-layer coating technique. Investigations of how ML electrodes benefit from consecutive reduction in the binder material in the top layer are described. The simplicity and flexibility of this unconventional electrode manufacturing technique and its usage in a roll-to-roll (R2R) coating process of industrial relevance are demonstrated in this work. To the authors' knowledge, this is the first work that covers aqueous multi-layered NMC811 cathodes with integrated binder gradients and comparatively high loadings (up to 45 mg cm^{-2} of active material), and high discharge capacities.

2. Materials and Methods

Three decreases in binder content were implemented in the slurry formulation in Ni-rich lithium nickel manganese cobalt oxide (NMC811) multi-layer coatings of comparable thickness. To evaluate possible effects of reduced binder content in the top layer, physical properties, as well as electrochemical performance were analyzed in coin cell configuration.

2.1. Electrode Preparation

All samples have the same coating as a basis, which consists of NCM811 powder (BASF SE, Ludwigshafenam Rhein, Germany; $d_{\text{avg}} = 7.8 \text{ }\mu\text{m}$) as active material, carbon black (C-ENERGYTMSUPER C65, TIMCAL Ltd., Bodio, Switzerland; $d_{\text{avg}} = 37 \text{ nm}$), artificial graphite (C-ENERGYTMKS6L, TIMCAL Ltd.; $d_{\text{avg}} = 3.5 \text{ }\mu\text{m}$), CMC (WALOCCELTMCRT 2000 PA, DuPont de Nemours Inc., Wilmington, DE, USA) and poly(methyl)acrylate (PMA)(ENEOS Cathode Binder, ENEOS Materials Belgium BV, Belgium) in a 92/3/2/1/2 wt% composition. Then, 0.16 g of 1M phosphoric acid (H_3PO_4) (Sigma Aldrich, Saint Louis, MO, USA) was used for each gram of NMC811 to counteract the increase in pH due to leaching of Li^+ ions from the active material. To remove residual water, solid components were dried for approximately 8 h at $105 \text{ }^\circ\text{C}$.

Slurries were mixed in a 250 mL container with a dissolver blade (DISPERMAT CV3-PLUS, VMA GETZMANN GMBH, Reichsdorf, Germany). Firstly, CB and KS6L were added to a 2 wt% CMC aqueous solution under constant stirring at slow speed, ending in 10 min of stirring at 2000 rpm. To lower the pH value, H_3PO_4 was added before incorporating the NMC811 powder into the slurry at 3000 rpm for 8 min. PMA was added at low speed (500 rpm) to ensure the integrity of the binder molecules. To prevent corrosion at the current collector, pH values of the slurry were measured using a pH-meter (SevenCompact S210, Mettler Toledo). Three electrode slurries were prepared to show the effect of reduced PMA concentration within multi-layer coated cathodes. The amount of PMA was reduced in comparison to the bottom layer, to 50%, 25%, and 0% of the initial amount of acrylate. In the remainder of this work, these samples will be abbreviated as 50PMA, 25PMA, and 0PMA. The resulting amounts of active materials and PMA binders used are listed in Table 1. The final solid content of the slurry was determined to be around 60%, slightly varying due to the the amount of PMA solution added to the mixture.

Table 1. Amount of active material and PMA in the slurry formulations of all samples.

	Top Layer		Total	
	AM [%]	PMA [%]	AM [%]	PMA [%]
0PMA	93.88	0.0	92.94	1.0
25PMA	93.40	0.5	92.70	1.25
50PMA	92.93	1.0	92.47	1.5

The roll-to-roll coating process was conducted via doctor blade coating method (SC 30, COATEMA Coating Machinery GmbH, Dormagen, Germany) with a gap size of 250 μm for the base layer. Gentle drying was ensured by the combination of three sequential drying phases at 45 $^{\circ}\text{C}$, 55 $^{\circ}\text{C}$, and 50 $^{\circ}\text{C}$ and a line speed of 0.3 m min^{-1} . After drying of the bottom layer, a second layer of slurry—with modified PMA content—was deposited with a wet thickness of 330 μm . 22 μm thick aluminum foil (Norsk Hydro ASA, Oslo, Norway) was used for all cathode coatings as current collector. The resulting layer thicknesses after drying for bottom and top layers are listed in Table 2. An additional 12 h drying step at 80 $^{\circ}\text{C}$ under vacuum was performed to remove residual solvent. The porosity of the as-coated multi-layer electrodes was calculated on the basis of the physical densities of the individual materials and the coating itself. The calculations were conducted in analogy to a previous study [8]. All electrode types were compacted at room temperature to a porosity of 40% with a hot roller press (MSK-HRP-1A, MTI Corporation, Richmond, CA, USA) and a final thickness of $\sim 200 \mu\text{m}$.

Table 2. Electrode parameters after coating, drying, and compacting.

Electrode Type	Total Coating Thickness [μm]	Porosity [%]	Areal Capacity [mA h cm^{-2}]
bottom layer	99 \pm 2	52.7 \pm 0.3	8.6 \pm 0.1
0PMA	200 \pm 4	52.8 \pm 0.2	8.52 \pm 0.2
25PMA	200 \pm 5	52.04 \pm 0.9	8.58 \pm 0.1
50PMA	198 \pm 5	52.6 \pm 0.9	8.51 \pm 0.15

Graphite anodes were fabricated as counter electrodes to enable investigations on a full cell level. The anode coatings consist of high energy density graphite (HED graphite 918-A2, Targray Technology International Inc, Kirkland, QC, Canada.; $d_{\text{avg}} = 14.93 \mu\text{m}$), carbon black (C-ENERGYTMSUPER C65, TIMCAL Ltd.), and polyvinylidene difluoride (PVDF) (Solef@PVDF, Solvay SA, Brussels, Belgium) in a 90/4/6 wt% composition. Preparation of the slurry was conducted in a planetary mixer (HIVIS DISPER MIX Model 3D-2, PRIMIX Corporation, Awaji-shi, Japan). After pre-mixing the active material and the carbon black, an 8 wt% solution of PVDF dissolved in NMP was added. To reach the targeted solid content of 50%, more NMP was added. The slurry was coated onto a 11 μm copper foil (Carl Schlenk AG, Roth, Germany) with a gap width of 560 μm to reach the desired areal capacity of 9.5 mA h cm^{-2} , assuming a specific capacity of 350 mA h g^{-1} for the active material. Anodes were dried and compacted to a porosity of 38% before cell assembly. Graphite electrodes were produced in accordance with a standard electrode manufacturing process in order to guarantee good comparability for all electrochemical tests.

2.2. Slurry and Electrode Characteristics

Scanning electron microscopy (SEM) was used to investigate surface topologies and material distribution at electron acceleration voltages of 5 kV and 3 kV for top-view and cross-section images, respectively (SUPRA 40, Carl Zeiss AG). Samples for cross-sections were sanded with silicon carbide sandpaper and polished with diamond paste after being

embedded in epoxy resin. Cross-section samples were sputtered with Au for 40 s to increase conductivity.

Chronoamperometrical tests were performed to determine the electrical resistance of the electrodes prior to the electrochemical tests. Resulting currents were measured at equidistant voltage steps in a range of 10 mV to 50 mV on a Biologic-VSP instrument. The slope of the obtained I–V curve represents the electrical conductance for each sample according to Ohm's law.

Raman spectra of the electrodes and the individual electrode components (NMC811, CB, KS6L, PMA (Figure A1)) were recorded with a Horiba XploRA Plus, utilizing a 50× objective, a grating of 1200 gr/mm, and a 532 nm laser operated at 10 mW. Elemental mapping in an arbitrarily selected 500 × 500 μm square was conducted at 100 points, with three acquisitions per point.

2.3. Cell Assembly and Electrochemical Analysis

Discs with a diameter of 1.5 cm and 1.6 cm were punched out of the cathodes and anodes, respectively, for further processing into coin cells. The electrodes were dried (anodes at 120 °C and cathodes at 80 °C) under vacuum for 12 h and transferred into a glove box ($O_2 < 0.1$ ppm, $H_2O < 0.1$ ppm (LabMaster Glove Box MB200-G, MBRAUN)) of Ar-filled atmosphere. Coin cells of 2032 dimension were assembled, containing 1.1 mm wave springs, 1.5 mm stainless steel spacers, and a trilayer 2500 Celgard separator. Then, 150 μL of LiPF₆ in 3:7 EC:EMC (2 wt% VC) were used as an electrolyte. To ensure full wetting of the electrodes, a resting period of 4 h was implemented before further electrochemical testing. An Arbin BT-21084 instrument was used for all cycling tests. Specific capacity of 200 mA h g⁻¹ was assumed for the cathode active material. All cells went through a formation and preconditioning protocol of 2 cycles at 0.05C, followed by 5 cycles at 0.1C. Discharge capacities were adapted to match the 3rd cycle at 0.1C to reflect real capacities of the cells for further tests. Adjusted specific capacities are 123 mA h g⁻¹ for both 0PMA and 25PMA, and 125 mA h g⁻¹ for 50PMA. Subsequent rate capability tests were conducted at 4 different C-rates (0.2C, 0.5C, 1C and 0.1C) with 10 symmetric charge/discharge cycles each. These constant current constant voltage (CCCV) tests were performed within a potential range of 3 to 4.2 V. Additionally, the cycling behavior at 0.2C was investigated for 100 cycles.

Electrochemical impedance spectroscopy (EIS) was carried out in half cell configuration against Li metal to help understand transfer phenomena during the formation cycles at 3 V, 100% depth of discharge (DOD). Spectra were recorded on a Biologic-VSP in a range between 500 kHz and 500 mHz using a voltage amplitude of 10 mV.

3. Results

3.1. Electrode Characterization

SEM images give insights into the morphology of the electrodes at the top region of the coating (Figure 1). At low magnification (3kx), the coatings containing PMA appear more continuous than the 0PMA sample, in which crevices between the NMC particles are visible in Figure 1a,c,e. At higher magnifications (10kx) (Figure 1b,d,f), the distinguishability between the NMC secondary particles is clearer for 0PMA than for the other samples. In Figure 1b, typical round shaped secondary NMC particles (purple) with a diameter of approximately 10 μm can be distinguished from the smaller CB particles (yellow) and the flake-like KS6L graphite (green). The difference between 25PMA and 50PMA samples is less pronounced compared to the sample without PMA in the top layer. Cross-section images taken via digital microscope are shown in Figure A3. 0PMA (Figure A3c) shows clear differentiation between the bottom and top layer. Similarly, the two layers are distinguishable for 0PMA and 50PMA in the SEM images (Figure A3b,f). 25PMA shows no definite interface between the layers (Figure A3d) in the investigated electrode section. While pores and cavities are visible in the bottom layers of 0PMA and 25PMA (Figure A3b,d), for 50PMA only few pores can be detected (Figure A3f). It must be pointed out that by nature,

the investigated sections of SEM images are comparably small and further interpretation should be taking carefully.

Omitting PMA in the top-layer causes an increase in electrical resistance. The investigation of the electrical resistance leads to values of $2.12\ \Omega$, $0.71\ \Omega$, and $0.83\ \Omega$ for 0PMA, 25PMA, and 50PMA, respectively, which were calculated by analyzing the slopes of the I–V curves in Figure A4.

Raman spectroscopy was performed to verify the differences in material distribution, visible in the SEM images. Figure 2a shows the median of all recorded spectra after background correction. The peak intensity at $522\ \text{cm}^{-1}$ is assigned to NMC811 [47,48] and is approximately 50% higher for 0PMA than for the other two electrodes. After normalizing the spectra (Figure 2b), two particular regions in a range of $900\text{--}1300\ \text{cm}^{-1}$ and $1500\text{--}1700\ \text{cm}^{-1}$ show clear features displayed in Figure 2c and Figure 2d, respectively.

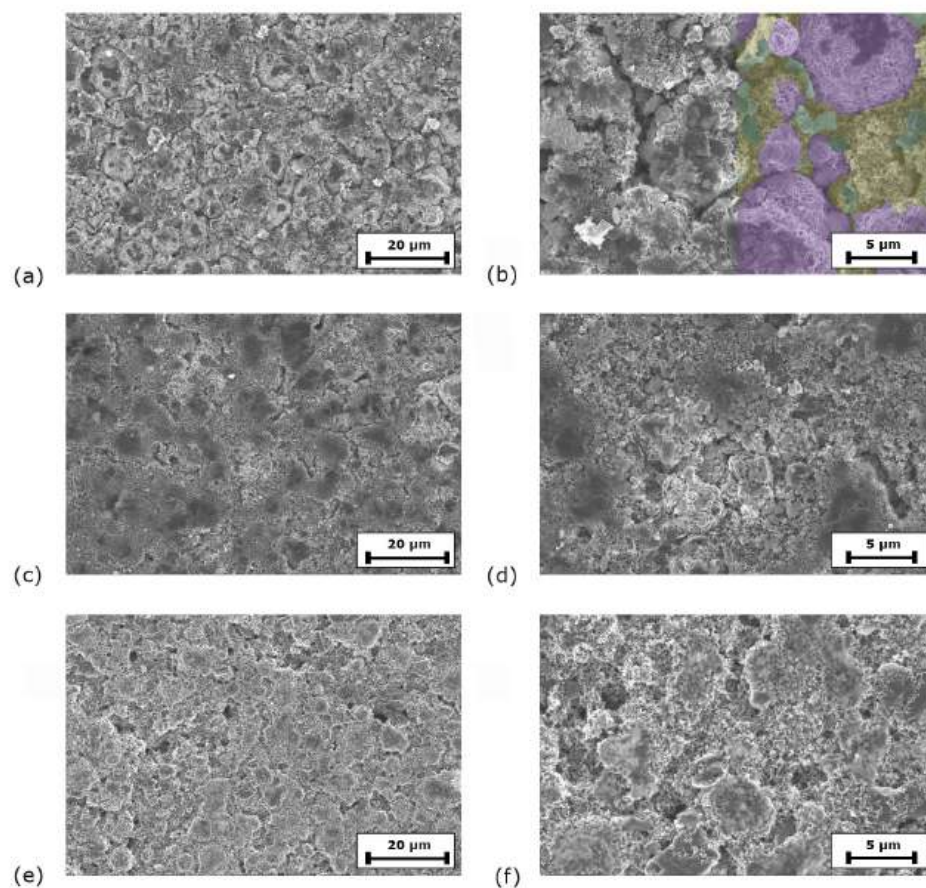


Figure 1. SEM images of (a,b) 0PMA (NMC811 particles in purple, KS6L graphite in green and CB in yellow; larger image shown in Figure A2), (c,d) 25PMA and (e,f) 50PMA at two different magnifications each.

The peaks at $1570\ \text{cm}^{-1}$ correspond to the G-band peak of graphite [49,50]. The absence of a pronounced peak at $1345\ \text{cm}^{-1}$ (graphite D-band) [49,50] indicates a higher concentration of the graphite additive KS6L in comparison to carbon black, where both D- and G-band peaks have similar intensities (Figure A1b,c).

The peak at $1070\ \text{cm}^{-1}$ originates from the LiOH formed during the slurry mixing process [51]. The peak is partially overlapped by vibrational modes (ν_1 and ν_3) [52] arising from Li_3PO_4 formed during the reaction of LiOH with H_3PO_4 [53]. Increasing pH values due to the rising concentration of LiOH inside the slurry are suppressed by incorporation of phosphoric acid into the mixture. Phosphates formed on the surface of the NMC secondary particles prevent extensive Li^+ leaching and, thus, an increase in pH above the corrosion limit of 8.6.

PMA binder is dispersed in a 40 wt% solution of water and added during the last step of the mixing process. This increases the amount of LiOH, comparing the intensities of the 1070 cm^{-1} peaks in Figure 2c.

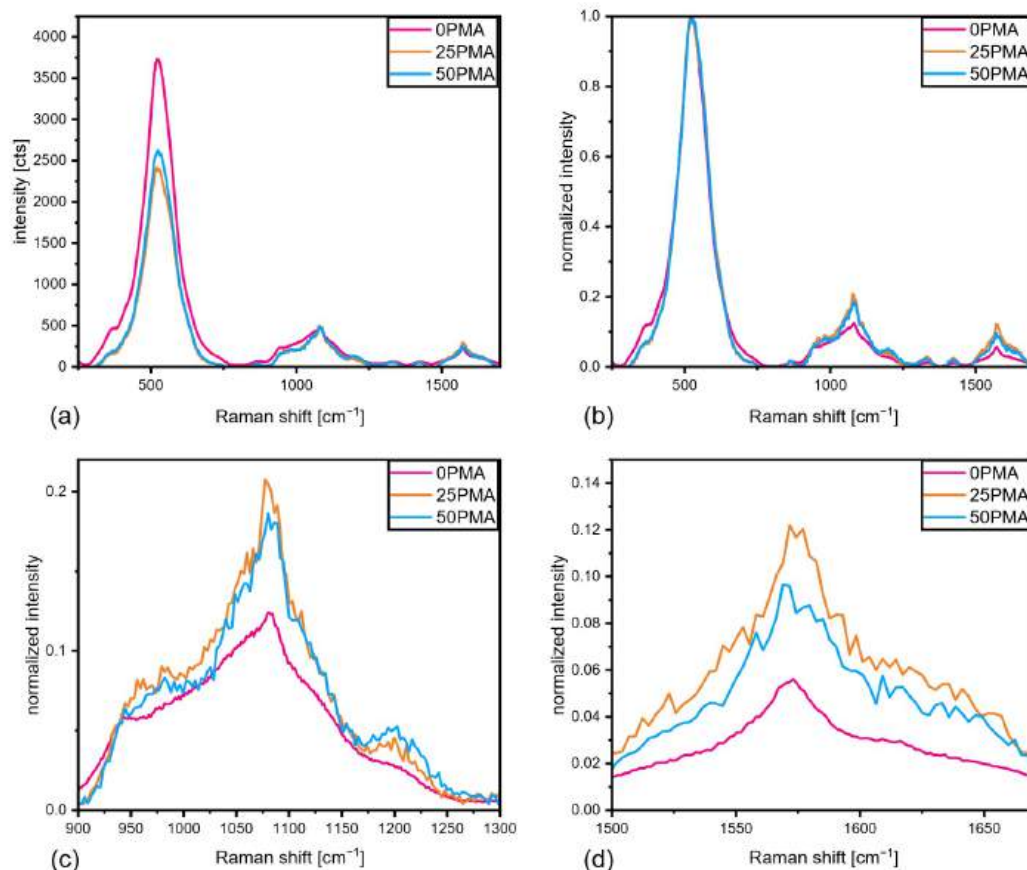


Figure 2. (a) Raman spectra comparison of measured intensities, (b) normalized Raman spectra, (c) zoomed-in section between 900 and 1300 cm^{-1} , (d) zoomed-in section between 1500 and 1700 cm^{-1} .

3.2. Electrochemical Cell Performance

Rate capability tests were performed at different current densities from 0.05C to 1C . The results are shown in Figure 3a. To see the improvement over a multi-layered cathode without any binder tuning, ML coatings from previous studies [8] were included in this graph. Formation cycles are not displayed. The first 5 cycles at 0.1C are marked with an asterisk to show that nominal capacities were adjusted for the following cycles. The irregularities seen at a C-rate of 0.2C for the 0PMA sample are due to power shortages of the cycling instrument and are present in all cells with assembled 0PMA electrodes. At low current densities (0.1C and 0.2C), binder reduction seems to have little impact on the specific discharge capacity—the difference stays within a range of $\pm 5\%$ with regard to ML. Significant improvements can be achieved at higher C-rates. At 0.5C an increase of around 10% can be obtained, with 25PMA having the highest specific discharge capacity of 156 mAh g^{-1} . 50PMA and 25PMA benefit from a reduction in binder content at a C-rate of 1C , resulting in a 24% and 27% increase, respectively. 0PMA and ML similarly show lower values. Averaged results of specific discharge capacities are displayed in Table 3 for all samples and C-rates. The specific discharge capacities for 100 cycles at 0.2C are shown in Figure 3b. ML electrodes hold 89% of their initial specific discharge capacity after 100 cycles. In comparison, tuned cathodes performed slightly superior with 0PMA at 91% and both 25PMA and 50PMA at 93% of their original capacity values.

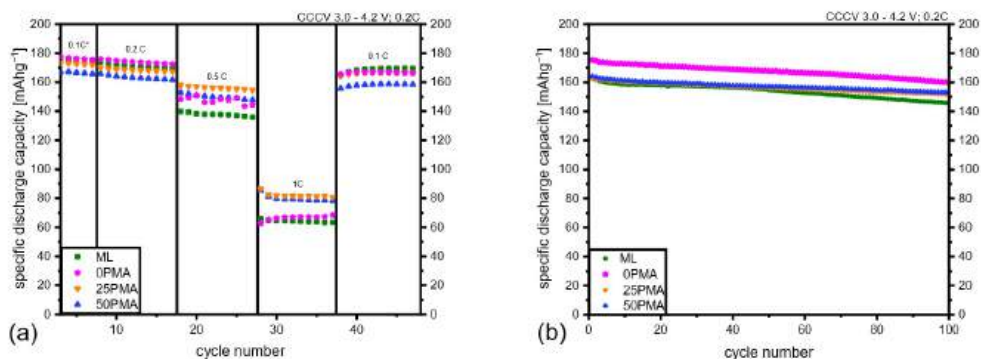


Figure 3. (a) Rate capability test including ML samples from a previous study [8] and (b) results of 100 cycles at 0.2C. A plot including error bars is attached to the Appendix (Figure A5).

Table 3. Specific discharge capacities [mA h g⁻¹] for different C-rates of all tested samples, including ML samples as reference [8]. Results are averaged over all cycles of the specific C-rate and standard deviations (SD) calculated.

Sample	0.1C [mA h g ⁻¹]	SD	0.2C [mA h g ⁻¹]	SD	0.5C [mA h g ⁻¹]	SD	1C [mA h g ⁻¹]	SD	0.1C [mA h g ⁻¹]	SD
OPMA	176	1.82	174	1.36	148	2.53	67	0.39	169	0.86
25PMA	173	4.65	158	6.49	156	4.74	82	7.12	169	6.74
50PMA	167	1.33	163	2.24	150	1.8	80	3.07	159	0.6
ML	176	0.44	171	0.63	138	9.8	64	9.12	170	2.48

Electrochemical impedance spectra were measured to investigate transport phenomena during the formation cycles. Figure 4a,b show a comparison of all Nyquist plots of OPMA, 25PMA, and 50PMA cells at 100%DOD during the first and second cycles. First cycle impedance spectra of 25PMA and 50PMA show a similarly small semi-circle in contrast to OPMA. An increase in impedance for both OPMA and 50PMA is detectable after the second cycle, whereas 25PMA shows no significant change (Figure 4c–e). Voltage curves associated to the EIS measurements are displayed in Figure A6. The shapes of the voltage profiles for 25PMA and 50PMA are similar for both cycles.

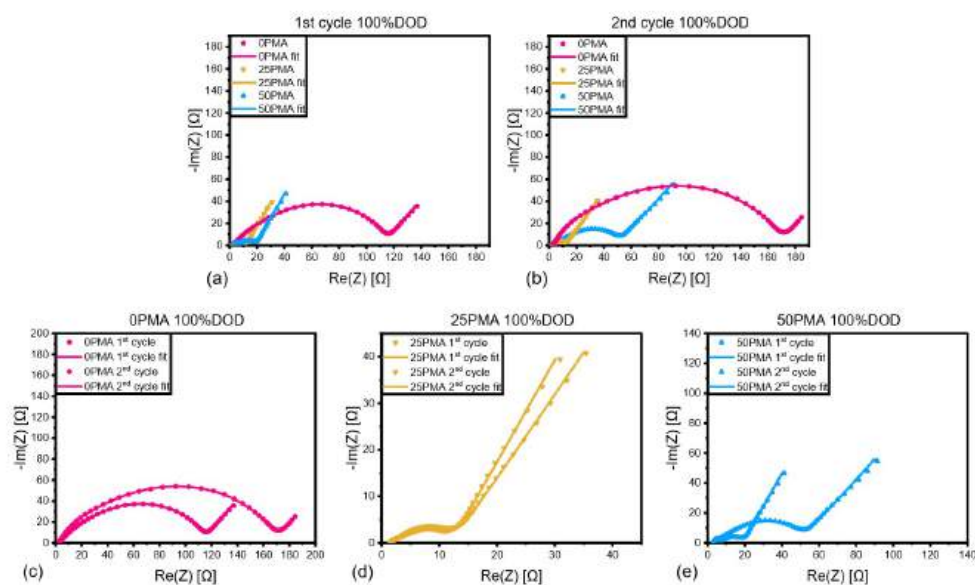


Figure 4. Comparison of EIS spectra for different electrode types with included fit of (a) 1st cycle and (b) 2nd cycle at 100% depth of discharge. Zoomed in spectra comparing 1st and 2nd cycle of (c) OPMA, (d) 25PMA and (e) 50PMA.

4. Discussion

Investigations of the electrodes' morphology, as well as results from electrochemical analysis, reveal correlations between sufficient electronic conductivity of the electrode and cycling performance. Reducing the amount of insulating PMA in the top layer causes a decrease in electrical resistance. Top-view SEM images (Figure 1) indicate that without any PMA binder the slurry components can be differentiated clearly for 0PMA, in contrast to 25PMA and 50PMA samples. This can be linked to the ability to form strong bonds between the carbon particles and the active material. A well-integrated carbon-binder domain contributes positively to electron transport by building up a conductive network. At the same time, excessive CBD presence may lead to a blockage of the active surface [21]. This explains, on the one hand, the poor cycling performance of 0PMA at 1C. A small amount of binder is necessary to maintain the connection between conducting carbon entities and active material throughout the coating. On the other hand, a general reduction in PMA can increase the amount of active surface accessible, explaining the increase in specific discharge capacity for 25PMA and 50PMA for higher current densities. Raman spectra indicate that a noticeable amount of LiOH was formed by reaction of leached Li^+ in the aqueous slurry. This explains that even for low current densities a decrease in specific discharge capacity arises compared to the theoretically assumed value of 200 mA h g^{-1} .

To further investigate the differences in cycling behavior of the samples' specific charge and discharge capacities of representative cycles against voltage and at different C-rates are displayed in Figure 5. The horizontal region in all curves represents the constant voltage step of each charging cycle. Comparison of the individual contributions to the charge capacity, which is in direct proportion to the resistance of the cell, is in accordance with the higher resistance measured during chronoamperometry and EIS. As shown in Figure 6, the potentiostatic contribution to the specific charge capacity increases with current density. The ratio of galvanostatic to potentiostatic share at 1C is strongly in favor of constant voltage contributions for 0PMA. For 25PMA and 50PMA a smaller share, arising from the CV charging step is registered. Table 4 shows average values of galvanostatic and potentiostatic contributions to the specific discharge capacities for different C-rates.

Figure 7 shows differential plots dQ/dV vs. voltage for all samples. Characteristic peaks for NMC811 [54] are clearly visible in the differential plot at 0.2C (Figure 7a). The anodic peaks at $\sim 3.7 \text{ V}$ correspond to the phase transitions between hexagonal (H1) and monoclinic phase (M). Features at $\sim 3.9 \text{ V}$ and $\sim 4.15 \text{ V}$ indicate transitions between the phases $\text{M} \rightarrow \text{H2}$, and $\text{H2} \rightarrow \text{H3}$, respectively. However, the latter does not appear within the tested voltage range for 0PMA. Lithiation of the graphite is represented by the broad peaks at $\sim 3.5 \text{ V}$. Increasing the current density leads to a peak shift to higher voltages and a decreased capacity, which is represented by the area underneath the curve. This behavior is in accordance with the voltage plot in Figure 5.

Table 4. Average values of galvanostatic (CC) and potentiostatic (CV) contributions to the specific charge capacity for different C-rates.

Sample		0.2C	0.5C	1C
0PMA	CC	90%	73%	40%
	CV	10%	27%	60%
25PMA	CC	95%	82%	57%
	CV	5%	18%	43%
50PMA	CC	95%	79%	49%
	CV	5%	21%	51%

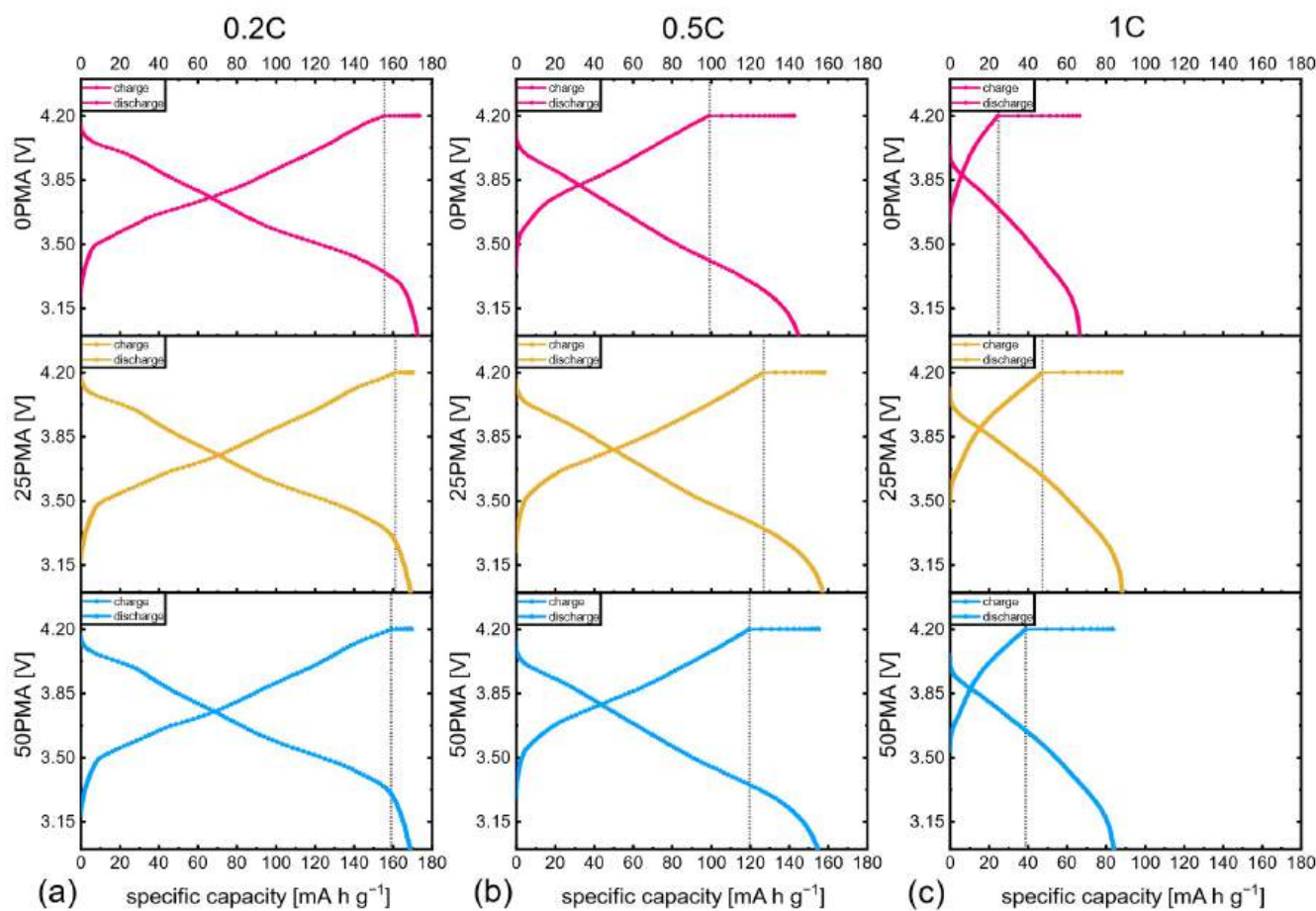


Figure 5. Voltage profiles of all samples at different C-rates (a) 0.2C, (b) 0.5C, (c) 1C.

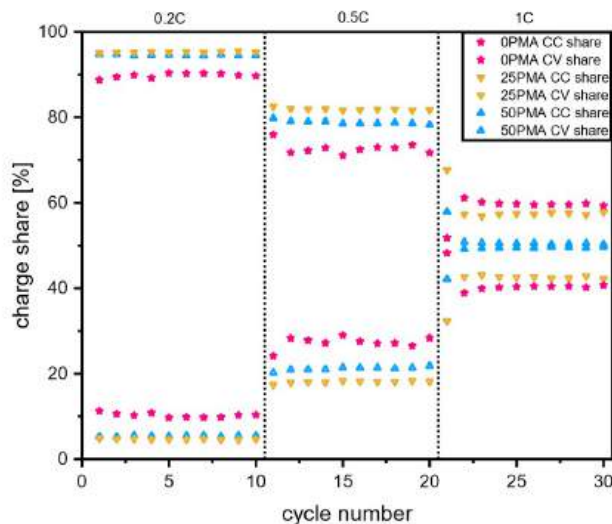


Figure 6. Galvanostatic (CC) and potentiostatic (CV) contributions to the specific charge capacities for 0.2C, 0.5C, and 1C. A plot including error bars is attached to the Appendix A (Figure A7).

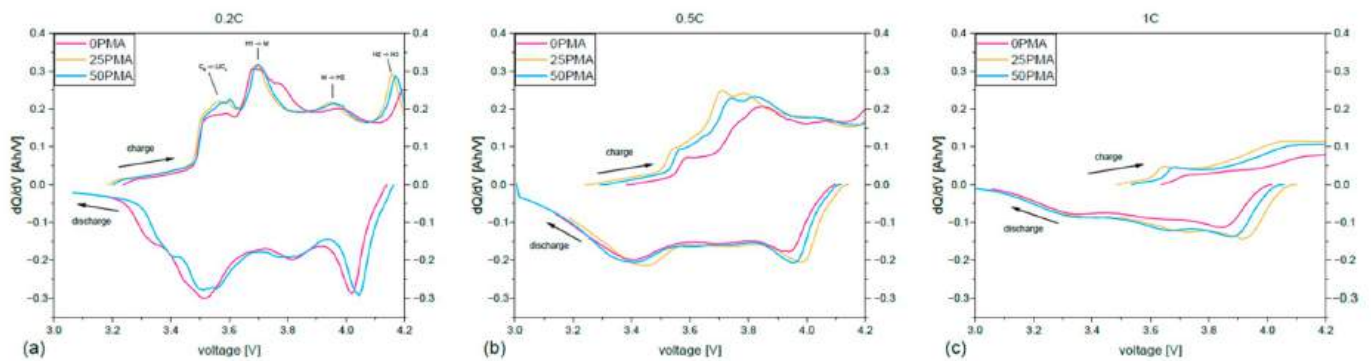


Figure 7. Differential plots for (a) 0.2C, (b) 0.5C, and (c) 1C.

To interpret EIS results, an appropriate equivalent circuit (Figure 8) was used to fit the recorded data according to Zhuang et al. [55]. L represents the inductive behavior arising from the cables connecting the cellholders with the potentiostat. Resistance contributions to R_S include the electrolyte and all cell components (separator, current collector). A constant phase element (Q_{CEI}) and a corresponding resistance R_{CEI} are used to fit the resistance share of the cathode electrolyte interphase (CEI). Middle to high-frequency regions are related to electronic resistances of the material within the coating and are represented by Q_e and R_e . The double-layer capacitance Q_{dl} and the charge transfer resistance R_{ct} depict the charge transfer between electrode and electrolyte. Li^+ diffusion within the active material can not be accurately modeled with a Warburg element at low frequencies and, thus, is represented by the constant phase element Q_D .

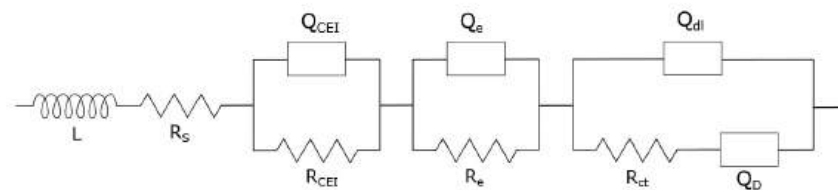


Figure 8. Equivalent circuit model used for EIS fitting.

Contributions of the individual resistances R_S , R_{CEI} , R_e , and R_{ct} to the overall resistance can be interpreted through an appropriate curve fit. Inductance values for all samples are in the magnitude of several nano Henry (nH) and, therefore, neglectable. Bulk resistances R_S show only marginal differences (Figure 9a and Table 5) due to the utilization of identical cell components besides the cathodes. They can be determined by $Re(Z)$ intercepts at high frequencies. The cathode electrolyte interphase resistance (R_{CEI}) values are displayed in Figure 9b and are significantly higher for 25PMA and 50PMA cells. This increase in R_{CEI} originates from the additional phosphates and LiOH covering the NMC particles detected via Raman spectroscopy (Section 3.1), which produce a thicker protective layer. According to Källquist et al., the exact ratio of all electrode components has an impact on CEI evolution [56]. Both R_S and R_{CEI} show only minor variations after the first and second cycles, for all three cell types. The aforementioned missing inter-particle connection through a conductive CBD bridge, which was detected in SEM images (Figure 1b), shows its effect also during EIS measurements. 0PMA samples show a severe increase in electronic resistance R_e compared to 25PMA and 50PMA. Charge transfer resistances R_{ct} are depicted by semicircles in the mid to low frequency region of the Nyquist plot. Values illustrated in Figure 9d for 25PMA and 50PMA are notably lower compared to 0PMA. Both elementary processes of electron conduction across the electrode thickness and the electrochemical insertion of electrons into the active material [57] are negatively effected by the missing CBD in 0PMA. The overall high resistances for 0PMA can be considered one of the driving forces for lower specific discharge capacities at 1C. In particular for high current densities,

proper electrical conductivity throughout the electrode is necessary to utilize the maximal capacity of the active material. All additional fitting parameters are displayed in Table A1.

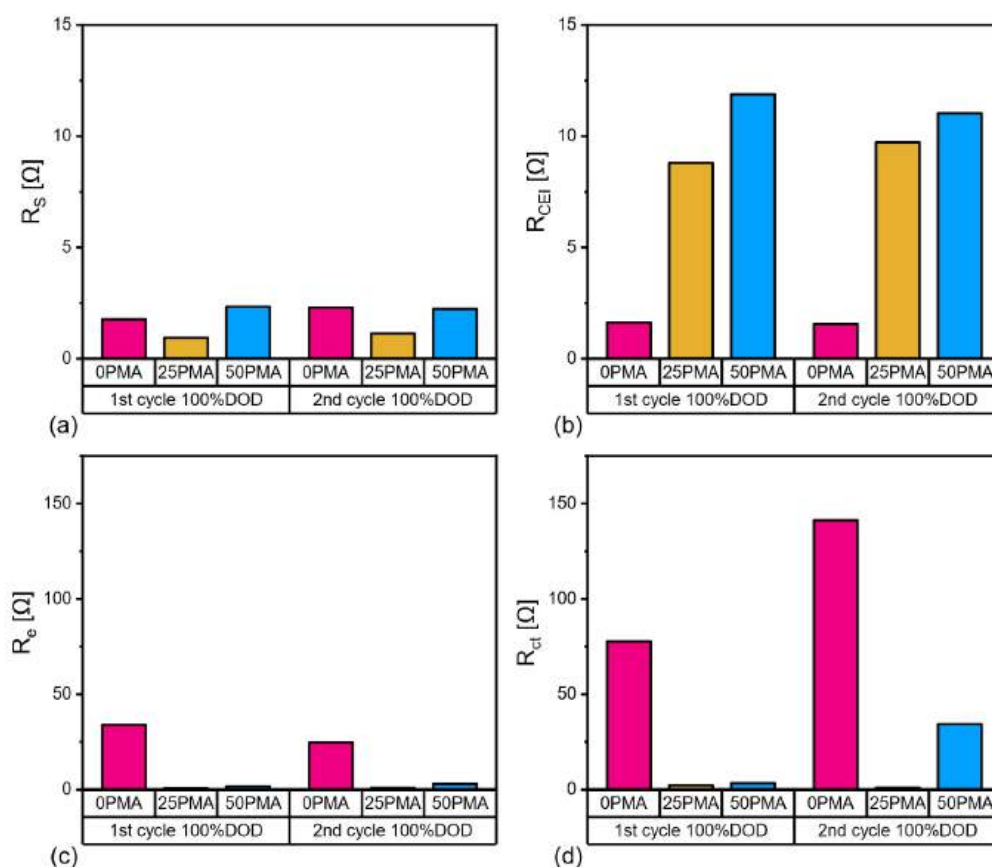


Figure 9. Comparison of contributions (a) R_S , (b) R_{CEL} , (c) R_e and (d) R_{ct} to resistance of 0PMA, 25PMA and 50PMA cells at 100%DOD.

Table 5. Resistance parameters determined from fitting the equivalent circuit model to the spectra.

	Sample	R_S [Ω]	R_{CEL} [Ω]	R_e [Ω]	R_{ct} [Ω]
1st cycle	0PMA	1.77	1.63	33.98	77.69
	25PMA	0.94	8.80	0.59	2.18
	50PMA	2.34	11.88	1.71	3.38
2nd cycle	0PMA	2.30	1.56	24.71	141.23
	25PMA	1.14	9.72	0.81	0.88
	50PMA	2.23	11.04	3.00	34.35

5. Conclusions

The multi-layer coating technique was used as a tool to create binder gradients within water-based NMC811 cathodes of high loading. It was demonstrated that this method can efficiently be applied to vary binder concentrations at pilot scale. Two samples with reduced amounts of poly(methyl) acrylic binder and one completely free of PMA in the top-layer were successfully fabricated on an R2R pilot line. In contrast to our previous findings [8] regarding the concept of multi-layering for manufacturing thick, high-energy NMC811 cathodes; we herein present the binder gradient influence on the electrochemical performance—related to the amount of PMA incorporated in the upper layer. Depending on the amount of the studied binder at the top layer, the particle connection and correlated electronic conductivity to achieve high current capability is increased or reduced. An

optimum was found at 25% PMA within the studied range at 1C. The binder reduction effectively increases the specific discharge capacity values compared to samples without binder gradients. Cathodes with a decreased amount of PMA outperform unmodified multi-layer electrodes by up to 28% at 1C. Summarizing the analysis of the electrode characteristics and electrochemical tests, an inter dependency between cycling performance and inter-particle conductivity was observed. Complete omission of PMA leads to an insufficient embedding of carbon particles (both CB and graphite) within the binder matrix. This missing link between the active materials has severe consequences for electronic and charge transfer resistance. These studies pave the way towards sustainably processed high current capable, highly loaded NMC811 cathode containing Li-ion batteries for future applications.

Author Contributions: Conceptualization, L.N.; methodology, L.N.; validation, L.N.; formal analysis, L.N.; investigation, L.N.; resources, K.F. and M.J.; writing—original draft preparation, L.N.; writing—review and editing, L.N., K.F., M.J. and F.W.; visualization, L.N.; supervision, K.F. and F.W.; project administration, K.F. and M.J.; funding acquisition, M.J. All authors have read and agreed to the published version of the manuscript.

Funding: This research was funded by the Austrian Federal Ministry for Climate Action, Environment, Energy, Mobility, Innovation and Technology (BMK).

Institutional Review Board Statement: Not applicable.

Informed Consent Statement: Not applicable.

Data Availability Statement: The data presented in this study are available on request from the corresponding author.

Acknowledgments: The authors would like to thank Christiane Groher and Ningxin Zhang for performing the SEM measurements reported herein. In addition we would like to acknowledge the support from Michael Höchtl during the analysis of the Raman data. Sample preparation for SEM cross-sections was carried out using facilities at the University Service Centre for Transmission Electron Microscopy, Vienna University of Technology, Austria.

Conflicts of Interest: The authors declare no conflict of interest.

Appendix A

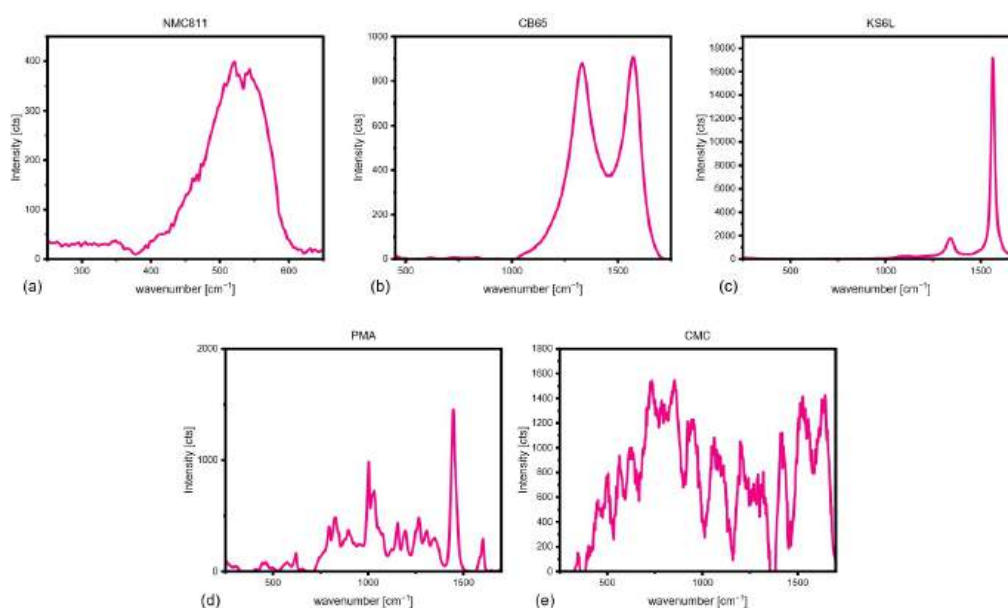


Figure A1. Raman spectra of all materials used for slurry mixing (a) NMC811, (b) KS6L, (c) CB65, (d) PMA, (e) CMC.

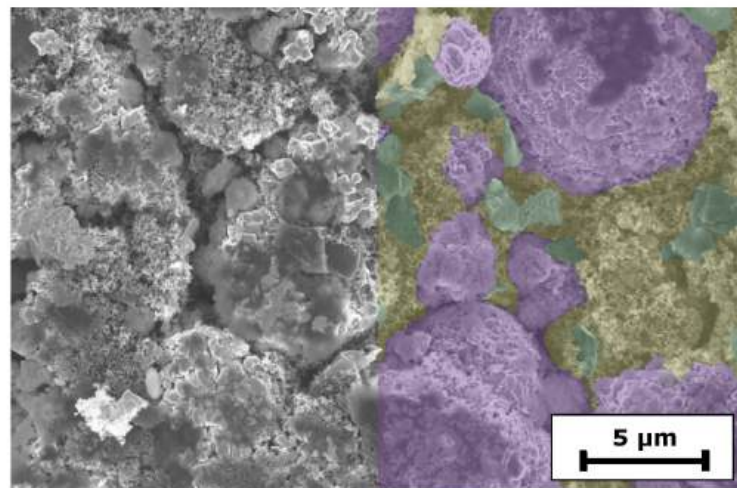


Figure A2. Top-view SEM image of 0PMA. Species are colored in purple (NMC811), green (KS6L graphite), and yellow (CBD).

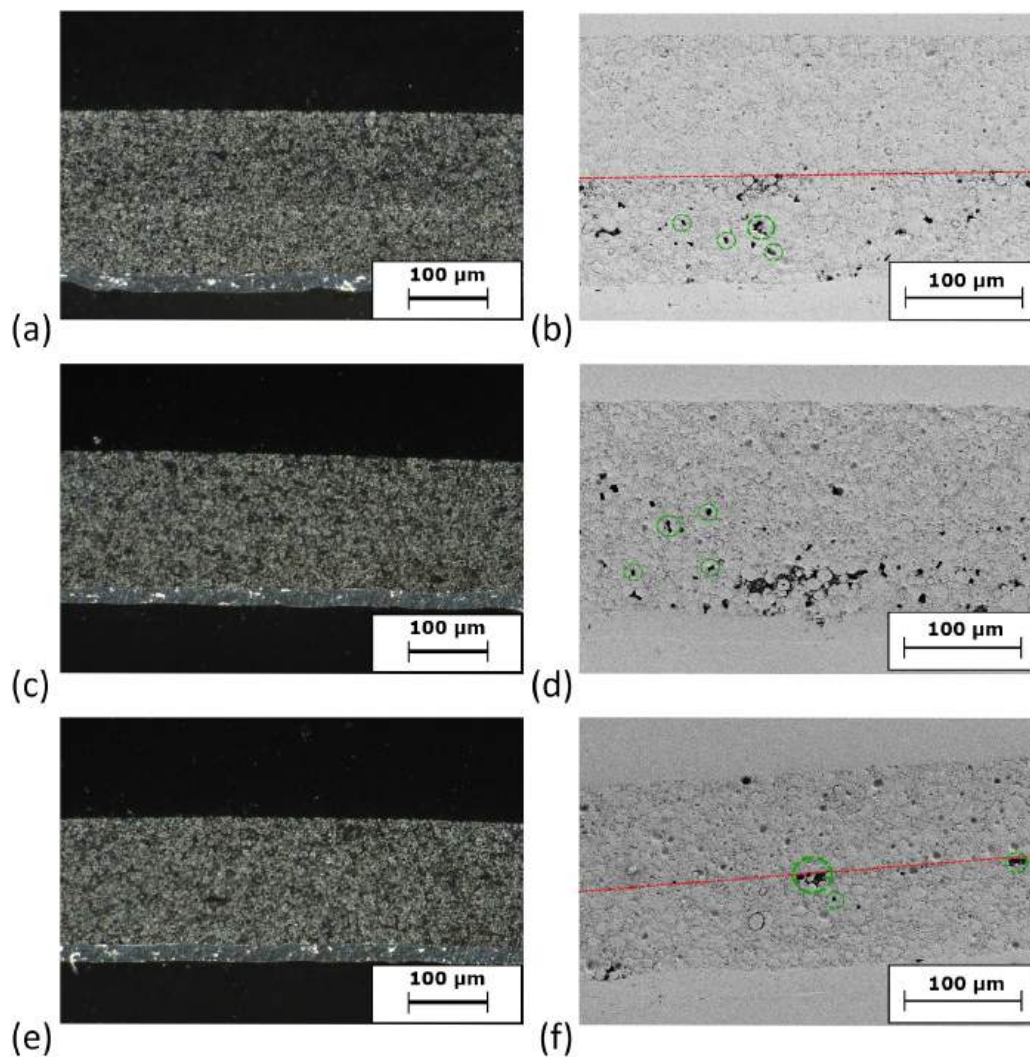


Figure A3. Cross-section images of (a,b) 0PMA, (c,d) 25PMA and (e,f) 50PMA. The left column shows images taken via digital microscope. The right column shows SEM images. Dotted red lines indicate the interface of the two layers, while green circles highlight examples for pores.

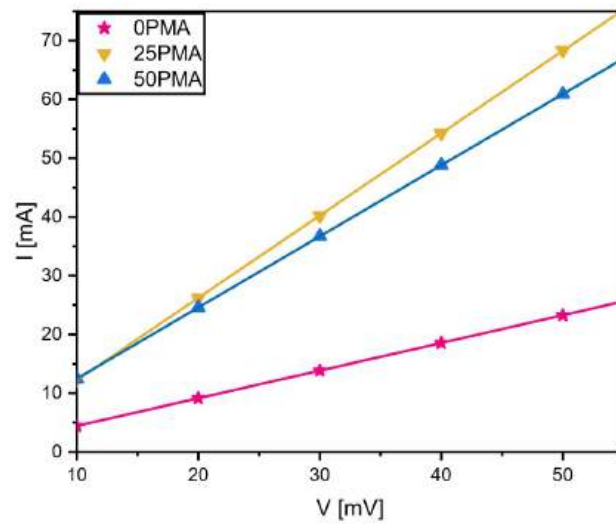


Figure A4. I-V curves resulting from chronoamperometry measurements.

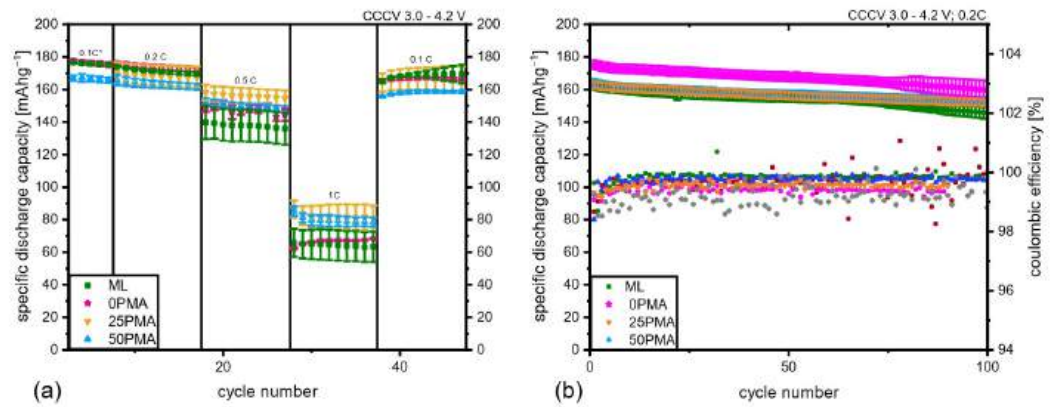


Figure A5. (a) Rate capability test including ML samples from a previous study [8], (b) results of 100 cycles at 0.2C including coulombic efficiencies and statistical errors.

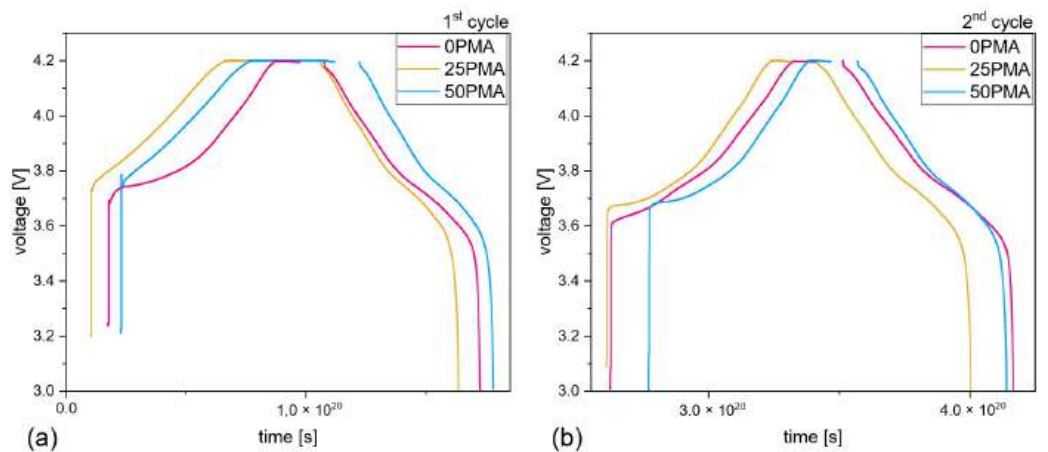


Figure A6. Voltage curves associated to the investigated EIS cycles. (a) 1st cycle and (b) 2nd cycle.

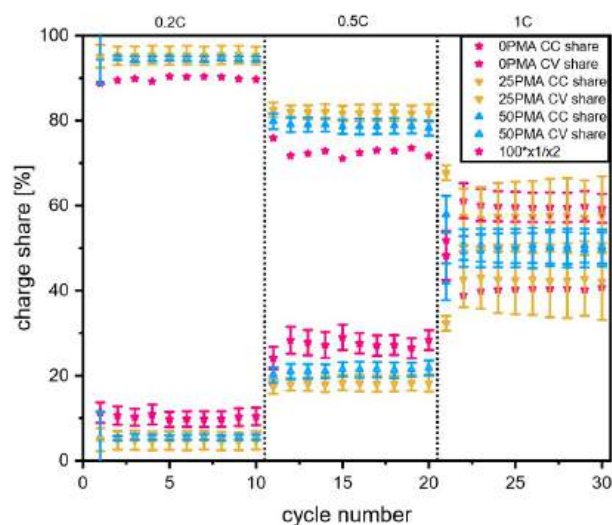


Figure A7. Galvanostatic (CC) and potentiostatic (CV) contributions to the specific charge capacities for 0.2C, 0.5C, and 1C.

Table A1. Parameters of constant phase elements determined from fitting the equivalent circuit model to the spectra and error value of the fit.

	Sample	Q_{CEI} [mF]	α_{CEI}	Q_e [μ F]	α_e	Q_{dl} [mF]	α_{dl}	Q_D [mF]	α_D	χ^2
1st cycle	0PMA	4.01×10^{-2}	0.72	22.78	0.84	4.55×10^{-4}	1.00	11.00	0.64	0.002
	25PMA	4.51×10^{-1}	0.66	1.25	1.00	4.59×10^{-1}	0.57	7.69	0.74	0.008
	50PMA	3.50×10^{-1}	0.68	19.13	0.87	2.31×10^{-3}	1.00	8.10	0.73	0.003
2nd cycle	0PMA	5.07×10^{-4}	1.00	11.42	0.85	2.08×10^{-2}	0.79	16.37	0.63	0.002
	25PMA	3.05×10^{-1}	0.73	0.84	1.00	5.62×10^{-2}	0.84	9.38	0.68	0.006
	50PMA	7.07×10^{-2}	0.68	0.27	1.00	4.03×10^{-2}	0.84	7.01	0.60	0.004

References

- Du, Z.; Wood, D.L.; Daniel, C.; Kalnaus, S.; Li, J. Understanding limiting factors in thick electrode performance as applied to high energy density Li-ion batteries. *J. Appl. Electrochem.* **2017**, *47*, 405–415. [\[CrossRef\]](#)
- Kuang, Y.; Chen, C.; Kirsch, D.; Hu, L. Thick electrode batteries: Principles, opportunities, and challenges. *Adv. Energy Mater.* **2019**, *9*, 1901457. [\[CrossRef\]](#)
- Font, F.; Protas, B.; Richardson, G.; Foster, J.M. Binder migration during drying of lithium-ion battery electrodes: Modelling and comparison to experiment. *J. Power Sources* **2018**, *393*, 177–185. [\[CrossRef\]](#)
- Jaiser, S.; Müller, M.; Baunach, M.; Bauer, W.; Scharfer, P.; Schabel, W. Investigation of film solidification and binder migration during drying of Li-Ion battery anodes. *J. Power Sources* **2016**, *318*, 210–219. [\[CrossRef\]](#)
- Baunach, M.; Jaiser, S.; Schmelzle, S.; Nirschl, H.; Scharfer, P.; Schabel, W. Delamination behavior of lithium-ion battery anodes: Influence of drying temperature during electrode processing. *Dry. Technol.* **2016**, *34*, 462–473. [\[CrossRef\]](#)
- Westphal, B.G.; Kwade, A. Critical electrode properties and drying conditions causing component segregation in graphitic anodes for lithium-ion batteries. *J. Energy Storage* **2018**, *18*, 509–517. [\[CrossRef\]](#)
- Pfleging, W. Recent progress in laser texturing of battery materials: A review of tuning electrochemical performances, related material development, and prospects for large-scale manufacturing. *Int. J. Extrem. Manuf.* **2020**, *3*, 012002. [\[CrossRef\]](#)
- Neidhart, L.; Fröhlich, K.; Eshraghi, N.; Cupid, D.; Winter, F.; Jahn, M. Aqueous Manufacturing of Defect-Free Thick Multi-Layer NMC811 Electrodes. *Nanomaterials* **2022**, *12*, 317. [\[CrossRef\]](#)
- Diehm, R.; Kumberg, J.; Dörner, C.; Müller, M.; Bauer, W.; Scharfer, P.; Schabel, W. In Situ Investigations of Simultaneous Two-Layer Slot Die Coating of Component-Graded Anodes for Improved High-Energy Li-Ion Batteries. *Energy Technol.* **2020**, *8*, 1901251. [\[CrossRef\]](#)

10. Wood, M.; Li, J.; Du, Z.; Daniel, C.; Dunlop, A.R.; Polzin, B.J.; Jansen, A.N.; Krumdick, G.K.; Wood, D.L., III. Impact of secondary particle size and two-layer architectures on the high-rate performance of thick electrodes in lithium-ion battery pouch cells. *J. Power Sources* **2021**, *515*, 230429. [[CrossRef](#)]
11. Kalnaus, S.; Livingston, K.; Hawley, W.B.; Wang, H.; Li, J. Design and processing for high performance Li ion battery electrodes with double-layer structure. *J. Energy Storage* **2021**, *44*, 103582. [[CrossRef](#)]
12. Kespe, M.; Cernak, S.; Gleiß, M.; Hammerich, S.; Nirschl, H. Three-dimensional simulation of transport processes within blended electrodes on the particle scale. *Int. J. Energy Res.* **2019**, *43*, 6762–6778. [[CrossRef](#)]
13. Liu, L.; Guan, P.; Liu, C. Experimental and simulation investigations of porosity graded cathodes in mitigating battery degradation of high voltage lithium-ion batteries. *J. Electrochem. Soc.* **2017**, *164*, A3163. [[CrossRef](#)]
14. Qi, Y.; Jang, T.; Ramadesigan, V.; Schwartz, D.T.; Subramanian, V.R. Is there a benefit in employing graded electrodes for lithium-ion batteries? *J. Electrochem. Soc.* **2017**, *164*, A3196. [[CrossRef](#)]
15. Müller, D.; Landa-Medrano, I.; Eguia-Barrío, A.; Boyano, I.; Urdampilleta, I.; de Meatza, I.; Fill, A.; Birke, P. Electrochemical characterization of bi-layered graphite anodes combining high and low porosity in lithium-ion cells to improve cell performance. *Electrochim. Acta* **2021**, *391*, 138966. [[CrossRef](#)]
16. Dai, Y.; Srinivasan, V. On graded electrode porosity as a design tool for improving the energy density of batteries. *J. Electrochem. Soc.* **2015**, *163*, A406. [[CrossRef](#)]
17. Liu, D.; Chen, L.C.; Liu, T.J.; Chu, W.B.; Tiu, C. Improvement of lithium-ion battery performance by two-layered slot-die coating operation. *Energy Technol.* **2017**, *5*, 1235–1241. [[CrossRef](#)]
18. Kim, K.M.; Jeon, W.S.; Chung, I.J.; Chang, S.H. Effect of mixing sequences on the electrode characteristics of lithium-ion rechargeable batteries. *J. Power Sources* **1999**, *83*, 108–113. [[CrossRef](#)]
19. Wang, M.; Dang, D.; Meyer, A.; Arsenaault, R.; Cheng, Y.T. Effects of the mixing sequence on making lithium ion battery electrodes. *J. Electrochem. Soc.* **2020**, *167*, 100518. [[CrossRef](#)]
20. Lombardo, T.; Ngandjong, A.C.; Belhacen, A.; Franco, A.A. Carbon-Binder Migration: A Three-Dimensional Drying Model for Lithium-ion Battery Electrodes. *Energy Storage Mater.* **2021**, *43*, 337–347. [[CrossRef](#)]
21. Hein, S.; Danner, T.; Westhoff, D.; Prifling, B.; Scurtu, R.; Kremer, L.; Hoffmann, A.; Hilger, A.; Osenberg, M.; Manke, I.; et al. Influence of conductive additives and binder on the impedance of lithium-ion battery electrodes: Effect of morphology. *J. Electrochem. Soc.* **2020**, *167*, 013546. [[CrossRef](#)]
22. Usseglio-Viretta, F.L.; Colclasure, A.M.; Dunlop, A.R.; Trask, S.E.; Jansen, A.N.; Abraham, D.P.; Rodrigues, M.T.F.; Dufek, E.J.; Tanim, T.R.; Chinnam, P.R.; et al. Carbon-Binder Weight Loading Optimization for Improved Lithium-Ion Battery Rate Capability. *J. Electrochem. Soc.* **2022**, *169*, 070519. [[CrossRef](#)]
23. Gordon, R.; Orias, R.; Willenbacher, N. Effect of carboxymethyl cellulose on the flow behavior of lithium-ion battery anode slurries and the electrical as well as mechanical properties of corresponding dry layers. *J. Mater. Sci.* **2020**, *55*, 15867–15881. [[CrossRef](#)]
24. Lopez, C.G.; Richtering, W. Oscillatory rheology of carboxymethyl cellulose gels: Influence of concentration and pH. *Carbohydr. Polym.* **2021**, *267*, 118117. [[CrossRef](#)] [[PubMed](#)]
25. Lee, J.H.; Paik, U.; Hackley, V.A.; Choi, Y.M. Effect of carboxymethyl cellulose on aqueous processing of natural graphite negative electrodes and their electrochemical performance for lithium batteries. *J. Electrochem. Soc.* **2005**, *152*, A1763. [[CrossRef](#)]
26. Yen, J.P.; Chang, C.C.; Lin, Y.R.; Shen, S.T.; Hong, J.L. Effects of styrene-butadiene rubber/carboxymethylcellulose (SBR/CMC) and polyvinylidene difluoride (PVDF) binders on low temperature lithium ion batteries. *J. Electrochem. Soc.* **2013**, *160*, A1811. [[CrossRef](#)]
27. Lingappan, N.; Kong, L.; Pecht, M. The significance of aqueous binders in lithium-ion batteries. *Renew. Sustain. Energy Rev.* **2021**, *147*, 111227. [[CrossRef](#)]
28. Hu, S.; Li, Y.; Yin, J.; Wang, H.; Yuan, X.; Li, Q. Effect of different binders on electrochemical properties of LiFePO₄/C cathode material in lithium ion batteries. *Chem. Eng. J.* **2014**, *237*, 497–502. [[CrossRef](#)]
29. Wang, W.L.; Jin, E.M.; Gu, H.B. Impacts of different polymer binders on electrochemical properties of LiFePO₄ cathode. *Appl. Surf. Sci.* **2013**, *282*, 444–449.
30. Komaba, S.; Yabuuchi, N.; Ozeki, T.; Okushi, K.; Yui, H.; Konno, K.; Katayama, Y.; Miura, T. Functional binders for reversible lithium intercalation into graphite in propylene carbonate and ionic liquid media. *J. Power Sources* **2010**, *195*, 6069–6074. [[CrossRef](#)]
31. Hawley, W.B.; Meyer, H.M., III; Li, J. Enabling aqueous processing for LiNi_{0.80}Co_{0.15}Al_{0.05}O₂ (NCA)-based lithium-ion battery cathodes using polyacrylic acid. *Electrochim. Acta* **2021**, *380*, 138203. [[CrossRef](#)]
32. Spahr, M.E.; Goers, D.; Leone, A.; Stallone, S.; Grivei, E. Development of carbon conductive additives for advanced lithium ion batteries. *J. Power Sources* **2011**, *196*, 3404–3413. [[CrossRef](#)]
33. Sahore, R.; Wood, D.L., III; Kukay, A.; Grady, K.M.; Li, J.; Belharouak, I. Towards understanding of cracking during drying of thick aqueous-processed LiNi_{0.8}Mn_{0.1}Co_{0.1}O₂ cathodes. *ACS Sustain. Chem. Eng.* **2020**, *8*, 3162–3169. [[CrossRef](#)]
34. Loeffler, N.; Kopel, T.; Kim, G.T.; Passerini, S. Polyurethane binder for aqueous processing of Li-ion battery electrodes. *J. Electrochem. Soc.* **2015**, *162*, A2692. [[CrossRef](#)]
35. Ibing, L.; Gallasch, T.; Friesen, A.; Niehoff, P.; Hintennach, A.; Winter, M.; Börner, M. The role of the pH value in water-based pastes on the processing and performance of Ni-rich LiNi_{0.5}Mn_{0.3}Co_{0.2}O₂ based positive electrodes. *J. Power Sources* **2020**, *475*, 228608. [[CrossRef](#)]

36. Kim, J.; Hong, Y.; Ryu, K.S.; Kim, M.G.; Cho, J. Washing effect of a $\text{LiNi}_{0.83}\text{Co}_{0.15}\text{Al}_{0.02}\text{O}_2$ cathode in water. *Electrochem. Solid-State Lett.* **2005**, *9*, A19. [[CrossRef](#)]
37. Shkrob, I.A.; Gilbert, J.A.; Phillips, P.J.; Klie, R.; Haasch, R.T.; Bareño, J.; Abraham, D.P. Chemical weathering of layered Ni-rich oxide electrode materials: Evidence for cation exchange. *J. Electrochem. Soc.* **2017**, *164*, A1489. [[CrossRef](#)]
38. Chatalov, A.Y. Effet du pH sur le comportement électrochimique des métaux et leur résistance à la corrosion. *Dokl. Akad. Nauk SSSR* **1952**, *86*, 775.
39. Kazzazi, A.; Bresser, D.; Birrozzi, A.; von Zamory, J.; Hekmatfar, M.; Passerini, S. Comparative analysis of aqueous binders for high-energy li-rich NMC as a Lithium-Ion cathode and the impact of adding phosphoric acid. *ACS Appl. Mater. Interfaces* **2018**, *10*, 17214–17222. [[CrossRef](#)] [[PubMed](#)]
40. Kukay, A.; Sahore, R.; Parejiya, A.; Hawley, W.B.; Li, J.; Wood, D.L., III. Aqueous Ni-rich-cathode dispersions processed with phosphoric acid for lithium-ion batteries with ultra-thick electrodes. *J. Colloid Interface Sci.* **2021**, *581*, 635–643. [[CrossRef](#)]
41. Carvalho, D.V.; Loeffler, N.; Kim, G.T.; Marinaro, M.; Wohlfahrt-Mehrens, M.; Passerini, S. Study of water-based lithium titanate electrode processing: The role of pH and binder molecular structure. *Polymers* **2016**, *8*, 276. [[CrossRef](#)]
42. Hamam, I.; Zhang, N.; Liu, A.; Johnson, M.; Dahn, J. Study of the reactions between Ni-rich positive electrode materials and aqueous solutions and their relation to the failure of Li-ion cells. *J. Electrochem. Soc.* **2020**, *167*, 130521. [[CrossRef](#)]
43. Li, C.C.; Lee, J.T.; Tung, Y.L.; Yang, C.R. Effects of pH on the dispersion and cell performance of LiCoO_2 cathodes based on the aqueous process. *J. Mater. Sci.* **2007**, *42*, 5773–5777. [[CrossRef](#)]
44. Bauer, W.; Çetinel, F.A.; Müller, M.; Kaufmann, U. Effects of pH control by acid addition at the aqueous processing of cathodes for lithium ion batteries. *Electrochim. Acta* **2019**, *317*, 112–119. [[CrossRef](#)]
45. Zhu, P.; Han, J.; Pfleging, W. Characterization and Laser Structuring of Aqueous Processed $\text{Li}(\text{Ni}_{0.6}\text{Mn}_{0.2}\text{Co}_{0.2})\text{O}_2$ Thick-Film Cathodes for Lithium-Ion Batteries. *Nanomaterials* **2021**, *11*, 1840. [[CrossRef](#)]
46. Li, J.; Zhong, W.; Deng, Q.; Zhang, Q.; Yang, C. Recent progress in synthesis and surface modification of nickel-rich layered oxide cathode materials for lithium-ion batteries. *Int. J. Extrem. Manuf.* **2022**, *4*, 042004. [[CrossRef](#)]
47. Li, T.; Yuan, X.Z.; Zhang, L.; Song, D.; Shi, K.; Bock, C. Degradation mechanisms and mitigation strategies of nickel-rich NMC-based lithium-ion batteries. *Electrochem. Energy Rev.* **2020**, *3*, 43–80. [[CrossRef](#)]
48. Julien, C.M.; Mauger, A. In situ Raman analyses of electrode materials for Li-ion batteries. *AIMS Mater. Sci.* **2018**, *5*, 650–698. [[CrossRef](#)]
49. Tuinstra, F.; Koenig, J.L. Raman spectrum of graphite. *J. Chem. Phys.* **1970**, *53*, 1126–1130. [[CrossRef](#)]
50. Reich, S.; Thomsen, C. Raman spectroscopy of graphite. *Philos. Trans. R. Soc. London. Ser. Math. Phys. Eng. Sci.* **2004**, *362*, 2271–2288. [[CrossRef](#)] [[PubMed](#)]
51. Gorelik, V.; Bi, D.; Voinov, Y.; Vodchits, A.; Gorshunov, B.; Yurasov, N.; Yurasova, I. Raman spectra of lithium compounds. In Proceedings of the Journal of Physics: Conference Series, Moscow, Russia, 25–27 January 2017; IOP Publishing: Bristol, UK, 2017; Volume 918, p. 012035.
52. Smith, R.J.; Shen, Y.; Bray, K.L. The effect of pressure on vibrational modes in Li_3PO_4 . *J. Physics Condens. Matter* **2001**, *14*, 461. [[CrossRef](#)]
53. Sahni, K.; Ashuri, M.; He, Q.; Sahore, R.; Bloom, I.D.; Liu, Y.; Kaduk, J.A.; Shaw, L.L. H_3PO_4 treatment to enhance the electrochemical properties of $\text{Li}(\text{Ni}_{1/3}\text{Mn}_{1/3}\text{Co}_{1/3})\text{O}_2$ and $\text{Li}(\text{Ni}_{0.5}\text{Mn}_{0.3}\text{Co}_{0.2})\text{O}_2$ cathodes. *Electrochim. Acta* **2019**, *301*, 8–22. [[CrossRef](#)]
54. Jung, R.; Metzger, M.; Maglia, F.; Stinner, C.; Gasteiger, H.A. Oxygen release and its effect on the cycling stability of $\text{LiNi}_x\text{Mn}_y\text{Co}_z\text{O}_2$ (NMC) cathode materials for Li-ion batteries. *J. Electrochem. Soc.* **2017**, *164*, A1361. [[CrossRef](#)]
55. Zhuang, Q.C.; Qiu, X.Y.; Xu, S.D.; Qiang, Y.H.; Su, S. Diagnosis of electrochemical impedance spectroscopy in lithium-ion batteries. *Lithium Ion Batter. Dev.* **2012**, *8*, 189–227.
56. Källquist, I.; Le Ruyet, R.; Liu, H.; Mogensen, R.; Lee, M.T.; Edström, K.; Naylor, A.J. Advances in studying interfacial reactions in rechargeable batteries by photoelectron spectroscopy. *J. Mater. Chem. A* **2022**, *10*, 19466–19505. [[CrossRef](#)]
57. Gaberšček, M. Understanding Li-based battery materials via electrochemical impedance spectroscopy. *Nat. Commun.* **2021**, *12*, 1–4. [[CrossRef](#)]

Disclaimer/Publisher’s Note: The statements, opinions and data contained in all publications are solely those of the individual author(s) and contributor(s) and not of MDPI and/or the editor(s). MDPI and/or the editor(s) disclaim responsibility for any injury to people or property resulting from any ideas, methods, instructions or products referred to in the content.

Publication III



Layer by Layer: Improved Tortuosity in High Loading Aqueous NMC811 Electrodes

L. Neidhart,^{1,2,x} K. Fröhlich,¹ B. Boz,¹ F. Winter,² and M. Jahn¹

¹Battery Technologies, Center for Transport Technologies, Austrian Institute of Technology GmbH (AIT), 1210 Vienna, Austria

²Institute of Chemical, Environmental and Bioscience Engineering, TU Wien, 1060 Vienna, Austria

Thick electrode production is a key enabler for realizing high energy density Lithium-ion batteries. Therefore, the investigation of tortuosity as a crucial limiting parameter was conducted in this work. A thickness threshold ($>150 \mu\text{m}$) for a drastic increase in tortuosity for aqueous processed $\text{LiNi}_{0.8}\text{Mn}_{0.1}\text{Co}_{0.1}\text{O}_2$ (NMC811) electrodes was determined. Symmetrical cells, under blocking conditions, were analyzed via electrochemical impedance spectroscopy. To counteract this phenomenon, multi-layer coated electrodes with varying binder concentrations were investigated. This novel coating method, combined with the reduction of binder material, leads to a tortuosity decrease of more than 80%, when compared to high-loading electrodes ($>8.5 \text{ mA h cm}^{-2}$) coated with the conventional doctor-blade technique. Additionally, a simplified transmission line model is opposed to a linear fitting method for analyzing the impedance data.

© 2024 The Author(s). Published on behalf of The Electrochemical Society by IOP Publishing Limited. This is an open access article distributed under the terms of the Creative Commons Attribution 4.0 License (CC BY, <http://creativecommons.org/licenses/by/4.0/>), which permits unrestricted reuse of the work in any medium, provided the original work is properly cited. [DOI: 10.1149/1945-7111/ad47d2]



Manuscript submitted February 9, 2024; revised manuscript received April 23, 2024. Published May 16, 2024.

The growing global demand for sustainable energy solutions has motivated intensive research in advanced energy storage systems. Among others, lithium-ion batteries (LIBs) are a key technology considering propulsion systems for electric vehicles (EVs). As a logical consequence, the development of LIBs increased in importance. However, there is still a great need for optimization concerning range and fast-charging capabilities.

Maximizing the energy density of the whole battery is desired and thus an increase in capacity of a single cell or, in the broadest sense, of the electrodes assembled. Especially for high-loading electrodes, mass transport limitations, can be detrimental to their cycling performance.¹ There are mainly two options to enhance the ionic transport within the electrode. Either utilizing an electrolyte with high ionic conductivity or optimizing the spatial orientation of the material components.² The latter can be achieved by improving the tortuous characteristics of the electrode. The tortuosity (τ) indicates how well ionic transport pathways through the electrode layer are established. It gives information on the deviation from a straight, unhindered ion flux across the electrode.³ In an ideal case, tortuosity has a value of 1—indicating that the shortest pathway is equal to the actual ionic diffusion length. This means, that the ions can migrate in straight lines, orthogonal to the current collector, to directly reach the active material particles close to the substrate foil. Firstly, it is nearly impossible to align all particles during the fabrication process of battery electrodes. Additionally, a well-established through-plane connection between the active material particles and conductive agents can be favorable e.g., for electronic conductivity.⁴ Therefore, τ is always greater than 1 in real applications. However, proper knowledge of its value might lead to a better understanding of performance-limiting features in the cell. In contrast to tortuosity, porosity (ϵ) is a characteristic electrode parameter that has mostly drawn attention during the fabrication process but needs to be addressed carefully. Lowering the porosity minimizes the space between particles and electronic conductivity increases. This happens at the expense of electrolyte wettability and thus also negatively affects the mass transport in the electrode. Another benefit of decreased porosity is the increased energy density of the electrode.

Since the effective diffusion coefficient is indirectly proportional to τ , high diffusion polarization of the electrode roots from increased tortuosity.⁵ One of the challenges when increasing the electrode

thickness is the inhomogeneous distribution of the different components across the layer. A high binder concentration in the region near the separator can increase the overpotential of the electrode while, in the worst case, simultaneously leading to partial or complete delamination of the electrode mass from the current collector. The cross-linking of the polymer binder and the substrate foil is necessary to ensure sufficient adhesion between the coated layer and the current collector, which is proportional to the amount of binder in the vicinity of the substrate. The migration of binder particles, among other factors, is related to insufficient coating and drying parameters and is especially pronounced for high-loading electrodes.^{6,7} The higher number of interconnections between the active material particles by the carbon binder domain can limit ionic diffusion tremendously.⁸

Reducing the electrode tortuosity can help unlock the full potential of high-loading electrodes and diminish the limiting effects of ion transportation in thick coating layers.^{9,10} Changing the structure of the coated material film can be considered a possible solution to shorten the diffusion pathways of the Li-ions across the layer, within the electrolyte. On a macroscopic level, texturing the coated layer e.g. via laser processing can decrease the electrode tortuosity after the standard coating process.^{11,12} Structured electrodes can also be realized during the casting process, through a patterned blade,¹³ or via channel punching of a dry electrode after calendaring.¹⁴ Microscopic structures that enhance the diffusion capabilities can be created through different templating methods such as freeze casting/ice-templating^{15–17} and magnetic templating.¹⁸ All these methods follow the path of improving ion diffusion by increasing the layer porosity while simultaneously decreasing the tortuosity. Unfortunately, this is in most cases contradictory to an increase in volumetric energy density.

Another option to modify the structure of an electrode coating is by using the multi-layer (ML) coating technique.^{19–21} When coating several layers on top of each other, material compositions and characteristic properties such as porosity can be tuned accordingly. Previous studies showed that for thick electrodes, the cycling performance can be notably enhanced by using this novel method.^{22,23} Binder gradients, with higher polymer concentrations close to the current collector, seem advantageous for the electrochemical performance.²³

The impact of coating thickness^{24–27} and porosity^{28,29} on electrode tortuosity has already been explored in prior research. Notably, previous studies predominantly utilized N-methylpyrrolidone (NMP) as a solvent when processing cathode samples.

^xE-mail: lukas.neidhart@ait.ac.at

Investigations involving graphite anodes have also been conducted in combination with multi-layer coatings.³⁰ It is essential to note, however, that the electrodes previously examined featured low loading. Consequently, the advantageous effects of multi-layer coating could not be fully realized.

This work used electrochemical impedance spectroscopy (EIS) to analyze the effect of binder gradients—introduced through ML coating—on the electrode tortuosity. Furthermore, the relationship between electrode thickness and tortuosity is studied on water-based NMC811 samples. Two fitting methods with different complexities were used to determine tortuosity values via EIS measurements and the results were evaluated and compared.

Experimental Methods

Electrode fabrication & characterization.—All cathodes used in this study consist of $\text{LiNi}_{0.8}\text{Mn}_{0.1}\text{Co}_{0.1}\text{O}_2$ (NMC811) (BASF SE; $d_{\text{avg}} = 7.8 \mu\text{m}$) as the active material, carbon black (CB) (C-ENERGY™ SUPER C65, TIMCAL Ltd.; $d_{\text{avg}} = 37 \text{ nm}$), additive graphite (KS6L) (C-ENERGY™ KS6L, TIMCAL Ltd.; $d_{50} = 3.5 \mu\text{m}$) and a two-component binder system consisting of carboxymethyl cellulose (CMC) (WALOCEL™ CRT 2000 PA, DuPont de Nemours Inc.) and poly(methyl)acrylate (PMA) (ENEOS Cathode Binder, ENEOS Materials Belgium BV). Phosphoric acid (Sigma Aldrich) was used for pH stabilization of the slurry. Slurries were mixed with a dissolver blade (DISPERMAT CV3PLUS, VMA GETZMANN GMBH) according to the mixing procedure shown in a previous study.²² A slurry consisting of 92wt% NMC811, 3wt% CB, 2wt% KS6L, 1wt% CMC, and 2wt% PMA was mixed for all samples prepared for thickness measurements as well as for the bottom layer of the multi-layered electrodes. Water was used as a solvent for all slurry formulations. Film thicknesses between $36 \mu\text{m}$ ($\cong 1.54 \text{ mAhcm}^{-2}$) and $170 \mu\text{m}$ ($\cong 8.60 \text{ mAhcm}^{-2}$) were fabricated on a roll-to-roll doctor blade system (SC 30, COATEMA Coating Machinery GmbH) with 3 consecutive drying units. Temperatures were set to 45°C , 55°C , and 50°C with a drying time of 3 min per sector and a coating speed of 0.3 m/min. Cross-sections of the samples with minimum and maximum thickness were taken with an optical microscope (VHX7000, Keyence Corporation) and are shown in Fig. 1. Multi-layer coatings were processed in a consecutive coating step with drying in between the coating of the individual layers. ML samples with reduced binder content were manufactured with 50%, 25%, and 0% of the initial PMA content in the top layer and will be referred to as 50PMA, 25PMA, and 0PMA samples respectively.²³ To investigate the influence of binder concentration in a single-layered electrode, samples with the same overall PMA content as in the ML samples were fabricated. All investigated slurry compositions are listed in Table A-I of the appendix. ML electrodes with 0%, 25%, or 50% of the PMA content compared to the SL electrodes are referred to as 0PMA, 25PMA, and 50PMA, respectively. The suffix “-eq” indicates an SL electrode

with an equal amount of binder as its related ML electrode. Since as-coated electrodes naturally differ in porosity, all samples were calendared to a porosity of 40%, to minimize the influence of this parameter on the tortuosity and guarantee comparability of the samples. SEM images of cross-sections prepared via fast ion beam of the SL and 25PMA samples were analyzed to see the particle distribution in the surface region of the coating. Flow curves were recorded with a rotational rheometer (MCR 302e, Anton Paar) to investigate the shear-dependant behavior of the slurries. Measurements were conducted between a shear rate of 0.01 s^{-1} and 1000 s^{-1} at 25°C .

Blocking electrode experiments.—The tortuosity of the cathodes was determined by using electrochemical impedance spectroscopy on symmetrical coin cells with a Biologic-VSP potentiostat. Electrode discs of $15 \mu\text{m}$ diameter were assembled in 2032 coin cells with a 1.1 mm spring, a $25 \mu\text{m}$ trilayer 2500 Celgard separator, and an appropriate amount of stainless steel spacers depending on the thickness of the electrodes. Differences in coating thickness have a huge impact on the tortuosity calculation. Therefore, the discs assembled for coin cell testing were checked with a spiral micrometer before and after calendaring to guarantee valid tortuosity values. The electrolyte used was 20 mM tetrabutylammonium perchlorate (TBAClO_4) in a 1:1 (w:w) mixture of ethylene carbonate (EC) and dimethyl carbonate (DMC), resulting in an electrical conductivity of 0.71 mS/cm . The frequency range was set between 500 kHz and 100 mHz with an amplitude of 10 mV, to ensure, that no charge transfer occurs during the measurement. The analysis of the performed measurements was done in two ways. On the one hand, with a detailed model fit and on the other hand, with a linear fit of relevant regions.³¹ Landesfeind et al.³¹ showed that a simplified transmission line model (TLM-Q) can be selected as an equivalent circuit for the detailed analysis of symmetric cells in a blocking state, with a non-intercalating electrolyte (Fig. 2).

$$Z(\omega) = \sqrt{\frac{R_{\text{ion}}}{Q(i\omega)^\alpha}} \coth(L\sqrt{R_{\text{ion}}Q(i\omega)^\alpha}) \quad [1]$$

Equation 1 is the corresponding formula for calculating the impedance Z . R_{ion} represents the ionic resistance and Q is the total constant-phase capacitance of the model. α is the constant phase exponent, ω is the angular frequency, and i is the imaginary unit. A fast but decent approximation of the ionic resistance (R_{ion}) can also be determined by analyzing the x -axis offset of the high and low-frequency regions in the Nyquist plot.³² Knowing the area A of the substrate foil, the electric conductivity κ of the electrolyte, the porosity ε of the electrode coating and the thickness d of the coated layer leads to the tortuosity value τ using Eq. 2.

$$\tau = \frac{R_{\text{ion}} A \kappa \varepsilon}{2d} \quad [2]$$

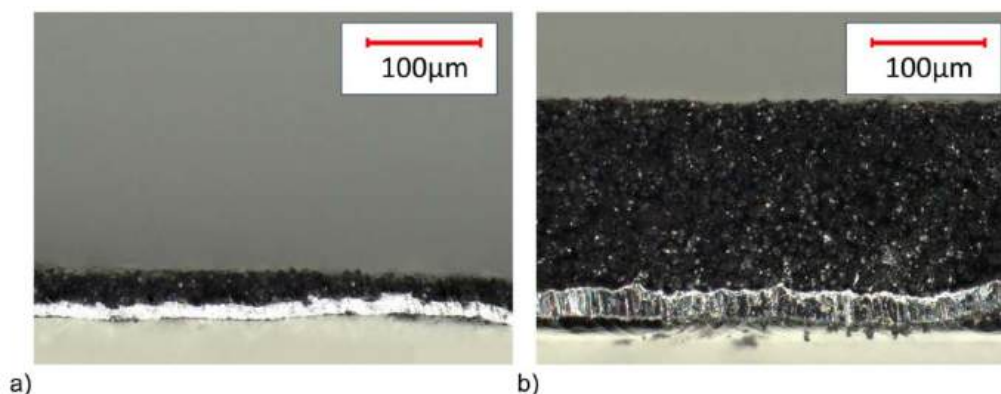


Figure 1. Cross-section images of fabricated cathodes with coating thicknesses of a) $36 \mu\text{m}$ ($\cong 1.54 \text{ mAhcm}^{-2}$) and b) $170 \mu\text{m}$ ($\cong 8.60 \text{ mAhcm}^{-2}$).

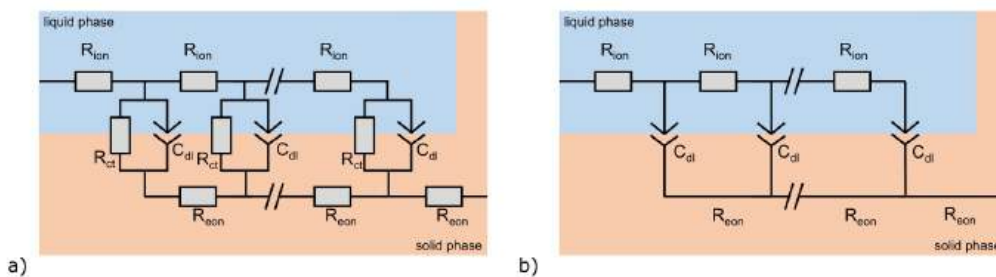


Figure 2. a) Equivalent circuit of transmission line model for faradaic processes, b) simplified transmission line model for blocking conditions in a reflective state.

Results and Discussion

Thickness dependency.—The influence of layer thickness on the ionic resistance and in further consequence on the tortuosity is displayed in Fig. 3 for TLM-Q analyzed samples (yellow) and linear fit (blue). In a certain thickness range, the tortuosity fluctuates around a constant value of about 5. The upper limit of this range is higher for the values determined with the TLM-Q ($154 \mu\text{m}$; $6.44 \text{ mA h cm}^{-2}$) than for the linear fit analysis ($133 \mu\text{m}$; $5.52 \text{ mA h cm}^{-2}$). The tortuosity rises rapidly for thicker samples within our measured thickness range. Standard deviations for thick samples are significantly higher than for thin samples. This behavior is detectable for both fitting methods. Determined tortuosity and R_{ion} values are listed in Table I. The Nyquist plots in Fig. 4 show how with increasing thickness, the low-frequency region gets shifted toward higher impedances and thus higher values of R_{ion} . The two fitting methods used in this study showed a similar trend for both analysis methods and the gathered tortuosity values. The larger deviation for thicker samples might occur due to the larger investigated volume. The investigation of tortuosity dependency on coating thickness shows that a certain threshold thickness exists, above which the overall morphology of the coating is disturbed. In the ideal case of homogeneously distributed material components within the electrode layer, one would expect that the tortuosity does not change with increased thickness. Since it is an intrinsic parameter of a material layer, changes in the composition could be considered a realistic reason for the significantly increasing values above certain thicknesses. Since, the usage of NMP as solvent is still the state of the art for cathode processing, comparison to water-based electrodes can be insightful. Usseglio-Viretta et al.²⁵ investigated the tortuosity of NMP-based NMC532 coatings. They received values approximately half of the ones shown in Table I, for samples below the threshold layer thickness of $150 \mu\text{m}$. This might be due to

structural differences between the PVDF and the CMC/PMA binder system. However, one has to keep in mind that tortuosity is very sensitive to the morphological properties of the coating (e.g. porosity, particle size, and particle shape), thereby compromising error-free comparability.

Multi-layer electrodes.—Tortuosity values of electrodes prepared via the multi-layer coating technique are displayed together with an SL-coated sample for comparison in Fig. 5. The corresponding impedance spectra, including their TLM-Q fit, are shown in Fig. 6. It can be seen that for these samples, the tortuosity values of both analysis methods are comparable and the same positive effect for multi-layer coatings is recognizable. A tortuosity reduction of approximately 65% and 70% for the TLM-Q fit and the linear fit respectively was detected when comparing the SL and ML samples with the same material composition. The ML coating without any changes in binder content is thus comparable with the tortuosity values among the thin coatings in Fig. 3. The electrodes with reduced polymethylacrylate binder content in the top layer show even lower tortuosity values, all determined around 2. 25PMA samples have the overall lowest tortuosity. Binder-reduced samples also show less deviation in their tortuosity compared to SL and ML electrodes. Values for both fitting methods and their standard deviations are listed in Table II.

As already been described,^{7,33,34} the binder migration to the top of the coating is a phenomenon commonly occurring for thick electrodes. The ion-blocking properties of these highly concentrated binder regions can lead to increased tortuosity. The vast improvement in specific discharge capacity for multi-layer coated electrodes also supports this statement. Especially for binder-reduced ML samples, the influence of binder distribution along the cross-section of the layer is confirmed. The reason for the improvements in the

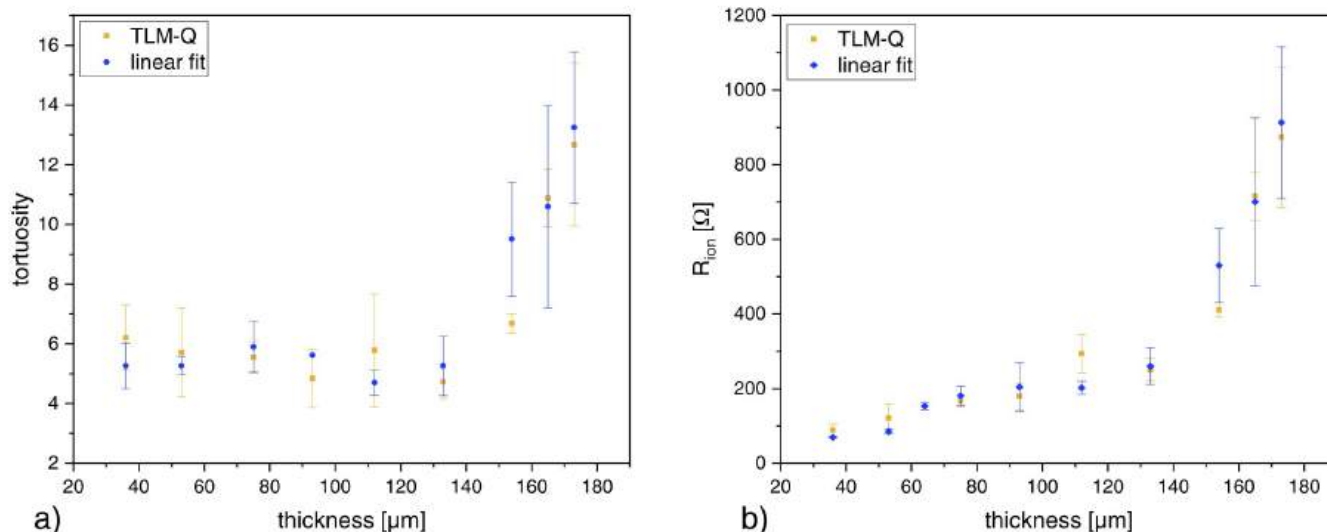
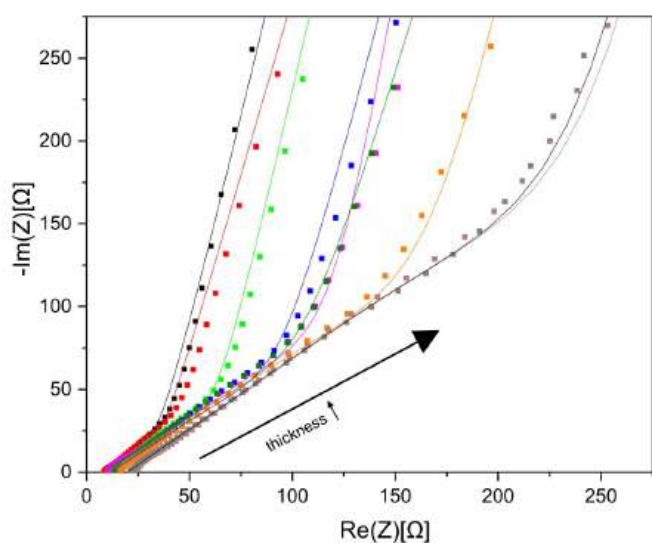
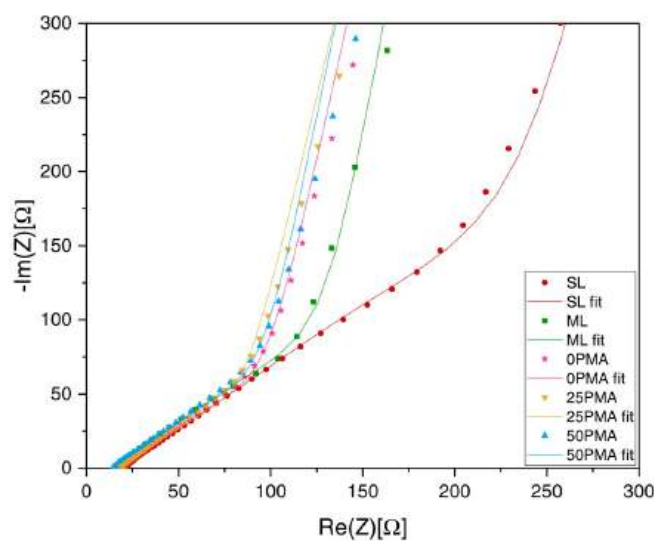
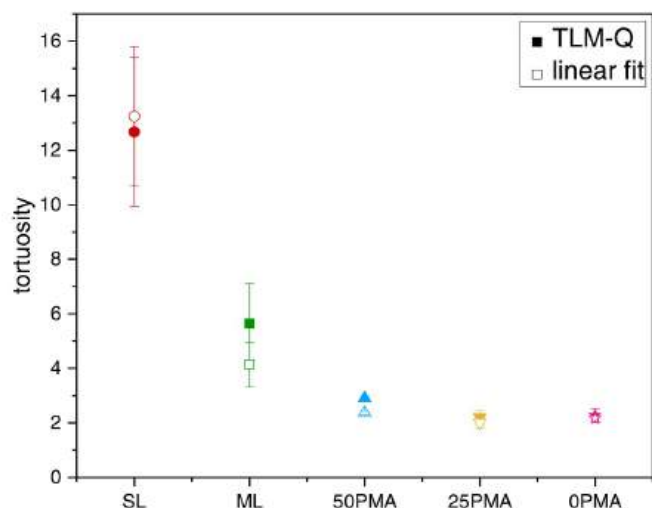


Figure 3. Comparison of both evaluation methods. a) τ against coating thickness and b) the dependency of R_{ion} and the thickness.

Table I. Ionic resistances and resulting tortuosities for different coating thicknesses including standard deviations (SD). All samples are calcendered to a porosity of 40%.

coating thickness (μm)	areal loading (mAhcm^{-2})	TLM-Q				linear fit			
		R_{ion}	$\text{SD}_{R_{\text{ion}}}$	τ	SD_{τ}	R_{ion}	$\text{SD}_{R_{\text{ion}}}$	τ	SD_{τ}
36	1.54	89.04	15.59	6.21	1.09	69.15	0.89	5.26	0.76
53	2.25	120.69	37.07	5.71	1.40	85.10	5.42	5.26	0.31
75	3.21	165.88	18.80	5.55	0.53	152.92	9.53	6.00	0.37
93	3.84	179.16	35.89	4.83	0.97	180.90	25.87	5.90	0.84
112	4.64	293.38	51.12	5.78	1.89	201.84	17.82	4.89	0.41
133	5.52	250.22	30.35	4.72	0.57	259.84	49.24	5.26	1.00
154	6.44	410.09	19.25	6.68	0.31	529.76	99.54	9.51	1.92
165	7.33	715.06	63.83	10.88	0.97	700.70	225.01	10.59	3.40
170	8.60	873.61	187.98	12.67	2.72	913.00	203.05	13.24	2.55

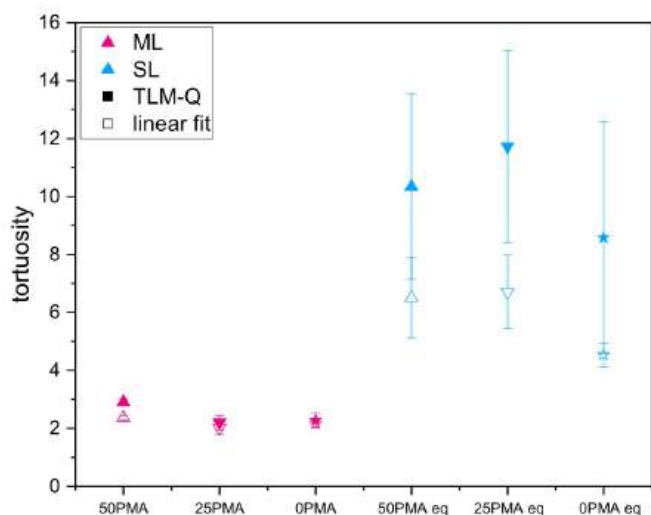
**Figure 4.** Nyquist plots for different thicknesses of water-based NMC811 samples, including their fit.**Figure 6.** Nyquist plots for SL and ML samples, to determine the ionic resistance R_{ion} .**Figure 5.** Tortuosity values for high loading SL and ML samples with varying binder content. Comparison of TLM-Q and linear fit method.

ML binder reduced samples could arise from a) the coating process itself and thus the distribution of binder material, or b) the reduction of the overall binder content in the electrode. Since the bottom layer

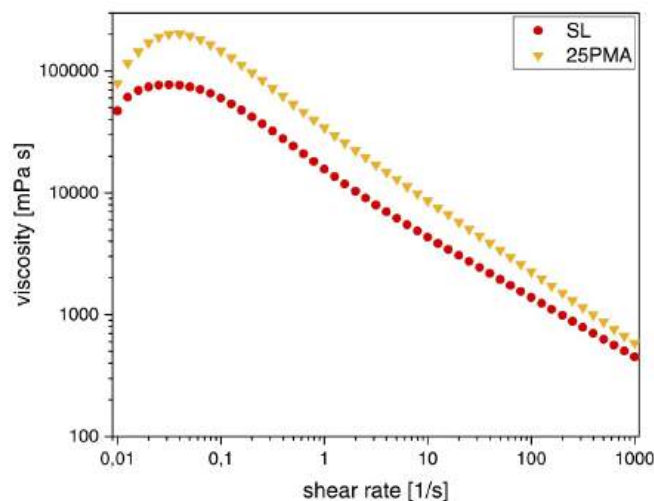
is fully dried before the second coating takes place, binder components in the surface region of the first layer can dissolve into the wet phase of the second coating—due to their solubility in water. This creates an intermixing region connecting both layers. To investigate if the drop in tortuosity arises from the reduction of the binder in the upper layer; single-layer thick electrodes with an equivalent amount of PMA as the reduced binder samples were fabricated. In Fig. 7 and Table III, the results for 50PMA, 25PMA, and OPMA are compared with their associated SL electrode with an equivalent amount of PMA. Compared to the reference SL sample, all SL electrodes with reduced binder show lower tortuosity. For 50PMA-equivalent and 25PMA-equivalent samples, a tortuosity of $\tau = 6.5$ and $\tau = 6.6$ could be determined, respectively. By reducing the amount of PMA even further, τ reaches a value of 4.5—which is still almost double that for ML-coated samples with a similar amount of PMA. Considering these results, these low tortuosity high-loading electrodes benefit from both, the reduction in polymer binder, and the multi-layer coating technique. According to Bernard et al.⁸ the amount of so-called “choke-points” increases proportionally with the binder content of the electrode. Notably, the interaction of the electrolyte and the polymer can result in swelling of the binder particles.³⁵ This effect is enhanced for samples with an increased binder concentration. The accumulation of contact points between the active material particles and their volume expansion can cause an elongation of the liquid phase diffusion pathways and thus increase

Table II. Tortuosity values and their standard deviations (SD) for single-layer and multi-layer samples including samples with reduced binder content, at a porosity of 40%.

	coating thickness (μm)	areal loading (mAhcm^{-2})	TLM-Q		linear fit	
			τ	SD_τ	τ	SD_τ
SL	170	8.60	12.67	2.73	13.243	2.55
ML	173	8.60	5.65	1.46	4.14	0.83
50PMA	176	8.51	2.90	0.11	2.36	0.06
25PMA	178	8.58	2.20	0.26	2.01	0.21
0PMA	178	8.52	2.27	0.24	2.16	0.16

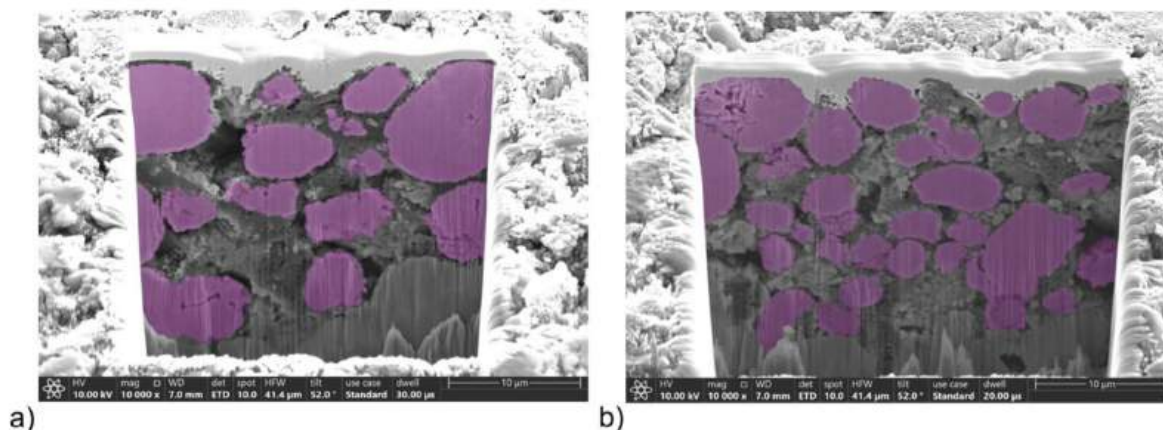
**Figure 7.** Comparison of the tortuosity values of binder reduced ML samples and their corresponding single-layer samples with equivalent amount of binder.

the tortuosity. Additionally, binder-electrolyte interaction also affects the wetting behavior of the coating with electrolyte. Penetration of the electrolyte through the entire depth of the coating gets disturbed with increased layer thickness. Active material closer to the current collector tends to remain inactive in the Li^+ intercalation process, leading to a decrease in capacity. A lower tortuosity can result in a better wetting of the electrode and minimize the non-utilization of NMC particles in the vicinity of the substrate foil. Especially comparison at low current densities, where the difference from the theoretical capacity values should be minimal, can reflect this effect. Figure A-1 shows substantial improvements for all ML samples compared to SL. Accumulation of binder material for SL

**Figure 9.** Flow curves of slurries used for SL and 25PMA electrode fabrication.

samples can be considered an additional explanation for the lower capacity values.

SEM images displayed in Fig. 8 give insights into the particle distribution in the surface region of the coated layer. SL and 25PMA samples are compared to represent the highest and lowest tortuosity values, respectively. Active material particles are colored in purple. Due to a higher binder content, primary particles of the active material in the SL electrode form secondary particles with larger diameters compared to the binder-reduced electrodes. Differences in particle size are also reflected in the rheological data. The flow curves of the SL slurry and the slurry used for the top layer coating of 25PMA (Fig. 9) indicate higher viscosity for the slurry with reduced binder content. Small aggregates have a larger surface area and thus a higher potential to interact with one another. This implies

**Figure 8.** SEM images of the surface region of a) an SL electrode and b) a 25PMA binder reduced multi-layer electrode.

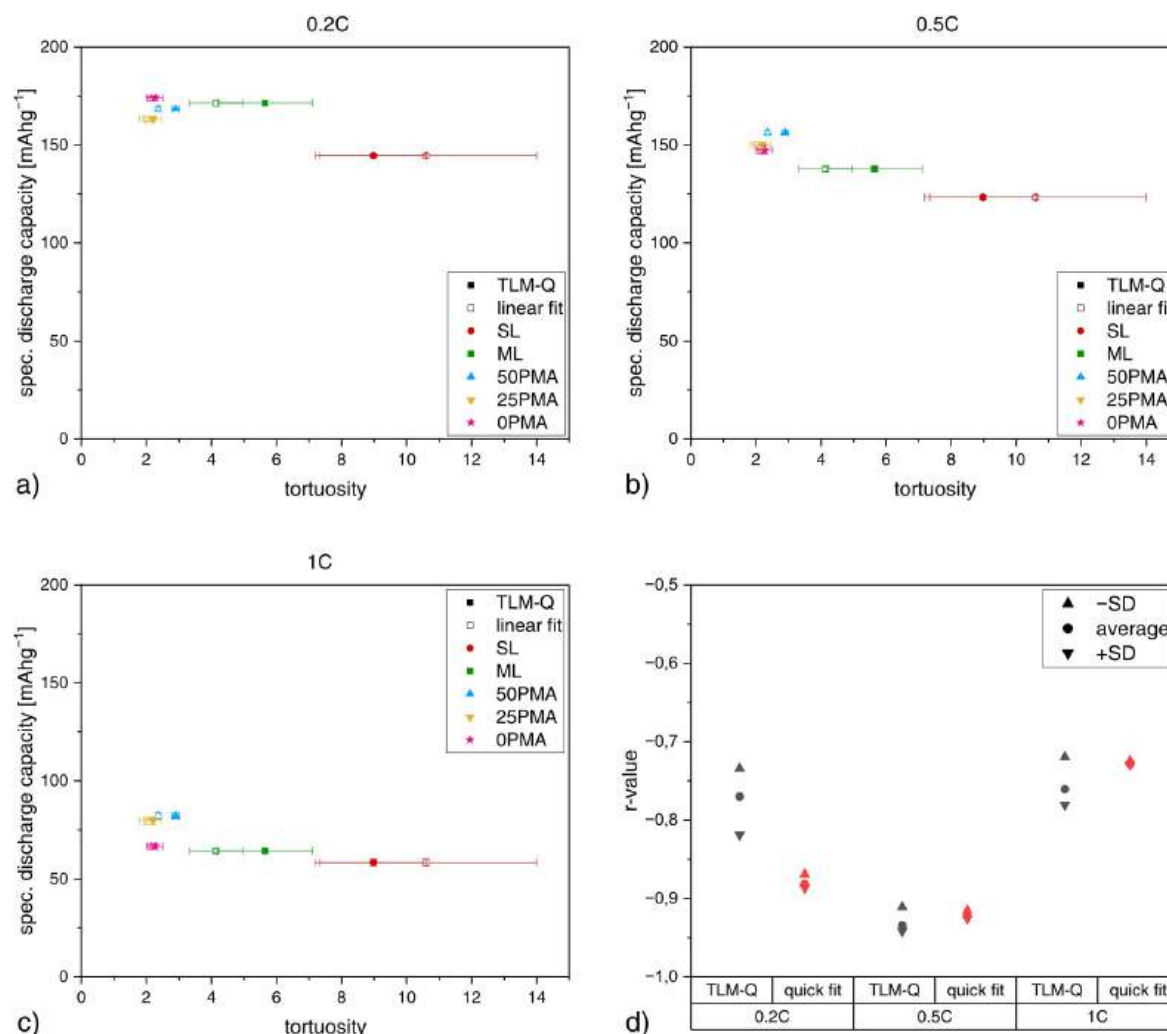


Figure 10. Correlation of tortuosity and specific discharge capacities for high loading ($> 8.5 \text{ mAhcm}^{-2}$) single-layer and multi-layer samples with varying binder concentration in the top-layer at different C-rates, a) 0.2C, b) 0.5C, and c) 1C. d) shows the r-values for different C-rates including their values plus and minus the corresponding standard deviation (SD)

Table III. Tortuosities and their standard deviations (SD) for multi-layer samples with reduced binder content and single-layer samples with equivalent binder content, at a porosity of 40%.

	coating thickness (μm)	areal loading (mAhcm^{-2})	TLM-Q		linear fit	
			τ	SD_τ	τ	SD_τ
50PMA	176	8.51	2.90	0.11	2.36	0.06
25PMA	178	8.58	2.20	0.26	2.01	0.21
0PMA	178	8.52	2.27	0.24	2.16	0.16
50PMA eq	180	8.71	10.34	3.19	6.51	1.39
25PMA eq	178	8.60	11.72	3.30	6.71	1.27
0PMA eq	181	8.68	8.57	4.00	4.53	0.41

smaller active material agglomerates for the sample used in 25PMA electrode preparation.³⁶ Comparing the shape of the curves, one can see that the difference in viscosity is larger for low shear rates and decreases when higher shear forces are applied. For high shear-rates, the agglomerates align and particle-particle interactions become negligible. Both slurries show the expected shear thinning behavior and no significant change in the shape of the curve is noticeable.

A combination of multi-layer coating and binder reduction causes a reduction in tortuosity, however, these results should now be correlated with previously recorded cycling tests, as displayed in Fig. A-1.^{22,23} Fig. 10a-10c displays the specific discharge capacities

of single-layer and multi-layer electrodes (with and without binder reduction) in a full-cell configuration—with a graphitic anode—against their tortuosity values. Three different C-rates were investigated: 0.2C, 0.5C and 1C. A Pearson correlation analysis was performed for tortuosity values determined via TLM-Q and the linear fit method. Since the tortuosity value has a large standard deviation for some samples, the analysis was done for the average value of τ and plus or minus the corresponding standard deviations. The resulting r-values are displayed in Table IV and Fig. 10d. All C-rates show significant correlations between tortuosity and specific discharge capacity. Intuitively one would expect the correlation to be

Table IV. Correlation coefficients of tortuosity and specific discharge capacity values for SL and ML samples with varying binder in top-layer. Average tortuosity values as well as standard deviation values are compared for TLM-Q and linear fit methods and different C-rates.

	r-value	C-rate		
		0.2C	0.5C	1C
TLM-Q	upper	-0.7341	-0.9419	-0.7806
	average	-0.7702	-0.9345	-0.7609
	lower	-0.8189	-0.9109	-0.7196
linear fit	upper	-0.8867	-0.9257	-0.7294
	average	-0.8817	-0.9230	-0.7284
	lower	-0.8691	-0.9154	-0.7248

strongest for the highest current density. However, Li-ion diffusion within the electrolyte is not presumed to be the rate-limiting step here. An imperfect carbon binder domain in the electrode layer without polymethyl acrylate (OPMA) can cause a high charge transfer resistance and thus overcompensate the positive effects of low-tortuous coatings. The difference in deviation of the r -value between the two fit methods results from the larger variation of τ for the linear fit in SL and ML samples.

Conclusion

NMC811 cathode samples were investigated with electrochemical impedance spectroscopy and two different fitting methods. One part of this study was to show how the layer thickness in water-based NMC811 electrodes influences the tortuosity. A threshold thickness of approximately $150\ \mu\text{m}$ was determined, which when exceeded leads to high-tortuous coatings. Tortuosity being an intrinsic parameter of an electrode, should not change when material distribution stays the same. Therefore, we assume that this rapid increase stems from a distortion of the overall morphology of the coating. Moreover, comparison to state-of-the-art PVDF electrodes underlines the demand for finding new ways of further improving aqueous processed cathodes. The multi-layer coating was effectively tested as a strategy to improve the tortuosity of the electrode. This innovative technique on its own enhances the tortuous behavior of the electrode. Further improvements were accomplished by combining a bi-layer coating architecture with a reduction of binder material in the top layer of the electrode. A decrease in tortuosity of $> 80\%$ was achieved for high-loading electrodes when comparing the lowest value ($\tau = 2.2$) of the 25PMA multi-layer sample and the single-layer electrodes ($\tau = 12.67$). A strong correlation was discovered between samples with decreased tortuosity and their specific discharge capacities in a rate capability test. These results show that tortuosity can be considered a performance indicator for high-loading electrodes. To differentiate between the effect of reduced binder and multi-layering, single-layer samples with an equal amount of binder were tested. Binder reduction alone is beneficial for decreased tortuosity, but the combination was the key factor. This could be an indication of possible binder migration since an artificially introduced gradient has positive impacts on the electrode tortuosity. Furthermore, the longevity of the different electrodes in

long-term cycling tests and the resulting consequences on their tortuous behavior will be part of future investigations. Both analysis methods—TLM-Q, and linear fit—show comparable results, throughout all measurements. Considering the simplicity of a linear fit, it is worth mentioning that depending on the purpose of one's investigations it can be useful as a fast way of checking thickness limits for new electrode configurations. However, a more elaborate fitting model such as the TLM-Q fit should be considered when a detailed analysis of electrode characteristics is of interest.

Acknowledgments

This research was funded by the Austrian Federal Ministry for Climate Action, Environment, Energy, Mobility, Innovation and Technology (BMK). SEM sample preparation was carried out using facilities at the University Service Centre for Transmission Electron Microscopy, Vienna University of Technology, Austria.

Appendix

Table A-I. Total amount of active material (AM) and polymethyl acrylate (PMA) used in different electrodes.

	AM(wt%)	PMA(wt%)
SL & ML	92	2.0
50PMA	92.47	1.5
25PMA	92.70	1.25
0PMA	92.94	1.0
50PMA eq	92.47	1.5
25PMA eq	92.70	1.25
0PMA eq	92.94	1.0

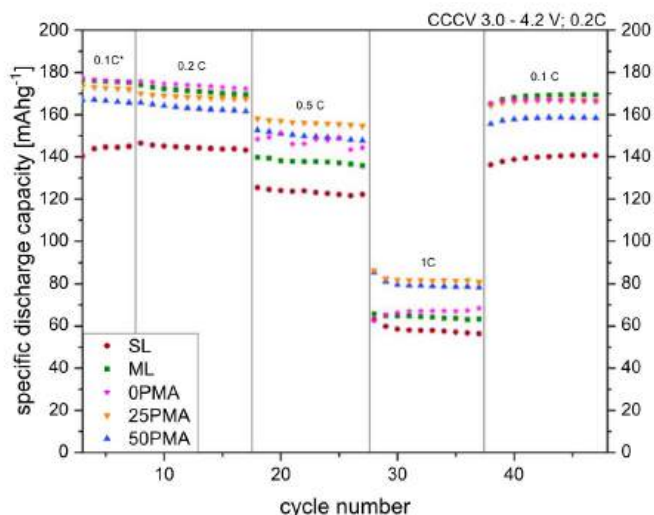


Figure A-1. Comparison of rate-capability test for single-layer and multi-layer samples with varying binder content. (Figure adapted with permission of Neidhart et al.^{22,23})

ORCID

L. Neidhart  <https://orcid.org/0000-0001-8263-6325>
 K. Fröhlich  <https://orcid.org/0000-0001-8978-5550>
 F. Winter  <https://orcid.org/0000-0001-9854-3836>
 M. Jahn  <https://orcid.org/0000-0003-3849-4256>

References

- H. Gao, Q. Wu, Y. Hu, J. P. Zheng, K. Amine, and Z. Chen, *The Journal of Physical Chemistry Letters*, **9**, 5100 (2018).
- C. Heubner, K. Nikolowski, S. Reuber, M. Schneider, M. Wolter, and A. Michaelis, *Batteries & Supercaps*, **4**, 268 (2021).
- N. A. Zacharias, D. R. Nevers, C. Skelton, K. Knackstedt, D. E. Stephenson, and D. R. Wheeler, *J. Electrochem. Soc.*, **160**, A306 (2012).
- D. E. Stephenson, E. M. Hartman, J. N. Harb, and D. R. Wheeler, *J. Electrochem. Soc.*, **154**, A1146 (2007).
- L. Kraft, J. B. Habedank, A. Frank, A. Rheinfeld, and A. Jossen, *J. Electrochem. Soc.*, **167**, 013506 (2020).
- S. Jaiser, M. Müller, M. Baunach, W. Bauer, P. Scharfer, and W. Schabel, *Journal of Power Sources*, **318**, 210 (2016).
- F. Font, B. Protas, G. Richardson, and J. M. Foster, *Journal of Power Sources*, **393**, 177 (2018).
- J. C. Bernard, J. C. Hestenes, K. S. Mayilvahanan, L. E. Marbella, and A. C. West, *J. Electrochem. Soc.*, **170**, 030518 (2023).
- Z. Du, D. L. Wood, C. Daniel, S. Kalnaus, and J. Li, *Journal of Applied Electrochemistry*, **47**, 405 (2017).
- Y. Kuang, C. Chen, D. Kirsch, and L. Hu, *Adv. Energy Mater.*, **9**, 1901457 (2019).
- W. Pfleging, *International Journal of Extreme Manufacturing*, **3**, 012002 (2020).
- L. Schweighofer, B. Eschelmüller, K. Fröhlich, W. Pfleging, and F. Pichler, *Nanomaterials*, **12**, 1574 (2022).
- T. P. Plateau, H. Pham, Y. Zhu, M. Leu, and J. Park, *Adv. Energy Mater.*, **12**, 2201353 (2022).
- H. Wang, J. Li, Z. Miao, K. Huang, Y. Liao, X. Xu, J. Meng, Z. Li, and Y. Huang, *ACS Applied Materials & Interfaces*, **15**, 26227 (2023).
- B. Delattre, R. Amin, J. Sander, J. De Coninck, A. P. Tomsia, and Y. M. Chiang, *J. Electrochem. Soc.*, **165**, A388 (2018).
- C. Huang, M. Dontigny, K. Zaghbi, and P. S. Grant, *Journal of Materials Chemistry A*, **7**, 21421 (2019).
- Z. Nie, R. Parai, C. Cai, C. Michaelis, J. M. LaManna, D. S. Hussey, D. L. Jacobson, D. Ghosh, and G. M. Koenig, *J. Electrochem. Soc.*, **168**, 060550 (2021).
- K. Yang, Y. Jiang, and C. Huang, *International Journal of Electrochemical Science*, **18**, 100348 (2023).
- M. Wood, J. Li, Z. Du, C. Daniel, A. R. Dunlop, B. J. Polzin, A. N. Jansen, G. K. Krundick, and D. L. Wood III, *Journal of Power Sources*, **515**, 230429 (2021).
- S. Kalnaus, K. Livingston, W. B. Hawley, H. Wang, and J. Li, *Journal of Energy Storage*, **44**, 103582 (2021).
- R. Diehm, J. Kumberg, C. Dörner, M. Müller, W. Bauer, P. Scharfer, and W. Schabel, *Energy Technology*, **8**, 1901251 (2020).
- L. Neidhart, K. Fröhlich, N. Eshraghi, D. Cupid, F. Winter, and M. Jahn, *Nanomaterials*, **12**, 317 (2022).
- L. Neidhart, K. Fröhlich, F. Winter, and M. Jahn, *Batteries*, **9**, 171 (2023).
- R. Morasch, J. Keilhofer, H. A. Gasteiger, and B. Suthar, *J. Electrochem. Soc.*, **168**, 080519 (2021).
- F. L. Usseglio-Viretta et al., *J. Electrochem. Soc.*, **165**, A3403 (2018).
- N. Ogihara, Y. Itou, T. Sasaki, and Y. Takeuchi, *The Journal of Physical Chemistry C*, **119**, 4612 (2015).
- N. Ogihara, S. Kawauchi, C. Okuda, Y. Itou, Y. Takeuchi, and Y. Ukyo, *J. Electrochem. Soc.*, **159**, A1034 (2012).
- S. Malifarge, B. Delobel, and C. Delacourt, *J. Electrochem. Soc.*, **164**, E3329 (2017).
- I. V. Thorat, D. E. Stephenson, N. A. Zacharias, K. Zaghbi, J. N. Harb, and D. R. Wheeler, *Journal of Power Sources*, **188**, 592 (2009).
- D. Müller, I. Landa-Medrano, A. Eguia-Barrio, I. Boyano, I. Urdampilleta, I. de Meatza, A. Fill, and P. Birke, *Electrochimica Acta*, **391**, 138966 (2021).
- J. Landesfeind, J. Hattendorff, A. Ehl, W. A. Wall, and H. A. Gasteiger, *J. Electrochem. Soc.*, **163**, A1373 (2016).
- F. Pouraghajan, H. Knight, M. Wray, B. Mazzeo, R. Subbaraman, J. Christensen, and D. Wheeler, *J. Electrochem. Soc.*, **165**, A2644 (2018).
- M. Baunach, S. Jaiser, S. Schmelzle, H. Nirschl, P. Scharfer, and W. Schabel, *Drying Technology*, **34**, 462 (2016).
- B. G. Westphal and A. Kwade, *Journal of Energy Storage*, **18**, 509 (2018).
- J. Qian, C. G. Wiener, Y. Zhu, and B. D. Vogt, *Polymer*, **143**, 237 (2018).
- R. Andersson, G. Hernández, K. Edström, and J. Mindemark, *Energy Technology*, **8**, 2000056 (2020).